DOCTORAATSPROEFSCHRIFT

2007

Faculteit Wetenschappen

Growth and Properties of Nearly Atomically-Flat Single Crystal Diamond Prepared by Plasma-Enhanced Chemical Vapor Deposition and its Surface Interactions

Proefschrift voorgelegd tot het behalen van de graad va Doctor
in Wetenschappen, richting natuurkunde, te verdedigen door

Ganna BOGDAN

Promotor: Prof. Dr. M. Nesládek

Copromotor : Prof. Dr. M. D'Olieslaeger

Instituut voor Materiaalonderzoek

Jury:

Prof. dr. Erna Nauwelaerts, dean Faculty of Sciences, chairman, Belgium

Prof. dr. Milos Nesládek, promoter, UHasselt, IMEC, Belgium

Prof. dr. Marc D’Olieslaeger, co-promoter, UHasselt, IMEC, Belgium

dr. Ken Haenen, UHasselt, Belgium

dr. Oliver Williams, UHasselt, Belgium

Prof. dr. Paul Clauws, UGent, Belgium

Prof. dr. Chris Van Haesendonck, KU-Leuven, Belgium

dr. A. Volodin, KU-Leuven, Belgium

Abstract

This thesis deals with the study of the fundamental growth mechanism of homoepitaxial CVD diamond films using the microwave plasma enhanced chemical vapour deposition (MW PECVD) technique and aiming at depositing high quality intrinsic single crystal diamond, as well as at studying the incorporation of defects. The precise control over the microscopic growth mechanism leads to the minimization of crystallographic imperfections and results in the preparation of diamond crystals with nearly atomically-flat surfaces by mastering the reactions occurring at the growing (100) diamond surface. The spectroscopic study of defects incorporated in the homoepitaxial diamond films, their electrical transport measurements are discussed.

Process parameters domain mapping at high plasma densities and relatively high gas pressures (~180 Torr), using specifically designed plasma configuration including the substrate holder optimization are described. The results obtained suggest that at high CH_4 concentrations and at relatively low growth temperature the diamond (100) growth does not proceed via a generally accepted step flow growth mechanism but leads to an increased probability of a direct carbon radical add-addition to the surface atoms and progresses at many sites leading to nano-sized clusters being formed onto the surface instead of only atomic steps. These nano-sized structures are present onto the surface almost independently of the growth time and are related to the specific growth mode used. The homoepitaxial diamond films grown at these conditions have been investigated in details with high resolution AFM and atomic resolution STM methods. Substrate quality and particularly developed specific surface O_2/H_2 treatments allowing reduction of crystallographic defects incorporated in the films and originating from the substrate are considered to have a major influence on the perfection of the films grown. These findings enable formation of near-atomically smooth thick films.

Bulk defects, impurities and their incorporation to the diamond films have been monitored by defect spectroscopy techniques such as PL, Raman, CL, PC, and EPR. The main defect structures have been traced up in the films grown, related to the impurities such as N, B, Si, H and other elements, which incorporation could be altered by the plasma conditions and gas purity.

Studies of the electrical transport of the (100) homoepitaxial layers have been expanded by the use of TOF technique. The electrical transport properties of freestanding homoepitaxial diamond films have been measured. In non-

optimized samples there is a dispersive transport due to trapping of charge on defects present in the films, as also confirmed by spectroscopic methods. However, the best quality samples grown using high purity gases and optimized growth conditions have shown good electrical properties with high mobilities for electrons and holes.

.

Acknowledgements

I would like to thank Milos for being a fantastic supervisor and ideas with all the practical aspects of the work contained within the thesis and for being so patient with reading drafts of the various chapters. I am indebted to Katrien De Corte, Michel Mermoux, Zdenek Remez, Bradly Cann, Peter Geither for all the help that they have provided to the spectroscopic side of the work, especially with their experts interpretation of the results. I would like to acknowledge Ken Haenen, Johnny Baccus, Olivier Douhèret and the IMO Diamond Group for all their assistance and patience. I would like to thank Alexander Volodin and Cristina Toma from KULeuven for their help with the high resolution AFM and STM measurements and many helpful discussions. And finally to my family, especially my husband and the best friend Andrey Bogdan for the TOF measurements on my samples and all the support.

The Herbalife community and all my close friends have been excellent in helping me with positive thinking and a healthy style of life.

List of publications

As first author

1) G. Bogdan, W.Deferme, K. De Corte, K. Haenen, M. Nesládek, “The growth mechanism of single crystal CVD diamond prepared from CH_4-rich mixtures”, physica status solidi (a) 203 (12), 3063-3069 (2006)

2) G. Bogdan, M. Nesládek, J. D’Haen, K. Haenen, M.D’Olieslaeger, “Freestanding (100) homoepitaxial CVD diamond”, Diamond & Related Materials 15, 508 – 512 (2006)

3) G. Bogdan, M. Nesládek, J. D’Haen, J. Maes, V. V. Moshchalkov, K. Haenen, M. D’Olieslaeger, “Growth and characterization of near-atomically flat, thick homoepitaxial CVD diamond films”, phys. stat. sol. (a) 202, No. 11, 2066-2072 (2005).

As a co-Author

1) W. Deferme, A. Bogdan, G. Bogdan, K. Haenen, W. De Ceuninck and M. Nesládek, “Electrical transport measurements and emission properties of free standing single crystalline CVD diamond samples.”phys. stat. sol. (a) 204 (9): 3017-3022 (2007).

2) A. Volodin, C. Toma, G. Bogdan, W. Deferme, K. Haenen, M. Nesládek, and C.Van Haesendonck, “Electrostatic force microscopy study of electrical conductivity of hydrogen-terminated CVD diamond films”, phys. stat. sol. (a) 204 (9): 2915-2919 (2007).

3) A. Volodin, C. Toma, G. Bogdan, W. Deferme, K. Haenen, M. Nesládek, and C.Van Haesendonck, “Electrostatic force microscopy mapping of electrical conductivity of hydrogen-terminated diamond films”, Appl. Phys. Lett. 91/14 Art. No. 142111 (2007).

4) C. Toma, A Volodin, G. Bogdan, W Deferme, K. Haenen, M. Nesládek, and C.Van Haesendonck, “Voltage dependent modification of hydrogen-terminated

diamond surface using a conductive atomic force microscope tip”, phys. stat. sol. (a) 204 (9): 2920-2924 (2007).

5) Z. Remes, M. Nesládek, N. Tranchant, G. Bogdan, “Optical and electronic properties of freestanding single crystal CVD diamond”, Rome 2007 2nd International Industrial Diamond Conference Proceedings.

6) A. Bogdan, G. Bogdan, W. De Ceuninck, K. Haenen, and M.Nesládek “Electrical Transport and Defect Spectroscopy of Free Standing Single Crystal CVD Diamond Prepared from Methane Rich Mixtures”, MRS Fall Proceedings 2006, Diamond Electronics — Fundamentals to Applications, Volume 956.

7) A. Hikavyy, P. Clauws, W. Deferme, G. Bogdan, K. Haenen, M. Nesládek, “Investigation of hydrogenated CVD diamond films by photo-thermal ionization spectroscopy”, Diamond and Related Materials 15/4-8, 682-686 (2006).

8) A. Hikavyy, P. Clauws, W. Deferme, G. Bogdan, K. Haenen, M. Nesládek, “PTIS investigation of hydrogenated CVD diamond films”, phys. stat. sol. (a) 202, (11), 2171-2176 (2005).

List of symbols and abbreviations

α – growth parameter

AFM – atomic force microscopy

Al - aluminum

AM – amplitude modulation

Ar - argon

ASTeX – Applied Science and Technology (now Seki Technotron Inc.)

B – boron

B – magnetic field

BE – boron bound exciton

BSE – back scattered electrons

C - Capacity

C - Carbon

CH_4 – methane

CL – cathodoluminescence

C_{me} – methane concentration

CNRS – Centre National de la Recherche Scientifique, France

CVD – chemical vapor deposition

CRT – cathode ray tube

DC – direct current

DBP – dual beam photoconductivity

DFT - density functional theory

DICM – differential interference contrast microscopy

DTC – Diamond Trading Company

e – electron charge

E – electrical field

E_a – activation energy (eV)

EBSD – electron backscatter diffraction

ECR – electron cyclotron resonance

EFM – electrostatic force microscopy

EM – electromagnetic

EPR – electron paramagnetic resonance

F – electric field

FCC - face-centered cubic

FE – free exciton

FTIR – Fourier-transform infrared spectroscopy

FTPS – Fourier-transform photocurrent spectroscopy

FWHM – full width at half maximum

H_2 – hydrogen gas

HeCd – helium-cadmium laser

HeNe – helium-neon laser

HF – hot filament

HNO_3 – nitric acid

HPHT – high pressure - high temperature

HRD - Hoge Raad voor Diamant / the Diamond High Council, Antwerp, Belgium

H_2SO_4 – sulphuric acid

IMO – Instituut voor Materiaalonderzoek / Institute for Materials Research, Diepenbeek, Belgium

IMOMEC – Institute for Materials Research in MicroElectronics

IR – infrared

KNO_3 – potassium nitrate

KULeuven - Katholieke Universiteit Leuven, Belgium

LNT – liquid nitrogen temperature (= 77 K)

LT – low temperature

m_0 – free electron mass (kg)

μ – mobility (cm^2/Vs)

Mo - molybdenum

MW - microwave

MW PE – microwave plasma enhanced

N – nitrogen

Nd:YAG - neodymium-doped-aluminum-garnet laser

NIRIM - National Institute for Research in Inorganic Materials, Tsukuba, Japan

Nph – number of photons

N_s – substitutional nitrogen

O_2 – oxygen gas

OES – optical emission spectroscopy

OM – optical microscopy

p – pressure (Torr)

P – power (W)

P - phosphorous

PC – photocurrent method

PDS – photo-thermal deflection spectroscopy

PL – photoluminescence

PLE – photoluminescence excitation

ppb – part per billion

ppm – part per million

Q_{ph} – photo generated charge

RF – radio frequency (Hz)

R_{rms} – root mean square surface roughness

SCCVD – single crystal chemical vapor deposition

SCLC – space charge limited mode

SE – secondary electrons

SEM – scanning electron microscopy

sccm – cubic centimeter per minute at standard temperature and pressure

Si - silicon

STM – scanning tunneling microscopy

TA – transverse acoustic

t_T - transit time

t_E – extraction time

T_e – electron temperature

T_g – neutral gas temperature

TE – transverse electric

TM – transverse magnetic

TO – transverse optical

TOF – time of flight

T_S – substrate temperature

θ_{mis} – misorientation angle

UHV – ultrahigh vacuum

UV – ultraviolet

V_S – saturation velocity

VIS – visible

WTOCD - Wetenschappelijk en Technisch Onderzoeks-Centrum voor Diamant / Scientific and Technical Research Center for Diamond, Lier, Belgium

XRD – X-ray difraction

ZPL – zero-phonon line

Table of contents

Chapter 2 Deposition and characterization Techniques 35

Chapter 3 Optimization of process conditions for thick SCCVD diamond growth 65

Nederlandstalige samenvatting

De exceptionele fysische eigenschappen van diamant maken het een ideale kandidaat voor verschillende technologische toepassingen waar extreme werkingstoestanden voor vereist zijn. Meer specifiek, eigenschappen zoals de transparantie voor zichtbaar licht, het hoge doorslagveld, de hoge stralingshardheid en de chemische inertheid maken het o.a. mogelijk om een "zonneblinde" UV detector of hoogenergetische deeltjesdetector te construeren. Deze kunnen Si-gebaseerde toepassingen in extreme omstandigheden vervangen.

Ondanks de veelbelovende karakteristieken van het materiaal, moet diamant-gebaseerde elektronica opboksen tegen verschillende problemen zoals de kwaliteit van het materiaal, de beschikbaarheid op grote schaal en de kost. Natuurlijk diamant is niet veelbelovend als materiaal voor toepassingen door de afwezigheid van standaardisatie, omdat het duur is en omdat het soms inclusies van defecten of onzuiverheden bevat die de elektronische eigenschappen drastisch beïnvloeden. Een belangrijke inspanning is gewijd aan het ontwikkelen van goed reproduceerbare depositieprocessen die de synthese van diamant kristallen op grote afmetingen toelaten. Kristallen gegroeid met het "High Pressure High Temperature (HPHT)" oftwel Hoge Druk Hoge Temperatuur procédé, hebben gereduceerde afmetingen en bevatten over het algemeen meer onzuiverheden dan natuurlijk diamant, zoals stikstof of overblijfsels van metallische katalysatoren gebruikt tijdens het proces. Daarenboven is het depositietoestel duur. Na de ontwikkeling van zogenaamd "lage druk" diamant met behulp van de chemische damp depositie (CVD) methode door Japanse onderzoekers, kwam er uitzicht op het groeien van diamand tegen een aanvaardbare kost. Hierdoor werden CVD gegroeide diamant lagen intens onderzocht voor elektronische toepassingen, en dit alles op basis van de verwachtte kristalzuiverheid, stabiliteit en reproduceerbaarheid van de CVD groei.

Tijdens de laatste 15 jaar werden doorslaggevende resultaten gepubliceerd door verschillende onderzoeksgroepen in verband met de groei van homoepitaxiaal diamant. Natuurlijk of HPHT monokristallijn diamant, welke stikstof of boor als onzuiverheid bevatten, zijn beschikbaar als diamant substraat. Spiegelglad gepolijst HPHT, type Ib monokristallijn diamant heeft uitstekende structurele eigenschappen en ze zijn commercieel beschikbaar tegen een redelijke prijs en ze worden daarom veel gebruikt voor homoepitaxiale groei. Het gebruik van deze Ib-type samples als substraten voor homoepitaxiale groei in een ultra zuiver gas, laat het toe monokristallijne CVD lagen te groeien met dezelfde hoge structurele kwaliteit maar vrij van de onzuiverheden aanwezig in het substraat. Kristaloriëntaties die vaak worden onderzocht voor homoepitaxiale studies zijn (100), (111), en (110) vlakken. Intense studies hebben aangetoond dat de kristal kwaliteit van de (100) diamantlagen is de beste in vergelijking met de groei van diamantlagen op andere, mogelijke oriëntaties.

De optimalisatie van het depositie proces en het verstaan van het groeimechanisme dat leidt tot zeer hoog kwalitatieve diamant samples is nog niet afgerond. Voor het microgolf plasma gedreven chemische damp depositie (MWPECVD) proces, een van de meest belangrijke zaken is de groeisnelheid van het diamant te verhogen terwijl de hoge kristallijne kwaliteit blijft. Naast onzuiverheden komende van andere elementen, blijven structurele defecten het meest uitdagende probleem in de homoepitaxiale groei. Japanse onderzoekers zijn erin geslaagd atomair vlak homoepitaxiaal diamand te groeien gebruik makend van een zeer lage methaan concentratie (ong. 0.05%) in het depositie gas mengsel.

Omdat de groeisnelheden te laag (< 0.1 μm/h) waren de uiteindelijk bekomen filmdikte typisch een aantal micrometers is. Daarom in de laatste 5 jaar hebben verschillende onderzoeksgroepen studies gelanceerd naar de groei van dikke (meer dan 100 micrometer) homoepitaxiale diamant (100) lagen met hoge groeisnelheden van 1-20 μm/h door het gebruik van hogere microgolf vermogen dichtheden en door het toepassen van speciale groeicondities die heel verschillend zijn van de conventionele. Het vergroten van de kristallen om een monokristallijne wafel te bekomen is een sleutel onderwerp voor commercialisering. Zowel supersnelle homoepitaxiale en heteroepitaxiale groei zijn kandidaten voor dit doel, maar de kennis gewonnen uit een basisstudie van de homoepitaxiale groei is waardevol voor succes in deze pogingen tot kristalvergroting. Daarom worden effecten van elke proces parameter tijdens de groeimode intens bediscussieerd in deze thesis.

Hoewel tot op heden, zover als wij weten, niemand verslagen heeft gepubliceerd op het bereiken van hoog elektronische kwaliteit vrijstaand > 100 micrometer dik monokristallijn diamant wafels buiten de Element Six resultaten, waar TOF metingen hoge mobiliteit waarden zouden geven, zoals is gedemonstreerd in deze thesis dat het bereikt werd.

Hoofdstuk 1 geeft een algemene inleiding. Na een korte beschrijving van wat diamant eigenlijk is, worden de verschillende manieren om het te produceren besproken. Sectie 1.5 en 1.6 omvatten de fundamentele aspecten van de CVD gasfase chemie en het CVD groeimechanisme van homoepitaxiaal diamant. De hoofdroutes van de inclusie van defecten en onzuiverheden in diamant via de gaschemie worden overwogen. Tenslotte wordt een korte samenvatting gegeven van de toepassingen van natuurlijk en synthetisch diamant.

Hoofdstuk 2 handelt over de experimentele methoden die gebruikt warden voor deze thesis. De technieken gebruikt voor de depositie van de diamantlagen, defect spectroscopie en microscopische karakterisering van de afgezette diamant lagen worden in detail besproken.

Het hoofddoel van hoofdstuk 3 is het bestuderen van de groeiparameters om uiteindelijk tot vrijstaande monokristallijne diamantplaatjes te komen. Na vergelijking met de literatuur, werd duidelijk dat het groeimechanisme dat aan de basis ligt van de onderzochte films, niet beschreven staat in de huidige wetenschappelijke literatuur. Dit mechanisme wordt vergeleken met het bekende “step flow” mechanisme. Een belangrijk resultaat is het afzetten van dikke homoepitaxiale diamant films van meerdere honderden micron dik waarbij een quasi atomair vlakke oppervlak behouden blijft. Met andere woorden, het groeimechanisme kan stabiel worden gehouden voor verscheidene uren. Dit groeiproces bevat o.a. het toevoegen van CH_3 radicalen en de stabilisatie van de diamantstructuur. In het bijzonder, bij gebruik van hoge CH_4 concentraties zoals gebruikt in deze thesis, gaat de koolstoftoevoeging niet alleen door op de stapranden maar de stijgende concentratie van CH_3 radicalen leidt tot een hogere kans voor directe toevoeging aan de oppervlakte-atomen. De groei vindt dus plaats op verschillende plaatsen tegelijk waarbij nano-clusters gevormd worden op het oppervlak. Deze groeien verder, raken elkaar, en vormen ten slotte een bijna perfecte structuur. Wanneer de groei onderbroken wordt, kunnen deze structuren zichtbaar gemaakt worden, wat een bevestiging is van dit type van groeimechanisme. Met het gebruik van lage temperatuur raster tunnelmicroscopie kan men zien dat het oppervlak bestaat uit dergelijke nanoclusters. Deze kunnen eventueel geëtst worden om de kristalkwaliteit van het CVD diamantoppervlak met de typische 2x1 reconstructie te onderzoeken.

Omdat de CVD diamant groei een thermodynamisch niet-evenwichtsproces is, waaronder ook de oppervlakte bindingen zoals het atomair waterstof dat sterk vasthangt aan het oppervlak, wordt er geloofd dat zulke uitwisselingen van oppervlakte deeltjes tegen hoge snelheid met hoge concentratie van methyl radicalen significant de oppervlakte morfologie verandert en de formatie van atomair vlakke films bevorderd. Met andere woorden in deze groei mode blijft het volume van de raakvlakken constant en bevochtigen de nanodeeltjes de oppervlakte van de grondlaag (het substraat) en de dunne diamant laag. Omdat de difussie van de oppervlakte gelimiteerd is, bij een substraattemperatuur van 700-

800°C, is de verplaatsing van koolstofatomen minimaal en is het termodynamisch evenwicht niet bereikt. Daarom vindt er op substraatvlak een toevoeging van koolstofradicalen plaats, wat leid tot de ontwikkeling van nanodeeltjes.

Imperfecte nano-clusters interactie, zoals er bijvoorbeeld extra energie nodig is om oppervlakte etsputten te overwinnen, kunnen leiden tot macroscopische in de film. Dit kan verminderd worden door een optimale interactie van het te begroeien oppervlak met het plasma, in termen van optimalisatie van de radicale en atomaire waterstof uitwisseling, oppervlakte energie (gerelateerd aan de potentiële energie in de plasma laag), temperatuur en groeisnelheid. Gebaseerd op deze optimalisatie, bijna atomair vlakke oppervlakken kunnen geprepareerd worden, zelfs voor grote filmdiktes.

Als toevoeging wordt er aangetoond dat de kwaliteit van het oppervlak van het substraat de kwaliteit van de kristal groei drastisch beïnvloed. De oppervlakte defecten zoals dislocaties en de groei sectoren kunnen tijdens de groei in de gegroeide lagen gebrand worden, wat leidt tot kristalgrafische defecten die duidelijk geobserveerd worden door de structurele technieken gebruikt in deze thesis. De Raman spectroscopie afbeelding toonde aan dat de geoptimaliseerde films van uitstekende kwaliteit zijn, met een smalle FWHM Raman lijn, beter dan de IIa natuurlijke kristallen. De beste resultaten hebben getoond dat de FWHM van 1.6 cm^{-1} kan behaald worden. In het geval van niet perfecte substraten stelde de Raman afbeelding ons in staat om defecten, ontwikkeld tijdens de groei van de film, te lokaliseren en de ontwikkeling van defecten in de film te bekijken door de positie, zijn FWHM en de amplitude van de Raman lijn (stress) te bepalen. Deze oppervlakte defecten konden gereduceerd worden door een oppervlakte voorbehandeling welke ook werd ontwikkeld, gebaseerd op het anisotroop etsen in een O_2/H_2 plasma voor de groei, voornamelijk (100) oppervlakken achterlaten, welke samen met een geoptimaliseerde alfa groeiparameter leidde tot bijna atomair vlakke oppervlakken. Het optimaliseren van de alfa groei parameter, waaronder ook het optimaliseren van het CH_4 en T parametrische veld, leidde tot de groei van films in de beste proces condities, waarvan ook de reproduceerbaarheid ook werd bestudeerd.

Tenslotte werd een duidelijk verschil waargenomen tussen de lagen gegroeid met de “oppervlaktecluster” methode en de films gegroei met het stap stroom mechanisme, waar de vorm van het substraat in de diamant films ingebrand werd. Er wordt geloofd dat dit de oorzaak is van de optimalisatie van de groei condities en de “oppervlakte cluster” type groei. De kwaliteit van de lagen gegroeid in termen van kristalgrafische defecten worden bestudeerd in Hoofdstuk 4.

Hoofdstuk 4 is gewijde aan een gedetailleerde karakterisering van bulk defecten in CVD diamant lagen. Een grondige kennis van deze defecten is van het hoogste belang voor alle mogelijke optische en vooral elektronische toepassingen van CVD diamant. De gedetailleerde spectroscopische karakterisering zegt niet enkel iets over de aanwezigheid van defecten, maar bovendien geeft het belangrijke hints over de epitaxiale diamantgroei zelf en het onderliggende mechanisme van de plasma-oppervlak interactie dat leidt tot de integratie van onzuiverheden en defecten. Meer specifiek werd Hoofdstuk 4 in verschillende secties verdeeld: gemmologische karakterisering; optische technieken; magnetische resonantie; elektrische transportmetingen. Een groot deel van dit werk werd uitgevoerd in samenwerking met andere laboratoria met expertise in deze technieken zodat een gedetailleerd beeld kon gevormd worden van de gegroeide CVD lagen.

De gemmologische karakterisering heeft duidelijk aangetoond dat de vrijstaande lagen van hoge gemmologische kwaliteit zijn, overeenkomend met de kwaliteit van IIa natuurlijke diamant. Meer bepaald werd de kleur bepaald met een Gran colorimeter en werden luminescentie-afbeeldingen van de vrijstaande films genomen met behulp van een commercieel apparaat ontwikkeld door E6 en gebruikt door verschillende gemmologische labo’s. De kleur van het beste kristal was D, i.e. vergelijkbaar met de helderste IIa kristallen wanneer deze als juweel geslepen zijn. De luminescentiebeelden van de geoptimaliseerde films vertoonden geen zichtbare (N-V) of (Si-V) luminiscentie. Dit bevestigt dat er weinig integratie is van residuele onzuiverheden. Onder UV-excitatie werd blauwe luminescentie waargenomen, zogenaamde band A, wat gelieerd is aan de aanwezigheid van dislocaties. In afbeeldingen genomen met gekruiste polarisatoren werd een typisch beeld waargenomen van dislocatiepatronen dat verschilt met de bekende “tatami” patronen in natuurlijk IIa diamant. Zoals besproken in Hoodstuk 3, worden de dislocaties in de CVD film dikwijls verzoorzaakt door dislocaties die reeds aanwezig zijn in het substraat. Door een aangepaste plasma oppervlaktebehandeling werd getracht om de concentratie in de diamant film te beperken.

Defectenconcentraties op sub ppm schaal werden bestudeerd met een fotostroom-gebaseerde opstelling, i.e. AMFTPS. Ondanks de genomen voorzorgen, werden zelfs in de beste films residu’s van stikstof in substitutionele toestand waargenomen. De concentratie van deze defecten was in de orde van enkele ppm of lager. De kleine hoeveelheid N komt is afkomstig uit de lucht die onvermijdbaar de reactor binnendringt wegens de niet perfecte aard van het vacuüm. De opgemeten concentratie van substitutioneel stikstof is hoger dan deze bepaald met behulp van EPR, waar substitutioneel stikstof bekend staat als het P1 defect. EPR-metingen geven een concentratie die typisch 1 tot 2 decades lager ligt dan AMFTPS. Waarschijnlijk is dit toe te schrijven aan de specifieke voorwaarde waarbij een defect kan gedetecteerd worden met EPR: enkel defecten met een vrije spin zijn observeerbaar. Wanneer het defect zich dus in een andere ladingstoestand bevindt, kan het mogelijks niet waargenomen worden. De beste commercieel verkrijgbare monsters, tonen ook een vrij hoge N-respons in de AMFTPS-spectra, vergelijkbaar met de films in dit onderzoek. Dit ondersteund de veronderstelling dat de stikstof concentratie in feite hoger is dan wordt opgemeten via EPR. Bovendien werd er in sommige films residueel B gedetecteerd. Er wordt geopperd dat de B-contaminatie zijn oorsprong vindt in de reactor zelf door vertontreininging van de wanden en andere componenten met kleine hoeveelheden B-bevattende verbindingen.

EPR-metingen bevestigden tevens de aanwezigheid van het H1 defect. Er wordt gespeculeerd dat de lage energieband gezien in AMFTPS-spectra en de zogenaamde D_x-defecten, gerelateerd zijn aan dit H1 defect. Meer nog, een kleine (N-V) aanwezigheid werd gezien in de films, maar de exacte concentratie kon niet bepaald worden.

Foto- en kathodeluminescentie studies leverden significante informatie over de specifieke aard van de defecten aanwezig in de film. Van de ongeveer 300 bekende defecten in IIa CVD diamant zijn $(N–V)^0$ en $(N–V)^-$ centra de hoofddefecten die werden geobserveerd. Dit tesamen met een kleine hoeveelheid luminiscentie van het H3 centrum (N-V-N). Ook de blauwe band A luminescentie, de GR1 band gerelateerd aan de vacature (741 nm), en het (Si-V) center (737 nm) afkomstig van Si komend van het microgolf kwarts venster, werden geobserveerd. Ondanks het feit dat de groei gebeurt bij 700 °C, een temperatuur waar vacatures mobiel zijn, werden ze geobserveerd in de CVD films. Bovendien werd soms zwakke emissie bij 596 nm, 683 nm en 600 – 610 nm waargenomen in de vrijstaande stalen. De oorsprong blijft onbekend is. Ook andere complexen zoals 5 RL en 2BD en spoorresten van 3H (503 nm) konden worden gezien.

Het opmeten van CL spectra laat toe om de kwaliteit van CVD films te bestuderen door te kijken naar exciton recombinatie. Meer bepaald konden de pieken bij 235 nm (FE^{TO}), 242 nm (FE^{TO+O}), 233 nm (FE^{TA}) en 238 nm (BE^{TO}) worden gemeten. Aangezien het aan B-gerelateerd gebonden exciton in sommige gevallen kon worden gemeten, kon de B concentratie worden geschat, gebaseerd op de verhouding van BE en FE. Slechts enkele films vertoonden ~ 3 ppb B.

Voor de meeste films was de B-concentratie dus < 0.6 ppb, de detectielimiet van de gebruikte CL opstelling. De CL data bevestigen dus duidelijk de hoge kristallijne kwaliteit van de films in dit onderzoek.

Tenslotte worden in het laatste deel van Hoofdstuk 4 de elektrische transporteigenschappen van CVD diamant films besproken. Voor een groot aantal monsters werd dispersief transport aangetoond, veroorzaakt door vangstcentra, i.e. defecten aanwezig in de CVD diamant films die de geëxciteerde elektrische ladingen vangen. De films van hoogste kwaliteit vertoonde quasi geen vangst van ladingen en dus goede elektrische transporteigenschappen met hoge elektronen– en gatenmobiliteit: 2050 cm^2/Vs voor elektronen en 2250 cm^2/Vs voor gaten, bij kamertemperatuur. Deze waarden komen goed overeen met de data voor IIa diamant.

Hoofdstuk 5 vat de belangrijkste resultaten verkregen in deze thesis samen.

Chapter 1 Diamond

1.1. Introduction to diamond history

The word 'diamond' derives from the Greek *adamao*, meaning 'I tame' or 'I subdue' and related word *adamas*, which means 'hardest steel' or 'hardest substance'. Everyone knows that diamonds are mechanically hard and have an attractive power due to their unique optical properties, but at the same time diamond, as made of carbon, is one of the oldest material one knows. While the rock in which diamonds are found may be 50 to 1600 million years old, the diamonds themselves are approximately 3.3 *billion* years old. This discrepancy is because the volcanic magma that solidifies into the rock where diamonds are found only transported the diamonds from the Earth's mantle to the surface. Diamonds also may be formed under high pressure and temperatures at the site of meteorite impacts. The diamonds formed during an impact may be relatively 'young', but some meteorites contain star dust, debris from the death of a star, which may include diamond crystals. One such meteorite is known to contain tiny diamonds over 5 billion years old. These diamonds are older than our solar system! Virtually all carbon on Earth comes from the stars. Studying the isotopic ratio of the carbon in a diamond makes it possible to trace the history of the carbon. For example, at the earth's surface the ratio of isotopes carbon-12 and carbon-13 is slightly different from that of star dust. Also, certain biological processes actively sort carbon isotopes according to mass, so the isotopic ratio of carbon that has been in living things is different from that of the Earth or the stars. The isotopic ratio of diamond is important physical property which influences many physical properties but also the growth chemistry discussed in this thesis. Although the origin of natural diamond stones is a triggering scientific topic, at least the same excitation brings chemistry of man made diamond – so called synthetic diamond, which can be either prepared by the High Temperature High Pressure synthesis (HPHT) or by the Chemical Vapor Deposition (CVD) route, which detailed investigation is the main topic of this thesis.

Understanding the chemistry of a diamond requires a basic knowledge of the element carbon. A neutral carbon atom has 6 protons and 6 neutrons in its nucleus, balanced by 6 electrons. The electron shell configuration of carbon is $1s^22s^22p^2$. Carbon has a valence of 4, since 4 electrons fill the 2p orbital.

Diamond is then made up of repeating elementary units of carbon atoms joined to four other carbon atoms via the strongest chemical linkage - the covalent bond. Each carbon atom is in a rigid tetrahedral network where it is equidistant from its neighboring carbon atoms. The structural unit of diamond consists of 8 atoms, fundamentally arranged in a cube. This network is very stable and rigid, which is why diamonds are so very hard and have a high melting point.

1.2. Diamond: material structure and properties

Carbon is unique among the elements in its ability to form strong chemical bonds and has a variety of coordination numbers leading to various allotropic forms. Example of carbon bonds are groups of two (e.g. linear chains or carbine phase), three (e.g. graphite) and four (e.g. diamond) atoms.

In graphite, each carbon atom bonds only 3 of its 4 valence electrons with neighboring carbons. The resulting structure of these bonds is a flat sheet of connected carbon atoms (Fig. 1.1 (a)). Though individually strong, these layers are only weakly connected one to another and slip over each other easily, what makes graphite so slippery.

On the other hand diamond is the densest form of carbon, every carbon shares all 4 of its available electrons with adjacent carbon atoms at a distance of 0.154 nm, forming a tetrahedral unit. This strongest known chemical linkage, the covalent bond, is responsible for many of diamond's superlative properties.

Repeating of the structural unit of diamond consisting of 8 atoms which are fundamentally arranged in a cube (Fig. 1.1 (b)) leads to diamond structure. The crystal structure of diamond is equivalent to a face-centered cubic (FCC) lattice, with a basis of two identical carbon atoms: one at (0, 0, 0) and the other at (1/4, 1/4, 1/4), where the coordinates are given as fractions along the cube sides. This is the same as two interpenetrating FCC lattices, offset from each other along a body diagonal by one-quarter of its length.

Graphite is only a few electron volts more stable than diamond, but the activation barrier for conversion of diamond requires almost as much energy as destroying the entire lattice and rebuilding it. Therefore, once diamond is formed, it will not reconvert

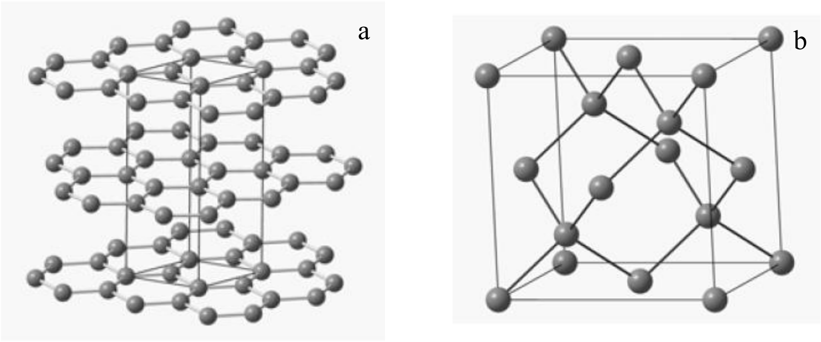

Figure 1.1: *Atomic arrangements of carbon atoms: a) diamond unit cell; b) graphite nano-particle with the unit cell indicated.*

back to graphite because the energetic barrier is too high. Diamonds are therefore said to be metastable, since they are kinetically rather than thermodynamically stable. Under the high pressure and temperature conditions diamond can form naturally being at these conditions more stable than graphite, and so over millions of years carbonaceous deposits may slowly crystallize into diamond. A phase diagram for carbon is shown in Fig. 1.2.

Consequently diamond's particular arrangement of carbon atoms or its crystal structure is the key feature that defines its fundamental properties. Based on the material characteristic, the electronic, structural, or optical properties - associated with diamond are the most extreme ones. Specifically, diamond properties are:

- It is chemicaly inert.
- Mechanical: it is the hardest macroscopic bulk material known to man.
- It has certain high performance electrical properties.
- It has unmatched optical transparency across the widest spectrum.
- It is the most thermally conductive material at room temperature.

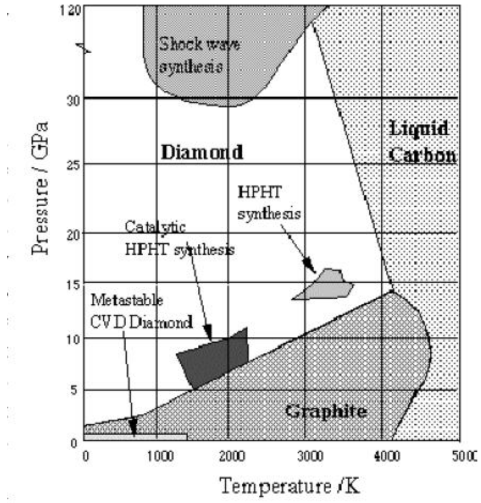

Figure 1.2: *The phase-diagram of carbon from ref [Bun80]*

The following is a table of the properties of diamond that render it so potentially useful across many fields of science.

Property	**Value**	**Units**
Hardness	10 000	kg/mm^2
Strength, tensile	>1.2	GPa
Strength, compressive	>110	GPa
Sound velocity	18 000	m/s
Density	3.52	g/cm^3
Young's modulus	1.22	GPa
Poisson's ratio	0.2	
Thermal expansion coefficient	0.0000011	/K
Thermal conductivity	20.0	W/cm·K
Thermal shock parameter	30 000 000	W/m
Debye temperature	2 200	K
Optical index of refraction (at 591 nm)	2.41	

Optical transmissivity (from nm to far IR)	225	
Loss tangent at 40 Hz	0.0006	
Dielectric constant	5.7	
Dielectric strength	10 000 000	V/cm
Electron mobility	~2 200	$cm^2/V\cdot s$
Hole mobility	~2 000	$cm^2/V\cdot s$
Electron saturated velocity	27 000 000	cm/s
Hole saturated velocity	10 000 000	cm/s
Bandgap	5.45	eV
Resistivity	10^{13} - 10^{16}	Ohm·cm

Table 1.1: *Selected properties of diamond (figures are for single crystal diamond; values measured or calculated at room temperature).*

1.3. Classification of diamond

Because we will often use the nomenclature of a standard diamond marking in this thesis, it is useful to briefly give the basics of the diamond classification:

- Type Ia diamond – colorless, contains nitrogen (up to 3000 ppm) in aggregated, diamagnetic form. About 98% of natural diamonds are of this type. Its prevalence motivated the emergence of different subsystems, of which only one has survived, that divides Ia diamonds to IaA and IaB, containing the A and B nitrogen aggregates.

- Type Ib diamonds, yellow – contain nitrogen (up to 800 ppm) mostly in single substitutional, paramagnetic form. They are very rare (~0.1%) in nature, but most HPHT and some of CVD diamonds can be ranked into this class.

- Type IIa – colorless; diamonds in which impurities can not be detected by conventional IR absorption measurements. In practice it means presence of less than a few ppm of single and aggregated nitrogen and of large variety of other defect centers. In other words, natural IIa diamonds should not be considered as a high-purity material. To the contrary, synthetic IIa diamonds can be of exceptional purity (< 1-10 ppb).

- Type IIb diamond – blue, extremely rare in nature, it is found for example in the Premium mine (South Africa). It contains a significant amount (up to 50 ppm) of boron. Boron forms a singly substitutional acceptor center in diamond making it a p-type semiconductor, with electrical resistivity of 10^1-10^8 Ω·cm. Absorption transitions from the valence band to the boron acceptor level give IIb stones a light blue color. Synthetic IIb stones and CVD films with boron concentration up to 0.1 % can be easily produced.

1.4. Chemical vapor deposition, new method for preparation of diamond

The knowledge that diamond consists solely of carbon [Lav72, Ten97] has led many people to consider making diamond artificially. The carbon phase diagram (Fig. 1.2.) suggests that by heating carbon under pressure diamond can be formed as a thermodynamically stable phase at certain temperature/pressure range. This reasoning forms the basis of the so-called high-pressure high-temperature (HPHT) growth technique [Bun55, Fie79, Nas79, Vri87] which has been used to produce ‘industrial’ diamond for several decades. In this technique, graphite is compressed in a pressure cell to tens of thousands of atmospheres, heated to over 2000 K in the presence of a suitable metal catalyst, and left until diamond crystallizes in the cell.

If diamond would be thermodynamically stable at low pressures, its growth could hypothetically be realized just by adding one by one carbon atom at a time to a primary template and finding a method to stabilize it kinetically, so that a tetrahedrally bonded carbon arrangement (diamond) persists. If this is possible to accomplish for example from a gas phase at lower pressures than it is for the HPHT technique, it could lead to evident benefits in terms of equipment and energy costs. Obviously this is not an easy task because working at low pressures means to move to the region where diamond is not thermodynamically stable over graphite. To prepare diamond in such pressure region was the main challenge taken up in the experiments of Eversole and Angus [Eve58,59, Ang68].In these experiments, thermal decomposition of carbon containing gases, leading to carbon vapor at less than 1 atmosphere pressure was used to deposit diamond on natural diamond crystals heated to ~900°C. The rate of growth in such early chemical vapour deposition (CVD) experiments was very low and graphite was co-deposited with the diamond, making people think that the idea of vapour synthesis of diamond could never become an economically reasonable method compared with the established HPHT process.

However, an advance was made by and Fedoseev, Deryagin *et al.*, who demonstrated that if atomic hydrogen is introduced it could preferentially etch graphite rather than diamond [Der68], leading to the so-called kinetic CVD route. Subsequent Russian work extended the possibilities of vapour phase diamond growth by showing that diamond could be deposited on non-diamond surfaces [Der76, Spi81]. Japanese researchers at the National Institute for Research in Inorganic Materials (NIRIM) in Tsukuba succeeded to put all these findings together in 1981 by building so-called 'hot filament' reactor [Mat82a, Mat82b] in which good quality films of diamond could be grown on non-diamond substrates, at significant rates (~1 $\mu m \cdot h^{-1}$). This system operated using a few percent CH_4 in H_2 at 20 Torr (0.026 atm) pressure using a hot electrically heated W-filament to provide the thermal decomposition of the CH_4 containing gas mixture. The same group reported another method for achieving diamond growth in a so-called 'microwave plasma' reactor [Kam83, Sai86] replacing the hot filament excitation by a plasma generated by absorption of microwave energy in the gas phase. A schematic of the hot filament reactor is shown in Fig. 1.3 as an example of a low pressure CVD technique. The region of typical CVD synthesis is shown on the carbon phase diagram (Fig.1.2). Note that these conditions are positioned well inside the region where graphite is the stable form of carbon. The ability to form diamond under ambient pressure is the essential advantage of CVD methods for low cost growth of diamond, compared with HPHT synthesis.

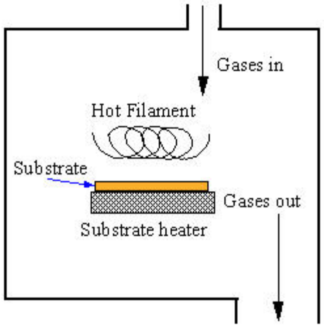

Figure 1.3: *Example of a low pressure CVD technique to deposit diamond. Hot Filament reactor.*

This chain of subsequent discoveries led to world-wide research interest in diamond CVD from the mid 1980's, in both industry and academia, which continues to present day. Numerous methods for diamond film growth have been developed since, such as D.C. plasma [Suz87, Aka88, Cho89, Suz90], radio frequency (RF) plasma [Mat85, Bec94], D.C. plasma jet [Kur88, Lug94, Bou92], microwave plasma jet [Mit89, Smi92], electron cyclotron resonance (ECR) microwave plasma [Kaw87, Suz89, Wei90], and combustion flame synthesis [Han88, Yar89, Tze90]. It is interesting to note that many of these techniques are plasma based.

1.5. Gas-phase chemistry

Diamond CVD growth is most commonly carried out with a reactant gas mixture of approximately 1-10 % methane in hydrogen. Although it is known that diamond growth is relatively unaffected by carbon source gas used, methane is most commonly employed. In order to initiate reactions in the gas-phase it is necessary to activate these gases; this may be carried out by a number of different methods as discussed above and defines the technique used. The activation of the gas mixture, irrespective of the method used, produces atomic hydrogen. Atomic hydrogen is the driving force behind the gas-phase and surface reactions and is clearly one of the most important species present in terms of diamond film growth and quality.

1.5.1. Atomic hydrogen production

The microwave plasma enhanced MW PECVD is a technique based on a direct coupling of MW energy to produce plasma by generating free electrons and ions and energetic radical i.e. the plasma. This reactions lead to H atom production which proceed via several reactions 1.1 shown.

$H_2 + e^- \rightarrow H + H + e^-$ Reaction 1.1

This reaction occurs through successive excitation of H_2 by electron impact in the plasma.

1.5.2. Atomic hydrogen loss mechanisms

The production and loss rates of atomic hydrogen in a reactor are such that a steady state regime exists. The destruction of H atoms, assuming no atomic hydrogen leaves the reaction chamber, occurs mainly via several recombination mechanisms [Has98, Hsu92].

The recombination of atomic hydrogen, under typical conditions prevailing in a CVD reactor, occurs at a slow rate [Lom05]. This allows a supra-equilibrium of atomic hydrogen concentration to exist at low local temperatures, thus supporting a transport of H atoms to the growing surface and stabilizing the deposited diamond kinetically by etching away the graphitic phase. The recombination via the reactor walls occurs via Reaction 1.2 [Has99a, Has99b],

$H + H + M \rightarrow H_2 + M$ Reaction 1.2

where M is a third body, facilitating the removal of excess heat of recombination. This reaction rate is pressure dependant with a characteristic reaction time at a pressure of 20 Torr of the order of several tenths of milliseconds.

The important route for the loss of H atoms is also the heterogeneous recombination due to direct collision with the growing diamond surface. Studies have shown the growing diamond surface is acting as an H atom ‘sink’, the concentration profile at the substrate surface being a function of the substrate temperature [Mit91]. The loss of H atoms to a diamond surface may be expressed in term of the recombination coefficient, which is defined as the atomic hydrogen loss rate at the surface divided by the H atom collision rate with the surface.

At substrate temperatures typically used during diamond CVD (≈ 1000-1300 K), the direct hydrogen recombination coefficient is high, signifying that the surface is acting as a sink for H atoms.

$2H \rightarrow H_2$ Reaction 1.3

This is exothermic (104 $\mathrm{kcal \cdot mol^{-1}}$) and is the major contributor to heating the substrate in many reactor systems.

1.5.3. Hydrocarbon gas-phase chemistry

The presence of a small quantity of hydrocarbon, typically methane, modifies a route of several gas-phase reactions [But93, Goo97], the basic ones, and most important for this thesis deal with the main diamond block - the CH_3 radical:

$H + CH_3 + M \rightarrow CH_4 + M$ Reaction 1.4

$H + CH_4 \rightarrow CH_3 + H_2$ Reaction 1.5

These two reactions compete and hence determine the recombination rate of atomic hydrogen.

As discussed above, the diamond growth under CVD conditions requires that diamond is deposited at a faster rate than graphitic material. Mass spectroscopy studies carried out by Harris *et al.* [Har88] using a quartz sampling tube positioned at the surface of either silicon or platinum substrates, have shown that CH_4 and C_2H_2 are the main species present at a growing surface. The analysis of the gas-phase composition confirms a non-equilibrium nature at the substrate surface. The concentrations of species such as CH_4, C_2H_2, CH_3 and C_2H_4 were measured and found to be sufficient to account for diamond deposition. Larger hydrocarbons (i.e. C_3 and greater) were present in trace quantities only and therefore deemed unimportant for diamond growth. Figure 1.4 summarizes the principal production and loss routes of carbon species in a CVD reactor operating with a CH_4/H_2 gas mixture.

The series of interconnected hydrogen shift reactions (left-hand column of Fig. 1.4) occur rapidly in both the forward and reverse directions due to low activation energies. The rate of reaction between atomic hydrogen and any carbon-containing species is obviously a function of the local gas temperature and the local atomic hydrogen concentration. This relationship defines the production and distribution of C_1 species throughout the reactor [But93].

Due to the complex nature of the reaction scheme and the gas temperature gradients that exist within a CVD reactor the first hydrocarbon concentration measurements of the diamond CVD environment were carried out by Celii *et al.* [Cel88] using an infrared diode laser absorption technique to detect acetylene, methyl radicals and ethylene in a hot filament reactor. This study found that high concentrations of CH_4 and C_2H_2 existed together with low concentrations of CH_3 and C_2H_4 from an input CH_4/H_2 gas mixture. Bearing in mind that the absorption technique used a sampled column of inhomogeneous gas; a rotational temperature of ~600 K was obtained from C_2H_2 detection. On the other hand the gas temperature during MW or DC PECVD can be as high as 3000-5000 K.

The temperature of the gas phase is important as it implies the rates for various plasma-chemical reactions in the gas phase and also it determines the thermal equilibrium hydrocarbon concentrations which are further used in the growth. For example simple gas-phase equilibrium calculations as in [Kee89] for a 1% CH_4/H_2 gas mixture clearly show that the back conversion of dissociated CH_4 to

C_2H_2 occurs at gas temperatures that exist during diamond deposition. One interesting feature resulting from these studies is that the mole fractions of carbon containing species in the activated gas are essentially independent of the input carbon-containing precursor.

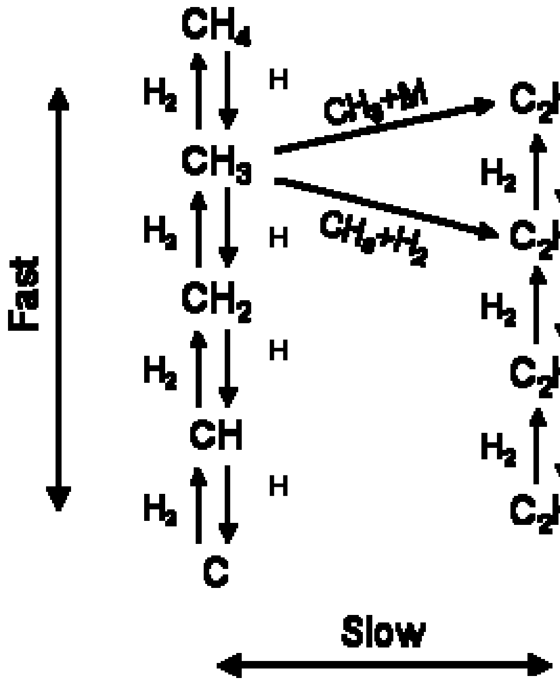

Figure 1.4 *Principal C_1 and C_2 gas-phase reaction scheme illustrating the fast hydrogen shift reactions and the slower bimolecular C_1 to C_2 hydrocarbon forming steps, adapted from ref [But93].*

In the scheme in Fig. 1.4, the conversion of a C_1 species to a C_2 species is carried out via rapid H atom abstraction. If, for example, methane is introduced into a reaction scheme whereby the H/H_2 fraction is below a few percent, methyl radicals (CH_3) may be formed via Reaction 1.6

$H + CH_4 \rightarrow CH_3 + H_2$ Reaction 1.6

Recombination of these methyl radicals will go to form C_2 species via several possible reaction schemes [But93, Har88].

From modeling studies carried out by Dandy and Coltrin [Dan94], it is clear that CH_3, the methyl radical, is the most abundant C_1 radical species present in the gas-phase, under typical low power CVD process conditions. Methyl radicals are formed, via Reaction 1.6. CH_3 radicals are thus the most important species for the diamond growth, discussed further.

1.6. Growth mechanism

1.6.1. CVD diamond nucleation and growth

CVD diamond growth follows a classical crystal growth process of nucleation, addition, propagation, followed by a termination step. Growth of diamond begins when individual carbon atoms nucleated onto the surface in such a way as to initiate the beginnings of a sp^3 tetrahedral lattice. When using a small diamond seed, natural or from HPHT synthesis (by a process called *homoepitaxial* growth), the template for the required tetrahedral structure is already present, and the diamond lattice is just extended atom-by-atom addition as deposition proceeds, which will be discussed further. But for non-diamond substrates (*heteroepitaxial* growth), there is no such template for the C atoms to follow, and those C atoms that deposit in non-diamond forms are immediately etched back into the gas phase by reaction with atomic H. As a result, the initial induction period before which diamond starts to grow can be prohibitively long (hours or even days). Gas-phase nucleation has been suggested as playing almost no role in diamond growth but most studies have been performed in relatively low power and low pressure systems. Any diamond particles formed in the gas-phase have been found to be of such low concentrations that they would have minimal effects on nucleation.

To combat this problem, the substrate surface must undergo a pre-treatment prior to deposition in order to reduce the induction time and to increase the density of nucleation sites. This pre-treatment can involve a number of different processes. The simplest is abrasion of the substrate surface by mechanical polishing or ultrasonic agitation using diamond grit ranging in size from a few nm to 10 μm. It is believed that it aids nucleation by either (a) creating appropriately shaped scratches in the surface, which act as growth templates, or (b) embedding nanometer-sized fragments of diamond into the surface, which then act as seed crystals, or (c) a combination of both. The origins of the nucleation of diamond are important as this can lead to the introduction of many common growth faults [May00]. However as in this thesis we concentrate only on homoepitxail growth the nucleation on foreign substrates is not discussed in further details.

Once individual diamond crystallites have nucleated on the surface, growth proceeds in three dimensions until the crystals coalesce. The resulting film is polycrystalline with many grain boundaries and defects, and exhibits a columnar structure extending upward from the substrate. The surface morphology of the diamond film obtained during CVD depends critically upon the various process conditions, especially the gas mixing ratio, which determines the value for the growth α-parameter which will be discussed in the following section.

1.6.2. Growing surfaces

Atomic hydrogen discussed above, is an essential part of the CVD diamond growth process as it stabilizes the growing diamond surface by maintaining the sp^3 hybridization by saturating the surface radical sites, forming carbon-hydrogen bonds. Hydrogen atoms also preferentially etch sp^2 carbon faster then sp^3 carbon, ensuring that the diamond is the predominant phase of carbon grown [Don97].

The basic more general picture for CVD diamond growth is a site-activation by a surface hydrogen abstraction reaction (1.7), followed by addition of a hydrocarbon radical, (assumed to be CH_3 in this case), (1.8) [But93, Goo98, But01].

$C_dH + H\cdot \rightarrow C_{\cdot d} + H_2$ Reaction 1.7

$C_{\cdot d} + CH\cdot_3 \rightarrow C_d{-}CH_3$ Reaction 1.8

The resulting surface and the surface morphology of a growing diamond surface depend on the different rates at which diamond planes grow.

The growth mechanism [Wil93, Cla92] has been described on the basis of how the relative growth velocities in the <100> and <111> directions determine crystal shapes. For an isolated untwined crystal, the direction of fastest growth is parallel to the largest diameter of the crystallites. This final growth morphology of the crystals is based on so-called α parameter, which defines the morphology of the layer growth on (100) and (111) planes. This growth parameter α is defined as:

$$\alpha = (v_{100} / v_{111})\sqrt{3}$$

where v_{100} and v_{111} are the normal growth velocity of the respective diamond planes [Wil93, Wil94]. For optimisation of the single crystal growth the α parameter is of crucial importance to control the quality of the homoepitaxial layer growth.

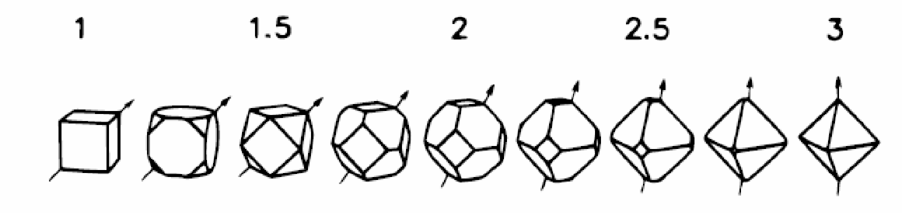

Figure 1.5: *Idiomorphic crystal shapes for different values of the growth parameter α. The arrows indicate the direction of fastest growth (from ref. [Wil93])*

1.6.3. Growth on the (100) surface

Based on the knowledge of the so-called 'alpha-map' [Wil94] which is the dependence of α on experimental conditions such as pressure, methane concentration and temperature an optimal α value can be selected. In general an optimal α value for the growth of (100) oriented films (close to 3) can be reached by using low deposition temperatures and high methane concentrations in the gas phase. Based on this geometrical argument, α parameter has been shown to affect the multitwin formation [Wil94, Yan99]] and ensure preferential (100) growth. Diamond samples which are mainly (100) aligned generally have less defects than the other planes making it the focus of intensive experimental and theoretical studies. An example of such growth carried out in this thesis is demonstrated in Fig. 1.6.

1.6.3.1. The growth mechanism on (100) surfaces

The main mechanism of the (100) plane growth discussed in the literature is the so-called step flow growth, explained schematically in Figure 1.7. In this mode the growth propagates parallel with the surface plane by addition of C atoms via the radical growth mechanism as discussed above.

Detailed investigation on numerous CVD diamond substrates confirmed that this step flow growth is the dominant mechanism as can also be confirmed by a formation of large terraces. The step flow growth mechanism is based upon adsorption of a growth species upon the surface and its subsequent diffusion across the growing surface to step edges and/or other adsorbed atoms.

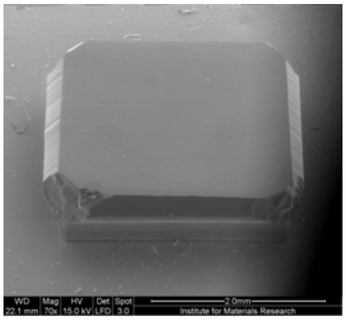

Figure 1.6: *Scanning electron microscopy of a homoepitaxial diamond grown on a (100) diamond plane.*

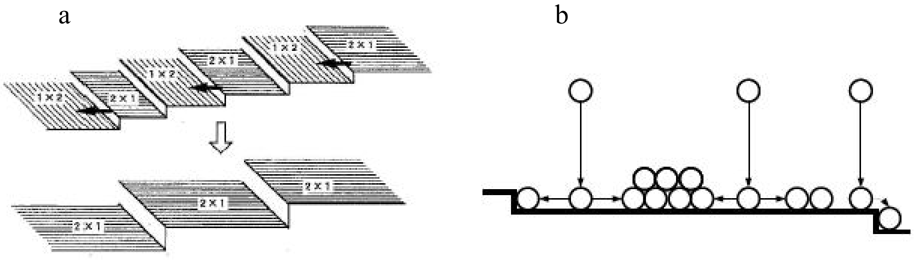

Figure 1.7: *Schematic of epitaxial growth: (a) formation of a single domain surface for a mis-aligned sample from ref. [Tsu94], (b) hillock growth upon a well-aligned sample from ref. [Lee97]*

The ideal step flow growth can be hindered by other processes, which are either secondary nucleation or hillock formation. The level of different terracing depends upon the orientation of the growing diamond surface. Well-oriented substrates show evidence for a hillock growth process, Fig. 1.7(b) [Lee97].

Diamond growth occurring during the CVD process by the continuous adsorption of hydrocarbon precursors and the subsequent abstraction of hydrogen atoms leads to specific surfaces [Gar92, Har93]. On the surface, steps or kinks are energetically the most favorable sites for precursors to join the crystal surface

[Tsu92]. For the misoriented substrate, where plenty of atomic steps are available, it can be considered that the lateral movement of atomic steps through a continuous supply of hydrocarbon precursors into steps makes a major contribution to the growth. In this case, adsorbates landing hinder the further step movement and causing the step bunching or terraces. Another mechanism leading to the disturbance of ideal diamond surface happens when steps are distributed far apart, giving rise to a much larger terrace width than the diffusion length of adsorbates leading to macrosteps. Under given deposition conditions adsorbates can also agglomerate together forming stable clusters and stick to the terrace rather than move to the pre-existing step, this leas to a formation of defects in the step flow hindering the existing steps to move forward. This causes 2D nucleation on the terrace. As the density of steps newly created by the repeated 2D nucleation processes exceeds that of the pre-existing steps, diamond growth begins to be governed by 2D nucleation. The hillock growth through 2D nucleation is schematically illustrated in Fig.1.7 (b). The growth by hillock formation is dominant over the step-flow growth on the well-oriented surface, for example it can be initiated by dislocation or due to the lack of pre-existing surface steps. For the step-flow growth, the steps on atomic scale are already present due to the surface misorientation, whereas for the hillock growth, 2D nucleation on terraces provides steps.

1.6.3.2. The atomic structure of (100) surfaces

Important for the understanding of the step in the (100) surface is the structure of (100) surfaces. The (100) diamond surface upon, hydrogenation is composed of the well-known (2×1) reconstruction where two surface carbon atoms relax from the bulk geometry positions and move together to form a carbon–carbon bond in the plane of the growing surface [Tsu94, Nut96, Bob03]. The diamond surface can be composed of such dimmer rows or multiple dimmers which are neatly arranged into several configurations, an example of it is shown in Fig. 1.8(a) and 1.9(a). This behavior is unlike any other group IV semiconductors, which also undergo (2×1) reconstructions but in case of diamond patterns of alternate dimmers in both directions along the surface can be formed. The high resolution STM figure shows such dimmer arrangement in Fig. 1.9(b).

Density Functional Theory (DFT) calculations explained the experimental evidence that carbon forms a symmetric configuration of dimmer rows. The arrangement of the individual dimmers into rows is due to the strong interaction between the π electrons on the reconstructed carbons due to the localized nature of the carbon's π orbitals [Kru95].

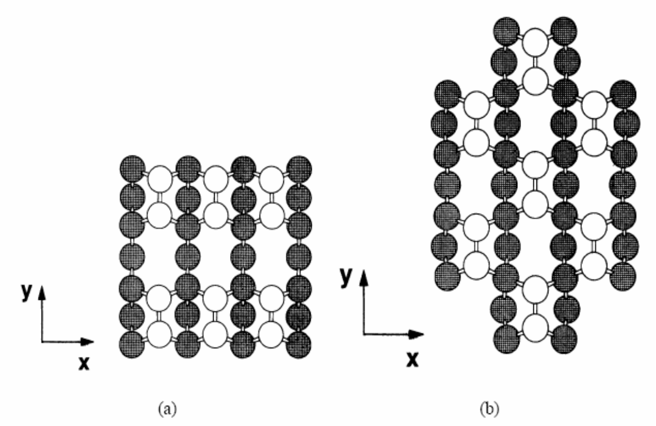

Figure 1.8: *Surface dimer reconstructions arrangement for Group XIV semiconductors showing the (a) row atom arrangement (b) staggered dimer arrangement, adapted from ref. [Sko9].*

From the above discussion it is essential to evaluate what is the implication of the CVD diamond surface reconstruction for the diamond growth. The extent to which growing surfaces are covered with reconstructed dimmers is not clear at present as no in-situ AFM/STM studies with atomic resolution can be easily produced. Numerous scanning tunneling (STM) and atomic force (AFM) microscopy studies showed not only the formation of the (2×1) reconstructions, but also the mirror counterpart as the (1×2) reconstructions and other derivatives like the (3×1) reconstruction, which can incorporate one reconstructed dimmer with an isolated surface dehydrate [Nut96, Bob03, Kru95, Sko93, Tsu91, Yan92, Kua95].

However, there were also suggestions that the surface reconstructions and the formation of the large domains of smooth (100) diamond surfaces is just a post-growth feature either caused by annealing in hydrogen in sample preparation for surface studies [Sta96] or surface etching/annealing that occurs during the shutdown process of a CVD reactor [Sko95a]. The close proximity of the two neighboring hydrogen atoms enables them to associate (at a slight energy cost) and then to dissociate as molecular hydrogen, resulting in formation of a C-C bond in the (100) plane [Hua92]. It is also energetically feasible that the reconstruction process can be initiated by hydrogen abstraction and the resultant lowest energy structure results in the exclusion of atomic hydrogen and the formation of the reconstructed bond. How important these surface reconstructions during the CVD diamond growth are, is a topic studied also partially in this thesis.

Details of the H-terminated surface are shown in Fig 1.9 (b).

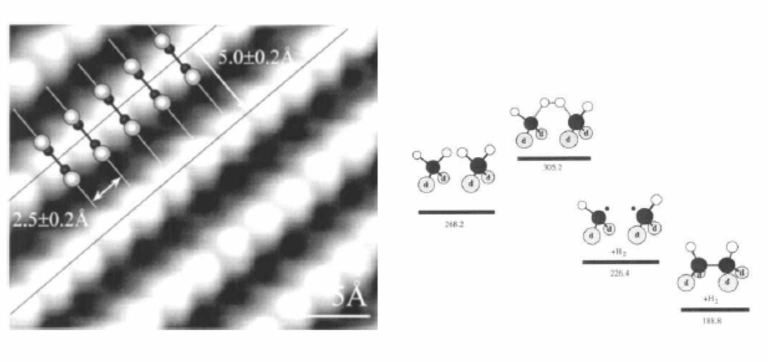

(a) (b)

Figure 1.9: *(a) Scanning Tunneling Microscopy (STM) image of the topography of the hydrogen terminated {100} diamond reconstruction surface from ref. [Bob03]; (b) a proposed mechanism for formation of isolated reconstructed surface dimers for the hydrogen terminated {100} surface from ref. [Hua92] (energy in kcal mol^{-1}), where dark gray circles are diamond, light gray circles are C atoms in chemisorbed hydrocarbons, and white circles are H atoms.*

1.6.3.3. Interactions on the (100) surface during CVD diamond growth

To explain the growth mechanism on (100) surface, studied in this thesis it is important to understand the details of driving forces of C-addition and the surface reconstruction. In Chapters 3 and 4 we will see that not only step flow mechanism can be the dominant mechanism on (100) diamond faces but also a direct addition is important process. Methyl radicals can diffuse from the gas-phase towards the diamond surface and form strong bonds to the surface radical sites. The resulting bound methyl group can be incorporated in two different places:

1) By formation of a carbon–carbon bond at the neighboring end of a reconstructed dimmer bond to which the methyl group is bound;

2) By addition to the neighboring reconstructed carbon dimmer by bridging the trough between the two dimmer rows (Sites A and B respectively in Fig. 1.10).

Both possibilities lead to distinct differences in the diamond growth mechanism studied in the thesis.

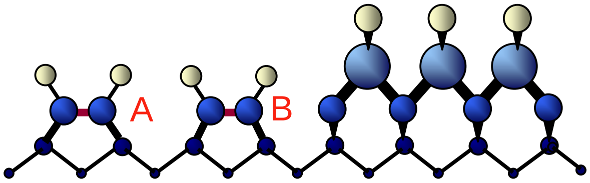

Figure 1.10: *Cross section through the {100} plane showing the dimmer reconstruction (A) and the trough (B) insertion points.*

An alternative growth mechanism is presented in Fig. 1.11, based on carbon insertion into the dimmer bond, (A), initially proposed by Garrison *et al.* from molecular dynamics studies of diamond surfaces [Gar92]. This process is initiated by hydrogen abstraction from a pendant surface bound CH_3 (i.e. C→D in Fig. 1.11). The newly formed CH_2 radical then incorporates into the diamond structure via a ring opening mechanism (D→E→F) rather than by direct insertion of CH_2 into the carbon – carbon bond which has a very large barrier (ca 200 kJ mol^{-1}) [Gar92, Kan00].

A surface bound CH_3 species could be also incorporated across the trough which separates dimmers (site B in Figure 1.10). Incorporation across the dimmer trough was first suggested by Harris *et al.* and was based upon results obtained from studies upon bicyclo-[3, 3, 1] nonane. The process is known as the HH-mechanism.

Neither mechanism adequately describes the effective growth rates and process for a whole new layer of diamond. This has led to suggestions that the overall growth mechanism must involve a combination of several above processes or that one should introduce the possibility of surface migration of reactive species. C_2 has also been investigated for possible incorporation into a non-hydrogenated (2×1) reconstructed (100) surface. This incorporation process is energetically feasible [Ste03] with the stable non-hydrogenated dimmer bond [Tam00], but is unlikely to be a major contributor to the growth process as the lifetime of a surface radical site is not long enough to endure for a second hydrogen abstraction reaction.

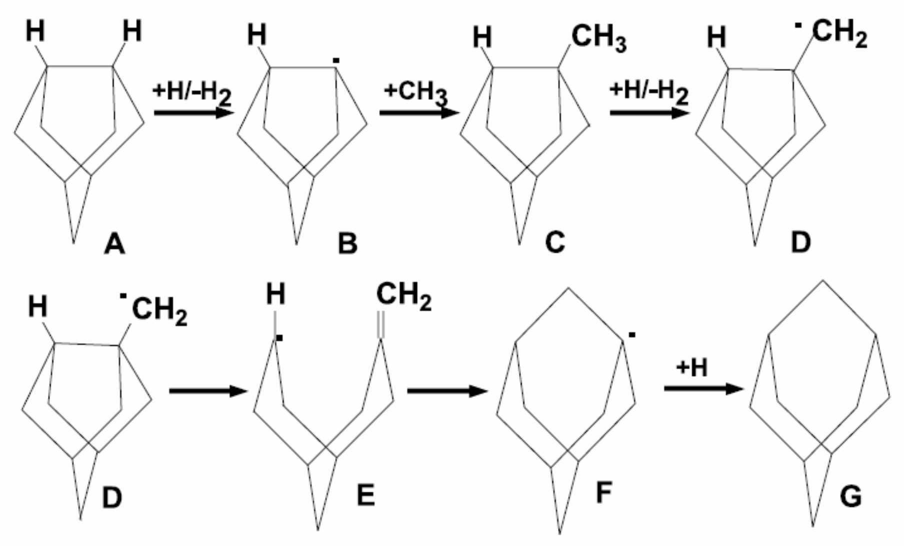

Figure 1.11: *Mechanism for a) hydrogen abstraction and surface activation (A→B); b) carbon incorporation into the diamond (100) surface (C→G).*

1.6.5 Etching

So far, only the mechanisms which focus upon the incorporation of carbon species into the diamond have been discussed. Etching and the removal of non-diamond material is also a critical process going on during the growth. In most gas-surface bond forming steps, like the initial addition of the methyl radical to the active surface site, the possibility of bond fission and disassociation of the reagent back into the gas-phase is unlikely without additional energetic input. This is due to the highly exothermic nature of the addition reaction and these direct desorption processes are highly unlikely unless the resulting carbon–carbon bond is very weak. On the other hand atomic hydrogen in the gas phase will lead to etching processes occurring by the active removal of carbon material by a gas-phase reagent bonding with a pendant surface species and then dissociating it. Most studies have focused on the removal of pendant methyl groups. The simplest way for removal of the surface methyl group is for a direct radical displacement reaction involving atomic hydrogen, resulting in methane dissociating into the gas-phase [Tam05, Sko95b].

In the literature, there has been controversy about the surface morphology after hydrogen plasma etching on (100) diamond. Recently a model has been suggested [Ri06], that the main mechanism of hydrogen plasma etching on (100) diamond is anisotropic etching due to atomic hydrogen [Zhu93, Sta01], and that the step edges are active sites in the etching as well as in the case of step flow growth. Simulated results based on the model explain well the experimental findings. It has been shown that root mean square surface roughness (R_{rms}) of the surface and the etch pits density after hydrogen plasma etching strongly depend on the misorientation angle of diamond substrates. In the report of Ri *et al.*, it was revealed that hydrogen plasma etching has the effect of flattening the surface of diamond substrates with low misorientation angle. The similarity between growth and etching processes revealed in this study, suggested that the effect of hydrogen plasma etching plays an important role in the growth of atomically flat homoepitaxial CVD diamond films.

1.7. Incorporation of defects and impurities in diamond via gas chemistry

In spite of the robust nature of diamond, crystallographic defects faults can be found in crystals due to the growth process. Most of the defects present in the diamond surface are coming from interactions of the growing surface with the gas phase. In some case foreign atoms can be incorporated into the diamond leading to presence of extrinsic impurities in diamond and giving rise to specific defect structures. These defects can appear throughout the crystal, affecting the bulk diamond physical properties and introducing new undesirable features into the diamond electronic structure. The introduction of defects into a diamond causes new characteristics by distorting the crystal and reducing the high level of symmetry of the diamond unit cell.

Diamond, both natural and synthetic, is never completely free of impurities. Defects in diamond can be of two types. Point defects consist of no more than a few atoms or vacancies, so they are in the order of sub nm in size. Extended defects are much larger (at least in one direction) and may be hundreds of nanometers in size, to the point where they are visible optically. Point defects in diamond can be either intrinsic or extrinsic.

Intrinsic self-defects, are misalignments of the diamond structure, creating vacancies or interstitials, and involve no foreign elements or including non-diamond carbon.

A vacancy is a discontinuity in the diamond lattice caused by the complete displacement of a carbon atom from its normal site and the resultant interaction between the former bonding electrons located on neighboring carbon atoms. Absorptions due to singular vacancies have been assigned to neutral [Cla73, Dav74], negatively [Dav77] and positively charged [Mai97] vacancies. There is the possibility of forming multicomponent systems, especially with nitrogen impurities.

Interstitials defects are formed by the displacement of a species from the normal lattices position into a stable but higher energy conformation. An isolated interstitial has not yet been detected in diamond; it migrates, forming different interstitial related centers. The long-standing problems of the self-interstitial and vacancy centers in diamond were recently clarified in careful spectroscopic studies on nearly intrinsic synthetic diamonds [New01, Twi01].

Extrinsic defects are impurity-related, with foreign atoms occupying either substitutional and/or interstitial sites, but many defects are a combination of both intrinsic and extrinsic. The atoms which are known to lie on lattice sites and are most relevant are nitrogen [Smi59], boron [Col70, Iso97b], silicon [Cla95] and hydrogen [Woo83].

Extended defects in crystals can, like point defects, either be intrinsic or extrinsic. Unlike other semiconductors however, diamond generally only exhibits intrinsic defects in the form of dislocations and twins, which are the main reason of birefringence in diamond.

Dislocations are another defect present in CVD and natural diamond. For example in natural diamond they can occur at densities as high as of 10^8–10^9 cm^{-2} [Wil05], but at much lower densities in CVD or HPHT-grown artificial diamond, often only 10^3 - 10^4 cm^{-2}. Their presence can be confirmed by optical or example synchrotron beam imaging, they generally exhibit photoluminescence in the blue or orange regions, which can be used to differentiate between natural and artificial stones [Mar04].

Twinning also is a common stacking fault found in synthetic and natural diamond resulting from a disruption in the growth process. Twinned domains are crystallographically rotated from the parent crystal by a single (or multiple) errors (stacking faults) in the normal a-b-c layer stacking of carbon atom layer along the <111> crystal direction. Twinned growth structures can appear on diamond (100) as well as (111) surfaces. The former are designated as ‘penetration twins’, while the latter are called ‘contact’ twins [Eve94, Wil94]. A consequence of twin formation is the generation of structural and electronic defects [Kas03].

A detailed review on defects in diamond and their electronic models is available in the Literature [Bri93, Cla79a, Cla79b, Dav79, Dav93, Mai94, Mai99, Zai01], therefore this paragraph offers just a short description of the most observed CVD defects and impurities, in particular, of those related to this work.

1.8. Applications of natural and synthetic diamonds

Final remarks of this chapter concern the application area, which is related to the progress in high quality diamond growth. Diamond as a material possesses a remarkable range of physical attributes [Ang92, Yod94] which make it a promising material for a large range of applications [Yod94, Fie92, Yar90]. A selection of these is given in Table 1.2. However, due to the cost and availability of large natural diamonds, most of these applications have not yet been developed to their full potential.

Physical Property	Possible application
Hardest known material: (9×10^9 kg m^{-2}).	Cutting tools.
Highest thermal conductivity at 300 K (2000 Wm^{-1}K^{-1}).	Heat spreaders.
High resistivity (insulator). Breakdown Voltage ~10^7 Vm^{-1}.	Electrical insulation layer for microcircuitry.
Semiconducting when suitably doped.	Electronic devices, sensors.
Negative electron affinity when H-terminated	‘Cold cathode’ electron sources.
IR to UV Transparency	Missile windows. High power laser windows.
Chemical inertness	Electrochemical sensors.

Biological inertness	*In vitro* applications (coatings/sensors)
Radiation hardness	Robust particle detectors.

Table 1.2: *Some of the outstanding properties of synthetic diamond and its possible applications.*

1.8.1. Diamond as a semiconductor material

Diamond's exceptional physical properties make it an ideal candidate for a number of technological applications where extreme operating conditions are required.

In fact, its transparency to visible light, high breakdown field, high radiation hardness and chemical inertness would allow the realization of solar-blind UV detectors [Ben06] or high-energy particle detectors, which might substitute Si-based devices in harsh environments.

However, in spite of the promising characteristics of the material, diamond-based electronics has to face up to some issues regarding mainly the material quality, its large-scale availability and costs. Natural diamond is not promising as an engineering material, because it lacks in standardization, is expensive and sometimes may present the inclusion of defects and impurities that drastically compromise its electronic properties. Therefore, a great effort has been devoted to establish highly reproducible deposition processes allowing the large-scale synthesis of diamond crystals. Specimens grown by High Pressure–High Temperature (HPHT) methods have reduced sizes and generally contain many impurities as nitrogen or metal catalysts. In addition, the deposition equipment is quite expensive.

Subsequently, after development of the low-pressure diamond chemical vapor deposition (CVD) method by Japanese researchers with the promise of realistic industrial growth configurations, CVD diamond films came to be investigated because CVD diamond films offer advantages for electronic applications in crystal purity, stability and reproducibility of its preparation. Depending on the nature of the substrate and details of the process chemistry, polycrystalline or single crystal CVD diamond may be produced.

The polycrystalline CVD samples constitute a serious limitation to its technological exploitation. Semiconducting properties obtained from polycrystalline diamond are not as high as expected from their diamond characteristics because polycrystalline diamond has a much higher defect densities due to the crystal grains and grain boundaries. Therefore, fundamental studies of semiconducting diamond including applicability to electronic devices are needed for making progress on homoepitaxial diamond. Growth mechanisms of diamond crystal under low-pressure conditions have gradually been revealed through many homoepitaxial studies. During the last 15 years, some breakthrough results have been reported from several research groups through advanced studies mainly in Japan, the US, and Europe on homoepitaxial diamond growth. Using optimized HPHT substrates for homoepitaxial growth in an ultra-pure gas phase allows growing single crystal CVD layers with high structural quality but free of the contaminations present in the substrate. High values of the electron and hole mobility measured on homoepitaxial CVD diamond samples (4500 cm^2/Vs for electrons and 3800 cm^2/Vs for holes) of commercial origin with electronic characteristics which are significantly superior to those present in natural high quality diamond, suggested that such material might be successfully used for the realization of diamond-based highly performing electronic devices [Isb02].

However, the optimization of the deposition process and understanding of the growth mechanism leading to very high-quality diamond samples is far not complete yet. For the MW PECVD process, one of the most important issues is to increase the diamond growth rate while maintaining high crystalline quality. Besides contaminations due to foreign elements, structural defects represent the most challenging problem for the homoepitaxial growth. Enlarging crystals to obtain a single-crystalline wafer is a key issue for commercialization. Both super high-rate homoepitaxial growth and heteroepitaxial growth are candidates for this purpose, but the knowledge gained from a basic study of the homoepitaxial growth is valuable for success in these trials of crystal enlarging. Therefore effects of each process parameter on the growth mode will be intensively discussed in the following experimental chapters.

1.9. Aims of this investigation

The study presented herein is ultimately concerned with improving diamond's suitability as a semiconductor material by working on some of the aforementioned problems in the engineering of high quality crystals with suitable electronic properties and low defect density. There are four principal aims of this thesis:

- Investigate the effect of process parameters such as methane concentration, substrate temperature, pressure, power and substrate misorientation angle on the diamond surface with regard to structural properties and the crystal quality and search for the effective process conditions for achieving the development of as perfect as possible diamond crystal.
- Control the atom addition in order to understand the growth mechanism on atomic scale and to control aspects such as the growth rate, crystalline quality, impurity incorporation and defect formation in single crystal diamond films.
- Better understanding of different diamond growth modes to obtain flat epitaxial surfaces and crystals with low defect densities.
- Detail spectroscopic study of defects incorporated in the CVD diamond films and the measurement of their electronic properties such as the charge carrier transport.

1.10. References

[Aka88] F. Akatsuka, Y. Hirose, K. Komaki, Jpn. J. Appl. Phys. **27** (1988), L160.

[Ang68] J. C. Angus, H. A. Will, W. S. Stanko, J. Appl. Phys. **39** (1968), 2915.

[Ang71] J. C. Angus, N. C. Gardner, D. J. Poferl, S. P. Chauhan, T. J. Dyble, P. Sung, Sin Almazy, **3** (1971), 38.

[Ang92] J. C. Angus, Thin Solid Films, **216** (1992), 126.

[Bec94] J. Beckman, R. B. Jackman, J. S. Foord, Diamond Relat. Mater. **3** (1994), 602.

[Ben06] A. BenMoussa, J. F. Hochedez, U. Schuehle, W. Schmutz, K. Haenen, Y. Stockman, A. Soltani, F. Scholze, U. Kroth, V. Mortet, A.Theissen, C. Laubis, M. Richter, S. Koller, J. M. Defise, S.

Koizumi, Diamond Relat. Mater., Sp. Iss. SI, **15** (4-8) (2006), 802-806.

[Bob03] K. Bobrov, A. Mayne, G. Comtet, G. Dujardin, L. Hellner, A. Hoffman, Phys. Rev. **68** (2003), 195416.

[Bou92] A. Boudina, E. Fitzer, G. Wahl, Diam. Relat. Mater. **1** (1992), 380.

[Bri93] P. R. Briddon, R. Jones, Physica B, **185** (1993), 179.

[Bun55] F.P.Bundy, H.T.Hall, H.M.Strong, R.H.Wentorf, Nature, **176** (1955), 51.

[Bun80] F. P. Bundy, J. Geophys. Res. **85** (1980), 6930.

[But93] J.E. Butler, R.L.Woodin, Phil. Trans. R. Soc. Lond. A, **342** (1993), 209.

[But01] J. E.Butler, D. G. Goodwin, Properties Growth and Applications,of Diamond, (ed. M. H. Nazar´e and A. J. Neves), Institution of Electrical Engineers, Michael Faraday House, Six Hills Way, Stevenage, Herts, SG1 2AY UK (2001)

[Cel88] F. G. Celii, P. E. Pehrsson, H. t. Wang, J. E. Butler, Appl. Phys. Letts. **52**, (1988), 2043.

[Cho89] T. Chonan, M. Uenura, S. Futaki, S. Nishi, Jpn. J. Appl. Phys., **28** (1989), L1058.

[Cla73] C. D. Clark , J. Walker, Proc. R. Soc. Lond. A. **234** (1973), 241.

[Cla79a] C. D. Clark, A. T. Collins, G. S. Woods, Properties of diamond, ed. J. E. Field, Academic Press, London (1979).

[Cla79b] C. D. Clark, E. W. J. Mitchel, B. J. Parsons, Properties of diamond, ed. J. E. Field, Academic Press, London (1979), 22.

[Cla92] P. Clausing, W.B. Alexander, P.H. Holloway, L. Heatherly, Surface & Coatings technology, **55** (1-3) (1992), 387-391.

[Cla95] C.D. Clark , Kanda H, Kiflawi I, Sittas G, Phys. Rev. B **51** (1995), 16681-16688.

[Col70] A. T. Collins, W.S. Williams, J. Phys. C: Solid State Phys. **4**, (1970), 1789.

[Col83] A.T. Collins, M.F. Thomaz, M. Jorge, Journal of Phys. C-Solid State Physics, **16** (11) (1983), 2177-2181.

[Dav74] G. Davies , C. M. Penchina, Proc. R. Soc. Lond. A., **59** (1974), 338.

[Dav77] G. Davies, Nature, **269** (1977), 498.

[Dav79] G. Davies, Chem. Phys. Carbon, **13** (1979), 1.

[Dav93] G. Davies, A. T. Collins, Diam. Relat. Mater. **2** (1993), 80.

[Dan94] D.S. Dandy, M.E. Coltrin, J. Appl. Phys. **76** (1994), 3102.

[Der68] B. V. Deryagin, D. V. Fedoseev, V. M. Lukyanovich, B. V. Spitsyn, A. V. Ryanov, A. V. Lavrentyev, J. Cryst. Growth, **2** (1968), 380.

[Der76] B. V. Deryagin, B. V. Spitsyn, L. L. Builov, A. A. Klochov, A. E. Gorodetskii, A. V. Smol'yanimov, Dokl. Akad. Nauk SSSR, **231** (1976), 333.

[Don97] C. M. Donnelly, R. W. McCullough, J. Geddes, Diamond Relat. Mater. **6** (1997), 787.

[Eve58] W. G. Eversole, US Patent Nos. 3030187, 3030188 (1958).

[Eve59] W. G. Eversole, Can. Patent No. 628527 (1959).

[Eve94] M. P Everson, M. A. Tamor, et al. J. of Appl. Physics **75**(1) (1994), 169-172.

[Fie79] J. E. Field, The Properties of Diamonds, Academic, New York, (1979).

[Fie92] J. E. Field, The Properties of Natural and Synthetic Diamond, Academic Press, London, (1992).

[Fre89] M. Frenklach, R. Kematick, D. Huang,W. Howard, K. E.Spear, J. Appl. Phys. **66** (1989), 395.

[Goo97] D. G. Goodwin, J. E. Butler, Handbook of Industrial Diamonds and Diamond Films. G. P. M.A. Prelas, and L.K. Bigelow. NY, NY, Marcel Dekker, (1997), 527-581.

[Goo98] D. G. Goodwin, J. E. Butler, Handbook of Industrial Diamonds and Diamond Films, (ed. M. A. Prelas, G. Popovici, and L. G. Bigelow), Marcel Dekker Inc. (1998).

[Gar92] B.J. Garrison, E.J. Dawnkaski, D. Srivastava, D.W. Brenner, Science, **255** (1992), 835.

[Han88] L. M. Hanssen, W. A. Currington, J. E. Butler, K. A. Snail, Mater. Lett., **7** (1988), 271.

[Har88] S.J. Harris, A.M. Weiner, T.A. Perry, Appl. Phys. Lett., **53** (1988), 1605.

[Har90] S. J. Harris, Appl. Phys. Lett. **56** (1990), 2298.

[Har93] S. J. Harris, D. G. Goodwin, J. Phys. Chem. **97** (1993), 23.

[Has98] K. Hassouni, O. Leroy, S. Farhat, A. Gicquel, Plasma Chem. Plasma P. **18** (1998), 325.

[Has99a] K. Hassouni, A. Gicquel, M. Capitelli, J. Loureiro, Plasma Sources Sci. Technol. **8** (1999), 494.

[Has99b] K. Hassouni, T. A. Grotjohn, A. Gicquel, J. Appl. Phys. **6** (1999), 134.

[Hsu92] W. L. Hsu, J. Appl. Phys. **72** (1992), 3102.

[Hua92] D. Huang, M. Frenklach, J. Phys. Chem. **96** (1992), 1868.

[Isb02] J. Isberg, J. Hammersberg, E. Johansson, T. Wikstrom, D. J. Tw A. J. Whitehead, S. E. Coe, G. A. Scarsbrook, Science **297** (2002) ,1670.

[Iso97b] J .Isoya, H. Kanda, Y. Morita, Phys. Rev. B **56** (1997), 6392.

[Kan00] J. K. Kang, C. B. Musgrave, J. Chem. Phys. **113** (2000), 7582. [Kam83] M. Kamo, U. Sato, S. Matsumoto, N. Setaka, J. Cryst. Growth, **62** (1983), 642.

[Kas03] M. Kasu, T. Makimoto, et al. Applied Physics Letters **83**(17)(2003), 3465-3467.

[Kaw87] H. Kawarada, K. S. Mar, A. Hiraki, Jpn. J. Appl. Phys. **26** (1987), L1032.

[Kee89] R.J. Kee, F.M. Rupley, J.A. Miller, Sandia Nation Laboratories Report SAND89-8009B,(1989).

[Kru95] P. Kruger , J. Pollmann, Phys. Rev. Lett. **74** (1995), 1155.

[Kua95] Y. Kuang, N. Lee, A. Badzian, T. T. Tsong, T. Badzian, C. Chen, Diam. Relat. Mater. **4** (1995), 1371.

[Kur88] K. Kurihara, K. Sasaki, M. Kawarada, N. Koshima, Appl. Phys. Lett., **52** (1988) 437.

[Lav72] A. L. Lavoisier, Memoire Academie des Sciences (1772), 564.

[Lee97] N. Lee , A. Badzian, Diamond. Relat. Mater. **6** (1997), 130.

[Lom05] G. Lombardi, K. Hassouni, G.-D. Stancu, L. Mechold, J. Ropcke, A. Gicquel, J. Appl. Phys. **98** (2005), 053303.

[Lug94] E. Lugscheider, W. Schlump, F. Deuerler, P. Remer, Diamond Relat. Mater., **3** (1994), 325.

[Mai94] A. Mainwood, Phys. Rev. B **49** (1994), 7934.

[Mai97] A. Mainwood, A. M. Stoneham, J. Phys. Condense. Matter. **9** (1997), 2453.

[Mai99] A. Mainwood, Phys. Stat. Sol. (a) **172** (1999).

[Mar04] P. Martineau et al., Gems Gemol. **40** (2004), 2.

[Mat82a] S. Matsumoto, Y. Sato, M. Kamo, N. Setaka, Jpn. J. Appl. Phys. Part 2, **21** (1982), 183.

[Mat82b] S. Matsumoto, Y. Sato, M. Tsutsumi, N. Setaka, J. Mater. Sci., **17** (1982), 3106.

[Mat85] S. Matsumoto, J. Mater. Sci. Lett., **4** (1985), 600.

[May00] P.W. May, Phil. Trans. R. Soc. Lond. A **358** (2000), 473.

[Mit89] Y. Mitsuda, T. Yoshida, K. Akashi, Rev. Sci. Instrum., **60** (1989), 249.

[Mit91] T. Mitomo, T. Ohta, E. Kondoh, K. Ohtsuka, J. Appl. Phys. **70** (1991), 4532.

[Nas79] K. Nassau, J. Nassau, J. Cryst. Growth, **46** (1979) ,157.

[New01] M. Newton, J. Baker, D. Twitchen, Properties Growth and Applications of Diamond (edited by M H Nazar´e and A J Neves), **26** (2001), 204. INSPEC, The Institution of Electrical Engineers, London, United Kingdom.

[Nut96] C. Nutzenadel, O. M. Kuttel, L. Diederich, E. MaillardSchaller, O. Groning, L. Schlapbach, Surf. Sci. **396** (1996), L111.

[Ri06] S.-G. Ri, H. Watanabe, M. Ogura, D. Takeuchi, S. Yamasaki, H.Okushia, J.of Crystal Growth **293** (2006), 311–317.

[Sai86] Y. Saito, S. Matsuda, S. Nogita, J. Mater. Sci. Lett., **5** (1986), 565.

[Sko93] S. Skokov, C. S. Carmer, B. Weiner, and M. Frenklach, Phys.Rev. B **49** (1993), 5662.

[Sko95a] S. Skokov, B. Weiner, M. Frenklach, Th. Frauenheim, M. Sternberg, Phys. Rev. B **52** (1995), 5426.

[Sko95b] S. Skokov, B. Weiner, M. Frenklach, J. Phys. Chem. **99** (1995), 5616.

[Smi59] Smith W V, Sorokin P P, Gelles I L, Lasher G J, Phys.Rev. **115** (1959), 1546.

[Smi92] D. K. Smith, E. Servillano, M. Besen, V. Berkman, L. Bourget, Diam. Relat. Mater. **1** (1992) 814.

[Spi81] B. V. Spitsyn, L. L. Builov, B. V. Deryagin, J. Cryst. Growth, **52** (1981), 219.

[Sta96] R. E. Stallcup II, L. M. Villarreal, S. C. Lim, I. Akwani, A. F. Aviles, J. M. Perez, J. Vac. Sci. Tech. B **14** (1996), 929.

[Sta01] R.E. Stallcup II, J.M. Perez, Phys. Rev. Lett. **86** (2001), 3368.

[Ste90] S. E. Stein, Nature **346** (1990), 517.

[Ste03] M. Sternberg, P. Zapol, L. A. Curtiss, Phys. Rev. B **68** (2003), 205-330.

[Suz87] K. Suzuki, A. Sawabe, H. Yasuda, T. Inuzuka, Appl. Phys. Lett. **50** (1987), 728.

[Suz89] J. Suzuki, H. Kawarada, K. Mar, K. Wei, Y. Yokota, A. Hiraki, Jpn. J. Appl. Phys. **28** (1989), L281.

[Suz90] K. Suzuki, A. Sawabe, H. Yasuda, T. Inuzuka, Jpn. J. Appl. Phys. **29** (1990), 153.

[Tam94] M. A.Tamor, M. P. Everson, Journal of Materials Research **9**(7) (1994), 1839-1848.

[Tam00] H. Tamura, H. Zhou, Y. Hirano, S. Takami, M. Kubo, R. V. Belosludov, A. Miyamoto, A. Imamura, M. N. Gamo, T. Ando, Phys. Rev. B. **62** (2000), 16995.

[Tam05] H. Tamura , M. S. Gordon, Chem. Phys. Lett. **406** (2005), 197.

[Ten97] S. Tennant, Phil. Trans. R. Soc., **87** (1797), 123.

[Tsu91] T. Tsuno, T. Imai, Y. Nishibayashi, K. Hamada1, N. Fujimori, Jpn. J. Appl. Phys. **30** (1991), 1063.

[Tsu92] M. Tsuda, S. Oikawa, S. Furukawa, C. Sckine and M. Hata. J. Electrochem. Soc. **139** (1992), 1482.

[Tsu94] T. Tsuno, T. Tomikawa, S. Shikata, T. lmai, N. Fujimori, Appl. Phys. Lett. **64** (1994), 572.

[Twi01] D. Twitchen, M.Newton, J. Baker, V. Nadolinny, Properties Growth and Applications of Diamond, (edited by M. H. Nazaré A. J. Neves), **26** (2001), 214 (INSPEC, The Institution of Electrical Engineers, London, United Kingdom).

[Tze90] Y. Tzeng, C. Cutshaw, R. Phillips, T. Srivinyunon, A. Ibrahimand, B.H. Loo, Appl. Phys. Lett. **56** (1990), 134.

[Vri87] R. C. De Vries, Ann. Rev. Mater. Sci. **17** (1987),161.

[Wei90] J. Wei, H. Kawarada, J. Suzuki, A. Hiraki, J. Cryst. rowth, **99** (1990), 1201.

[Wil93] C. Wild, P. Koidl, W. Muller-Sebert, H. Walcher, R. Kohl, N. Herres, R. Locher, R. Samlenski, R. Brenn, Diam. Relat. Mater. **3** (1993), 158.

[Wil94] C.Wild, R. Kohl, N. Herres,W.M¨uller-Sebert, P. Koidl, Diamond Relat. Mater. (1994).

[Wil05] B. Willems, L. Nistor, C. Ghica, G. Van Tendeloo, (2005), presented at SBDD-X, LUC Belgium, February 2005.

[Woo83] G.S. Woods, A.T. Collins, Phys. Chem. Solids **44** (1983), 471.

[Yan92] Y. L. Yang, M. P. D'Evelyn, J. Am. Chem. Soc. **114** (1992), 2796.

[Yan99] C. S. Yan, Y. K. Vohra, Diam Relat. Mater. **8**(11) (1999), 2022- 2031.

[Yar89] W. A. Yarborough, M. A. Stewart, J. A. Cooper, Surf. Coat. Technol, **39** (1989), 241.

[Yar90] W. A. Yarbrough, R. Messier, Science, **247** (1990),688.

[Yod94] M. N. Yoder, Synthetic Diamond: Emerging CVD Science and Technology, First ed. K. E. Spear and J. P. Dismukes eds., John Wiley & Sons, (1994).

[Zhu93] M. Zhu, R.H. Hauge, J.L. Margrave, M.P. D'Evelyn, in: J.P. Diamukes, K.V. Ravi (Eds.), Diamond Materials, The Electrochemical Society, Pennington, NJ, (1993), 138

Chapter 2 Deposition and characterization techniques

2.1. Microwave plasma enhanced CVD

Microwave plasma enhanced chemical vapor deposition MW PECVD was initially used for diamond synthesis in 1982 at NIRIM by Kamo *et al.* [Kam83]. This type of reactor therefore called a NIRIM-type microwave plasma reactor is shown schematically in Fig. 2.1. In order to explain the operation of MW PECVD reactors a brief explanation of microwave propagation in waveguides is given.

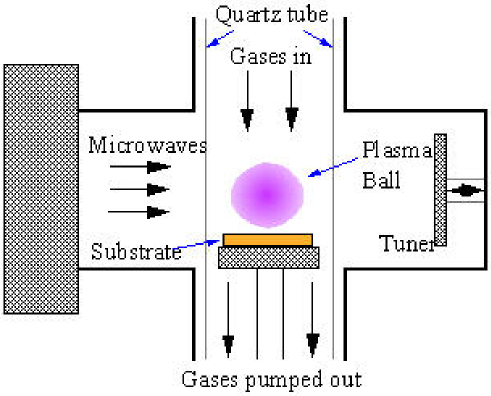

Figure 2.1: *NIRIM-type Microwave Plasma Enchanced CVD reactor.*

2.1.1. Waveguide transmission of microwaves

As microwaves is electromagnetic radiation, described by Maxwellian wave equations. At certain conditions it can propagate in the close fixed space, known as waveguide, using principles of reflective boundaries and it can be confined within a close space. The electric field strength **E**, and the magnetic field strength **B**, fluctuate periodically through the waveguide [Bad90]. Example of MW confined in spaced is a standing wave, formed by fitting an integer number of half wavelengths in the length of a box. The modes are denoted as transverse electric (TE) or transverse magnetic (TM), depending on whether **E**, or **B** respectively is perpendicular to the propagation direction in the waveguide. In a simple annotation a double subscript, for example TE_{mn} for a transverse electric mode, is generally used to denote the mode type, for detail see [Bad90]). In general, a microwave frequency of 2.45 GHz (used by commercial microwave ovens) is usually used in CVD reactors. Nevertheless 915 MHz reactors are now becoming more attractive, as the lower frequency allows the reactor size to be increased proportionally to the wavelength of MW used.

2.1.2.Plasma generation process

In the NIRIM-type reactor, a quartz tube passes through an opening in the waveguide in a region where the standing wave electric field is strongest. The tuner can be used to adjust the waveguide length to allow the highest electric field and the best 'matching' conditions. Injecting gas into the quartz tube allows generation of a plasma by absorption of MW energy in the gas by the mechanism of impact ionization, induced by the local electric field. The mechanism of plasma generation is however very similar in most of types of MW plasma reactors used for diamond growth.

To form plasma, a favorable ionization event, triggered thermally or intentionally (spark), can supply free electrons to the gas. The free electrons generated are accelerated by the strong local standing wave electric field in the waveguide. These electrons lose energy by collisions with gas molecules in the reactor, exciting the reactant molecules. Successive vibrational excitation or collision with a sufficiently energetic electron will result in dissociation of reactant gas molecules producing radical or ionic species. A cascade of ionization is set up and a steady state concentration of free electrons is reached when the rate of electron production is counterbalanced by the rate of electron loss. Electronic transitions in excited state molecules produce radiation which causes the plasma region to glow. The plasma generated during diamond deposition conditions typically takes the form of a ball glowing from purple-blue to greenish depending on the gas composition used. The plasma bal is typically ~1-6 cm in diameter, depending on the MW power and pressure and holder configuration. Microwaves do not heat only the gas but also the substrate holder, depending on the MW frequency used.

At specific conditions the reactive gas species (electrons, ions, and radicals) are not only produced by impact ionization but also by thermal dissociation of the gas. Such conditions are for example relatively high gas pressures above 10 mbar, when the high collision frequency leads to gas heating. Such gas mixture contains the reactants and substrate under favorable conditions for diamond growth. Electrons have higher energies, and accordingly higher velocities, than neutral and ionic species. For this reason electrons quickly diffuse from the plasma region, and are lost at the reactor walls, before they can thermalise. Two or more temperature fields are therefore needed to describe the temperature of the microwave plasma. These are usually the electron temperature T_e, and the neutral gas temperature T_g. Hence $T_e > T_g$ usually in a cold plasma, demonstrating that the system is not in thermal equilibrium. Electron temperatures can be measured using probe techniques while optical emission spectroscopy techniques (OES) can be used to measure vibrational or gas temperatures. Calculated, using computer models, the temperatures are found to be in the region of 1-5 eV (10^4 to 10^5 K) for typical diamond depositing plasmas [Gic94, Ree95]. The neutral gas temperature is believed to be in the range 800-5000 K (0.07-0.4 eV), depending on the experimental conditions [Gic94], demonstrating the thermal non-equilibrium of the electrons and neutrals. Ions cannot respond to the rapidly oscillating microwave field as quickly as electrons due to their greater mass. Ions thus have similar energies to neutral species, as they collide with the neutrals and thermalise.

2.1.3. ASTeX-type microwave plasma CVD reactor

A drawback of the NIRIM-type reactor is that the substrate temperature cannot be easily controlled from the plasma parameters since the substrate is immersed in the plasma. Another problem is the small diameter of the quartz tube used leads to an intense exchange of the plasma and the gas molecules with the quartz tube walls leading to heating of the tube with drawbacks of incorporation of Si and O atoms in the growing film. One of the possible solutions to this problem is using an ‘ASTeX’-type reactor design (ASTeX is a commercial manufacturer of plasma systems based in the US). In an ASTeX-type reactor, the plasma can be generated above a substrate, remote from reactor stainless steel wall surfaces. By application of additional heating or cooling on the substrate stage one minimizes partially the effect of plasma heating allowing almost independent control of plasma and substrate parameters.

This design used in this thesis is using a microwave generator and rectangular waveguide, with a mode converter to convert the TE_{10} mode in the rectangular waveguide to a TM_{01} mode in a cylindrical waveguide launched into the reactor vessel. The length of this cylindrical waveguide is tuned to the standing wave resonance, allowing a maximum amount of energy to be coupled into the plasma. This is achieved by a moveable antenna maximizing the energy coupling between the two waveguide sections and by terminating the cylindrical waveguide with a metallic substrate holder. With the waveguide, standing TM_{01}

electromagnetic field modes are supported in the cavity. Further tuning of the microwave circuit is possible by using the moveable substrate stage to adjust the cavity geometry.

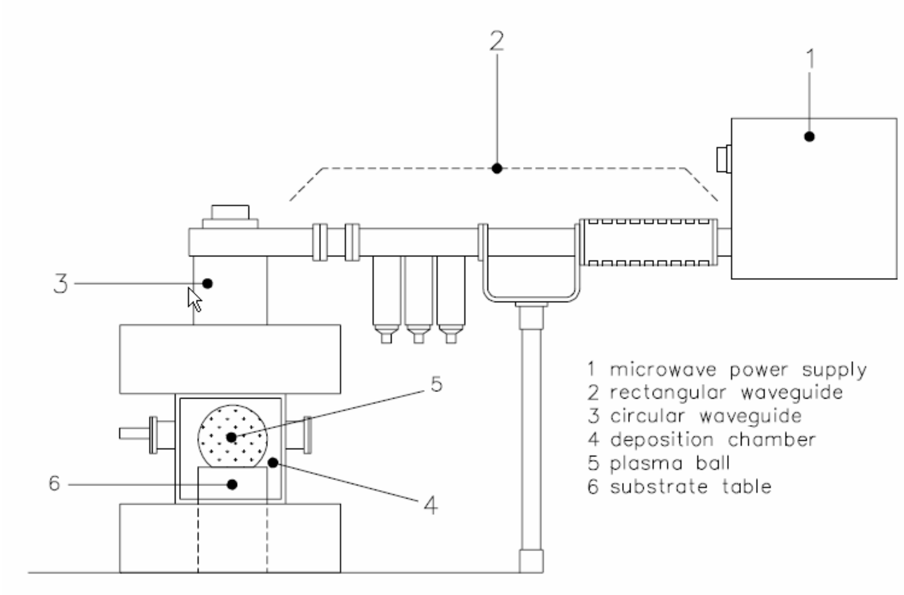

Generation of the plasma occurs by the same mechanisms as discussed above for the NIRIM-type reactor, in the regions where the local electric field strength is highest. But the ASTeX-type reactor is a slight variation of the most common microwave plasma CVD reactor types specifically designed for the operation at rather high gas pressures. The reactor used in this thesis is a variant of the ASTeX design and in the reality, this reactor is far more complex than a simple cylinder due to the presence of service ports, welds, diagnostic probes, etc., which in theory can slightly modify the electromagnetic field profile. In general it is only possible to predict the electromagnetic field structure, and hence plasma location, by numerical solving of Maxwell's equations within the entire reactor volume, as in the modeling work of Wild *et al* [Wil95].

Fig. 2.2 and 2.3 show a scheme and a photo of the apparatus used in this thesis for producing homoepitaxial diamond thin film. The illustrated-apparatus is an end-launch-type microwave plasma assisted CVD diamond synthesizer that projects microwaves normally to the surface of a substrate.

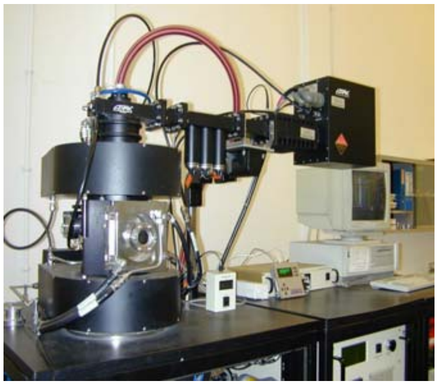

Figure 2.3: *5 kW Plasma deposition system from ASTeX (PDS17).*

The synthesizer is equipped with a magnetron whose microwave output can be regulated in the range of 600-5000 W. Microwaves emitted by the magnetron *1* at a prescribed output power advance through a waveguide *2* toward an applicator. The microwaves are partially reflected back toward the magnetron. In order to prevent degradation of the magnetron, a circulator *3* for heat-absorbing of the reflected waves in a water load and a dummy load are provided in the waveguide. The impedance of the waveguide *2* is regulated by a three-rod tuner so as to suppress microwave reflection and enable all input electric power to be consumed for producing the plasma. The TE_{01} mode microwaves advancing through the waveguide are converted into concentric TM_{01} mode microwaves as described above by an antenna projecting into the applicator, and then introduced into a reaction chamber *4*. Matching of the microwaves by the conversion to TM_{01} mode leads to a stable plasma ball *5* in the cylindrical reaction chamber *4*. Carbon source gas and hydrogen gas from the gas cylinders pass through pressure reducing valves and further on through mass flow controllers for regulating gas flow into an inlet pipe, supplied to the reaction chamber in suitable reaction gas mixtures. The mass controller for the carbon source gas is a unit enabling the carbon source content of the mixed gas to be regulated for moderate and high methane concentrations.

A turbo pump and a rotary pump are operated to evacuate the interior of the reaction chamber allowing to reach a vacuum $< 10^{-7}$ Torr level, which is necessary to suppress the residual gas phase impurities. During synthesis, gas is evacuated from the reaction chamber by a process pump; the mass controllers are regulated to supply the reaction chamber with reaction gas composed of hydrogen gas having a carbon source concentration of 1%- 15 %. The substrate is cooled allowing working with high power plasma and at the same time keeping the temperature in the range of 600-1200°C by regulating the MW power or the heating/cooling substrate assembly.

The main problem of achieving these ideal plasma surface interactions is optimizing the plasma sheet which is close to the substrate holder. The gas temperature just above the substrate holder decreases dramatically compared to the centre of the plasma ball where at pressures 100 Torr the temperature of about 3000 °K is reached, as determined by OES for the PW power ~1000 W and the power densities 1000 W/cm^3. Because the substrate surface is at about ~700-1000°C, on typically ~ 1 mm distance the concentration and temperatures of carbon radicals is altered enormously. Thus optimization of the exact geometrical configuration of the substrate holder is of primary importance for optimizing the rate reactions described in detail in Chapter 1. Therefore a change in the distance between the substrate surface with respect to the holder surface has detrimental influence on the quality of the homoepitaxial film grown. Another problem encountered is the heat flux, given mainly by the recombination of atomic hydrogen on the substrate surface, that leads to an extensive heating of the substrate. This is limiting the maximum MW powers used.

A related problem is connected to the configuration of the substrate holder geometry, i.e. an important paramater is the minimum the minimum threshold power before the plasma extinguishing supplied to sustain the plasma. For example for pressures of about 1800 Torr with the flat substrate holder this minimum lay in the range of ~ 5000 W. If this full power is transferred to small diamond substrate of dimension 3×3 mm, it would lead in normal conditions to its overheating (temperatures above 1500 °C). Therefore, as one of the innovative approaches in this thesis the substrate holder was redesigned specifically for our experiments. The designed substrate holder was capable to work with small total powers but high plasma densities and tunable substrate temperatures in the range of 600-1200 °C.

The design of the substrate holder was inspired by the possibility of an electric field enhancement by introducing a step-like function object of a small defined size and height compared to the cavity diameter and its bottom closure. In this case, based on the Poisson equation, this additional object leads to concentration of the electric field lines, leading to a local electric field enhancement. This fact of higher electric field density at the same MW power applied is directly translated to the possibility to reduce the MW power to sustain the plasma at certain gas pressure and to generate at the same time plasma of a small diameter just in the region of the concentrated electric field lines (Fig. 2.4.). Using this approach, the substrate holder can be a simple Mo cylinder with a diameter of 5-10 mm, in which the HPHT diamond substrate is embedded, allowing the plasma of typically 600W to be sustained at a pressure of 180 Torr. This allows working with a high plasma density on one side, together with limited heat fluxes towards the substrate.

Figure 2.4: *a) Photograph of the microwave plasma discharge (Reactant gases: 10%* CH_4/H_2*); b) an 'enclosed' holder stage assembly with a substrate inside used for the work in this thesis; c) an 'open' holder configuration.*

Based on the rate equations presented in Chapter 1, the highest possible gas temperature attained, lead in general to the highest atomic hydrogen concentrations. However, the second important parameter, the CH_3 radical production, has been modeled to attain highest concentrations at medium gas temperature [Bri07]. As a result the plasma sheet close to the growing surface was optimized for the preparation of high quality homoepitaxial diamond surfaces.

2.2. Microscopic surface imaging techniques

Homoepitaxial diamond thin films grown are evaluated by different measurements. Specifically several techniques to evaluate the film surface morphology, structure, thickness, defect concentration and their optical and electrical properties were used. The surface morphology of the films was evaluated using Optical Microscopy (OM), Scanning Electron Microscopy (SEM) and Atomic Force Microscopy (AFM), Scanning Tunneling Microscopy (STM), Electrostatic Force Microscopy (EFM). Perfection of the synthesized crystal and presence of crystallographic defects was evaluated by a DiamondView^{TM} apparatus, Cross-polarized Optical Microscopy and Photoluminescence (PL), additionally Cathodoluminescence (CL) spectroscopy, Optical Absorption (AO) and Photocurrent spectroscopy (PC) were used. The electrical characteristics have been measured by Time-of-flight method (TOF).

2.2.1. Optical microscopy

Before each growth experiment and after the deposition of a diamond the surface morphology is usually optically examined. The combination of microscopic techniques is a powerful, easy to use and non-destructive tool for characterising the surface morphology of CVD diamond layer and to gather information about the growth film history. The large scale morphology can simply be determined by aid of a stereo microscope. Details of the structure of the diamond surface can be studied by optical differential interference contrast microscopy (DICM or Nomarski contrast) and scanning electron microscopy (SEM). Whereas DICM allows for the identification of small differences in height, such as macro steps, round hillocks or etch pits on the diamond surface in the plane of focus, the large focus depth obtained by SEM is most suited to study three dimensional features, such as the shape of the crystallites in the diamond layer.

2.2.1.1. Differential interference contrast microscopy

Differential interference contrast converts optical path gradients into amplitude differences that can be visualized as an improved contrast in the resulting image. The optical components required for differential interference contrast microscopy enable the instrument to be employed at full numerical aperture. The result is a dramatic improvement in resolution (particularly in the direction of the optical axis), elimination of halo artifacts, and the ability to produce excellent three dimensional images with relatively thick specimens. In addition, differential interference contrast produces an image that can be easily manipulated using digital and video imaging techniques to further enhance contrast.

A schematic view of such an apparatus is shown in Fig. 2.5. A polarizer after a white light source is used to set the angle of the polarized light incident upon a Wollaston prism. The Wollaston prism splits the light into two beams having orthogonal polarization, which are sheared with respect to one another. After reflection off the test surface the Wollaston prism recombines the two beams. A fixed analyzer placed after the Wollaston prism transmits components of the two polarizations and generates an interference pattern.

The resulting image shows the difference between two closely spaced points on the test surface.

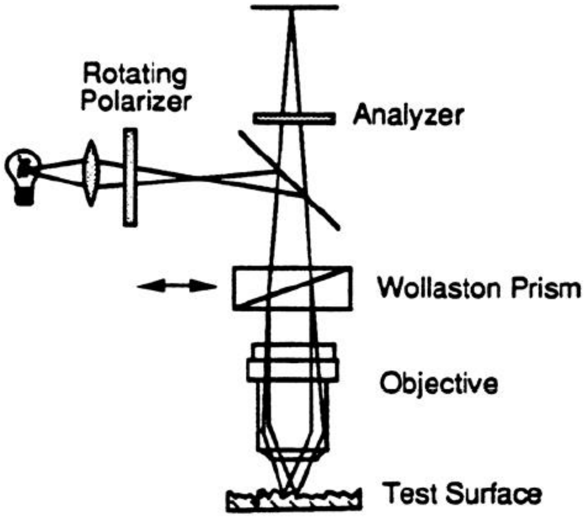

Figure 2.5: *Schematic of a DICM optical microscope.*

The point separation is usually comparable to the optical resolution of the microscope objective and hence only one image is seen. In any part of the specimen in which adjacent regions differ in refractive index the two beams are delayed or refracted differently. When the images are recombined by a second prism in the objective lens there are differences in brightness corresponding to differences in refractive index or thickness in the specimen.

The image shows the slope changes and it appears as though the surface has been illuminated from one side. The path difference between the two beams can be adjusted by laterally translating the Wollaston prism. When the axes of the polarizer and analyzer are parallel and the prism is centered, the path lengths are equal and white light is seen for a perfect test surface with no tilt. When the polarizer and analyzer are crossed and the prism centered, no light gets through. When the prism is translated sideways, the two beams have unequal paths and different colors are seen. The color for a specific feature on the test surface depends upon the path difference between the two beams for that point. The color changes indicate the surface slopes. When the polarizer before the prism is rotated, the relative intensities of the two orthogonal polarized beams change, and the colors change. When the contrast is optimized one can obtain a very distinct image that appears three dimensionally.

2.2.1.2. Cross-polarized light microscopy

Investigation of the samples under cross-polarized light used in this thesis provided information about the specific strain patterns in the SCCVD films and their growth history in order to understand the growth mechanism.

Polarized light is a contrast-enhancing technique that improves the quality of the image obtained with birefringent materials when compared to other techniques such as bright field illumination, differential interference contrast etc.

The polarized light microscope is designed to observe and photograph specimens that are visible primarily due to their optically anisotropic character. In order to accomplish this task, the microscope must be equipped with both a *polarizer*, positioned in the light path somewhere before the specimen, and an *analyzer* (a second polarizer), and placed in the optical pathway between the objective rear aperture and the observation tubes or camera port. Image contrast arises from the interaction of plane-polarized light with a *birefringent* (or doubly-refracting) specimen to produce two individual wave components that are each polarized in mutually perpendicular planes. The velocities of these components are different and vary with the propagation direction through the specimen. After exiting the specimen, the light components become out of phase, but are recombined with constructive and destructive interference when they pass through the analyzer.

When both the analyzer and polarizer are inserted into the optical path, their vibration azimuths are positioned at right angles to each other. In this configuration, the polarizer and analyzer are said to be *crossed*, with no light passing through the system and a dark view field present in the eyepieces.

In *crossed polarized illumination*, isotropic materials can be easily distinguished from anisotropic materials as they remain permanently in extinction (remain dark) when the stage is rotated through 360 degrees. Therefore the technique can reveal information about thermal history and the stresses and strains to which a specimen was subjected during formation.

2.2.2. Scanning electron microscopy

The electron microscope uses electrostatic and electromagnetic lenses to control the illumination and imaging of the specimen. By scanning a focused beam of electrons across a sample an image can be constructed by detecting the secondary and / or back scattered electrons. The penetration depth of the electron beam depends on the electric field and it for diamond is in the order of several microns for ~20 kV beams.

Secondary electrons (SE) can be generated by the interaction of the incident electron beam and weakly bonded electrons within the sample being studied. Secondary electrons are of low energy and are only emitted from the approximately the top 10 nm thickness of the film. This low energy also means that they are influenced by electromagnetic fields and hence can be accelerated to the detector even if there emission is not in the direction of the detector.

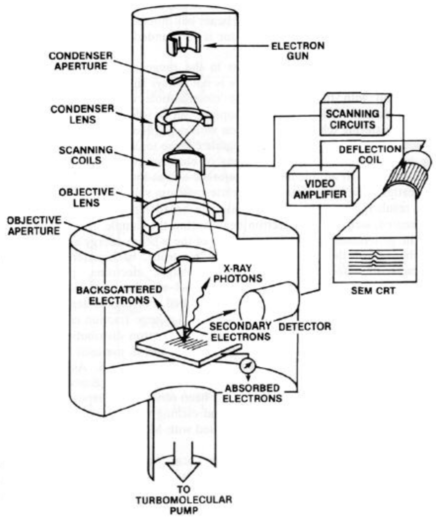

Figure 2.6: *Schematic of a SEM microscope [You86].*

Back scattered electrons (BSE) can also be used for imaging. There are of high energies as they are due to elastic collisions between the incident beam and relatively tightly bound electrons in the specimen. BSE emission intensity increase with increasing atomic number and can be used to differentiate regions of different elements.

A schematic of the apparatus is shown in Fig. 2.6. Electrons are generated by thermionic emission in the electron gun and are accelerated using a positive bias of around 20-40 keV on the condenser aperture. On passing through the aperture they are then focused into a tight beam by the condenser lens and scanned across the sample using the scanning lens. Focusing is assisted by the objective lens. Secondary electrons or BSE are collected by the detector and are amplified and projected on the cathode ray tube (CRT).

The entire electron system has to be contained within a high vacuum to maintain a useable mean free path. Also, as electrons are emitted the sample can become charged thus reducing subsequent emission. Hence insulating samples are coated with a thin layer of gold. Typical SEM has a beam diameter of around 1 – 10 nm but resolution is ultimately limited by the broadening of the beam due to scattering at the sample surface.

2.2.3. Scanning probe microscopy

Scanning probe microscopes (SPMs) are a family of instruments used for studying surface properties of materials from the atomic to the micron level. All SPMs contain the components illustrated in Fig. 2.7. Scanning-probe microscopy refers to a class of techniques in which a very fine needle nano-size probe (SPM tip) is mechanically moved across the surface of a sample in a series of straight lines (scans). The interaction of the probe with the surface is recorded as a function of position on the surface; hence the nature of the surface is determined in a very direct manner. With these *microscopes* direct images on nm resolution are produced, although it is only feasible to probe a very small surface area on the sample. Many different types of probe/surface interaction can be recorded, corresponding to different *modes* of operation. Three important modes will now be described.

2.2.3.1. Atomic force microscopy (AFM)

In an AFM apparatus, the probe tip is mounted onto a very sensitive piezoelectrically controlled mechanical cantilever As the probe is scanned across the sample, the force existing between the top atoms at the tip and those of the sample's surface causes deflection of the cantilever, which is typically detected by reflecting a laser beam from the top of the cantilever. In practice, a feedback loop is used to move the cantilever/probe up and down such that a constant force (deflection) is maintained, and the height required is recorded as a function of surface coordinate. This way, one can ensure that only small cantilever deflections occur, which keeps the theoretical calculation of forces accurate. In addition, this prevents damage to the surface which could arise from the large forces of a greatly strained cantilever. As will be seen, one advantage that AFM has over other scanning probe microscopes is that both electrically conducting and non-conducting surfaces can be investigated. It is interesting to note that work has recently been undertaken to manufacture AFM probes out of diamond [Shi99].

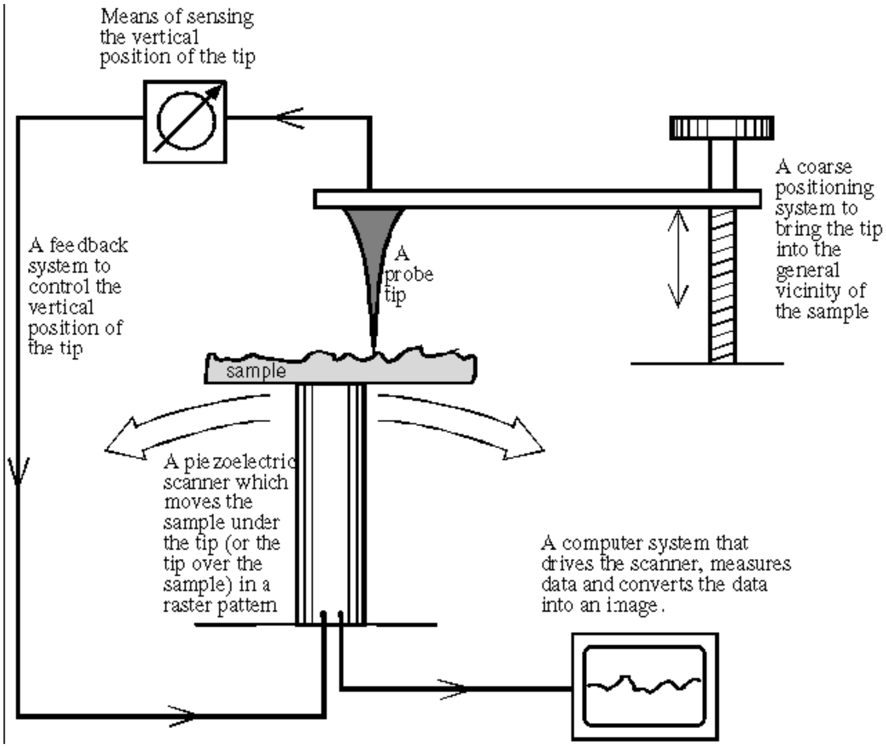

Figure 2.7: *Schematic of a generalized SPM [Sch98].*

AFM provides high magnification three-dimensional images of solid surfaces, similar in appearance to the STM images described in the section below. At maximum resolution, AFM can be used to examine surface reconstruction and this even with atomic resolution leading to imaging of atomic steps, features crucial for providing insight on the mechanism of diamond growth. Increasing the scan size allows profilometry of larger scale features such as surface roughness. AFM requires a clean surface, suggesting measurements should be performed under ultrahigh vacuum, however, in case of epitaxial diamond no significant sample preparation is required for AFM as the as-grown diamond surface is terminated by hydrocarbons, hydrogen or oxygen. The key to the technique is the precise translation of a sharp tip and measurement of vertical displacement due to attractive and repulsive forces between the tip and the surfaces. Most of the AFM studies of diamond surfaces can be routinely performed in air. The (100) surface is apparently remarkably stable and no differences in image were observed before and after a surface cleaning in boiling acids. Horizontal scan dimensions used varied in the range between 0.5 to 65 μm. This is in contracts to STM (see below), where a maximum resolution requires a clean and sufficiently electrically conducting surface; other requiring measurements should be performed under ultrahigh vacuum to remove surface adsorbates such as water.

2.2.3.2. Scanning tunneling microscopy (STM)

Spatial resolution greater than that offered by AFM is possible by using the STM mode. Provided that the surface material is conductive, a voltage can be put across the probe (typically made of platinum-rhodium or tungsten) and the sample, and the weak current due to electrons tunneling from one side to the other can be recorded during scans. Because the tunneling current decreases exponentially with distance between the tip of the probe and the atoms of the surface, a very accurate height map can be constructed for the region under investigation. STM is capable of resolving distances of around 2 Å, hence it offers atomic-scale resolution for many conductive substrates.

In the STM experiment, electrons tunnel between a sharp tip and a surface, requiring the tip-to-sample separation to be just a few angstroms. The magnitude for the tunnel current depends on the tip-to-sample distance, allowing the 3D topography of the surface to be profiled. The tunnel current also depends on the local density of electronic states at the surface. The bias voltage used selects which of these electronic states are involved in tunneling and the direction of current flow.

Both vertical and horizontal resolution of STM can approach 1Å for a square area 100 Å on a side. The small lattice constant of diamond makes atomic scale resolution inherently challenging. Images over larger regions (1 mm per side) can be made at lower resolution. Typically, recording an image requires only several minutes. The STM experiment can be eventually performed under atmospheric conditions using an electrically conductive surface. However, the use of ultrahigh vacuum (UHV) for STM experiments generally improves the maximum resolution obtainable by providing a clean surface for observation without the surface adsorbents such as the water. Surface roughness can also be quantified via STM. Additionally when using the derivative of the measured current as a function of differential changes of the tip applied voltage, scanning tunneling spectroscopy modes can be assessed, giving the information about the surface density of states.

2.3. Defect spectroscopy techniques

The main objective of this paragraph is a brief description of techniques to study the defects in CVD diamond. To measure optical absorption of high quality CVD diamond films, which are additionally thin, sensitive techniques have to be applied. Such defect spectroscopy techniques allow finding the electronic structure of the defects and eventually energy position of such defect in the forbidden gap of CVD diamond. The spectroscopic techniques used in this can be divided to optical, electrical, photoelectrical and magnetic. Specifically, photoluminescence, optical absorption, magnetic resonance and photocurrent are used to study defects in single crystal CVD diamond films.

2.3.1. Photo and electro-luminescence (PL/EL)

Luminescence refers to the emission of photons when a system in an excited electronic state relaxes into a state of lower energy. In photoluminescence (PL), the initial excited state can be produced by photon irradiation of the sample while in other important mode (cathodoluminescence) the photon is produced by interaction with another source of irradiation, such as upcoming electron, produced for example in a cathode of electron microscope. In general, several other methods of excitation can be used, including, electro, and thermo luminescence, wherein the excited state is produced by respectively using accelerated electrons, electric fields, and heating etc.. For a review one should consult, for example, refs.[Dav81, Dav99, Lig90].

PL techniques used in this thesis were mainly carried out in collaboration with Hoge Raad Diamant (HRD) in Antwerp, working with several laser sources and ranging from UV (above band gap) to visible light illumination. Some of these techniques were also used for a direct imaging of crystals.

In this work PL was used in several modes:

In “*above-bandgap*” PL, the sample is irradiated with photons of energy greater than the material's bandgap (5.46 eV), so that electron-hole pairs are created. The electrons rapidly thermalise to the bottom of the conduction band (and the holes to the top of the valence band), and they are also available for interactions with any available defect states of lower energy, such as those offered by defects. These relaxations may proceed via radiative mechanisms, although also non-radiative processes are possible and often more likely. The electrons eventually recombine with holes in the valence band or in defect states, and this recombination is accompanied by the emission of a photon with energy equal to the difference in the excited and ground electronic states. In cases where the excited state has a long radiative lifetime, or where the transition to the ground state is forbidden by symmetry, transitions may be instead observed as originating from a higher excited state. One of the principal differences between PL and optical absorption techniques (such as FTIR, discussed later) is the way in which they reveal the presence of multiple excited states. Absorption methods can in principle detect all excited states (into which the transition from the ground state is allowed by symmetry) by simply illuminating the sample with multichromatic radiation and recording the absorption as the difference between the incident and transmitted spectra. On the other hand, PL reveals excited states in a more indirect manner, based on the radiative recombination efficiency of the excited charge carriers only.

In ***"gap illumination"*** **PL**, photons with lower energy than the band gap energy are used, thus electrons occupying a defect state are directly excited to its excited state and their recombination leads to an observation of a specific PL, which is related to the radiative recombination of via defect states. Other local phonon vibrational modes can be involved in these excitations, interacting with the excited electrons. These modes are called vibronic transitions [Fie92].

Related technique used for sub-gap light experiments is *photoluminescence excitation* (PLE). The sample is irradiated for example by light from a tunable laser, while the luminescence detector is set to record outgoing photons of a specific energy, say that corresponding to the transition from the lowest (first) excited state into the ground state. The energy of the incident radiation is gradually changed), and the intensity of the particular luminescence is measured byt a observed by the detector. This technique is useful to study the energy needed to excite various defects. In general a first luminescence line is due to the first excited state ground state luminescence itself. As the incident light wavelength is decreased (energy increased), electrons will be promoted from the ground state into the second excited state, but will relax (most likely non-radiatively) into the first excited state, increasing its population.. At greater incident energies, the higher energy state can be excited and these electrons will relax. The spectrum of luminescence intensity as a function of incident radiation frequency will therefore contain peaks corresponding to the specific excited states present. The PLE technique is suitable for the characterization of thin samples or those with low defect concentrations, where absorption experiments can be difficult to interpret due to the low signals.

2.3.2. Infrared spectroscopy (IR)

The IR region of the electromagnetic (EM) spectrum covers wavelengths in the range of about 750 nm to 1 mm, corresponding to photon energies of about 1.2 meV to 1.7 eV. Photons with energies between about 0.05 and 0.50 eV are capable of exciting vibrational modes in typical covalently bonded solids, and so such photons may be absorbed when used to irradiate a sample. By recording a spectrum of absorption against input EM radiation wavelength, the energies of the allowed vibrational modes in a sample can be determined. Absorption or transmission is conventionally plotted against wave*number*, the latter varying over about 400 - 4000 cm^{-1}. The allowed vibrational mode frequencies will depend on bond lengths, bond angles (that is, orientation with respect to the surrounding atoms), the masses and interatomic potentials of the atoms involved, and the *type* of vibrational mode. In the context of two bonds that share one parent atom, there are six types of vibrational mode: two types of bond *stretching* (symmetric and asymmetric), and four types of bond *bending* (rocking, scissoring, wagging, and twisting). As with many other spectroscopic techniques, the peaks in a recorded spectrum are compared against those from samples of known composition in order to identify the bond types present. In case of diamond most important lines are the C-H modes, C-O modes and intrinsic modes such as 2 and 3 phonon absorption region (341-349 meV).

The key to the absorption process is the fact that the vibrating bond must involve a changing dipole in order to absorb the EM radiation. In general, this often means that the two atoms making the bond must be of different chemical species. The inevitable asymmetry in charge distribution between the two types of atom causes an electric dipole, the strength of which will oscillate as the bond vibrates with its natural frequency. The oscillating electric field present in the incident EM radiation can interact with the oscillating dipolar bond, and if the frequencies match, the photon energy will be absorbed, causing the bond to vibrate with greater amplitude. The result is that, in a monatomic solid such as diamond, the IR absorption process is very sensitive to the presence of defects, and in particular to bonds between atoms of the host material and impurity species.

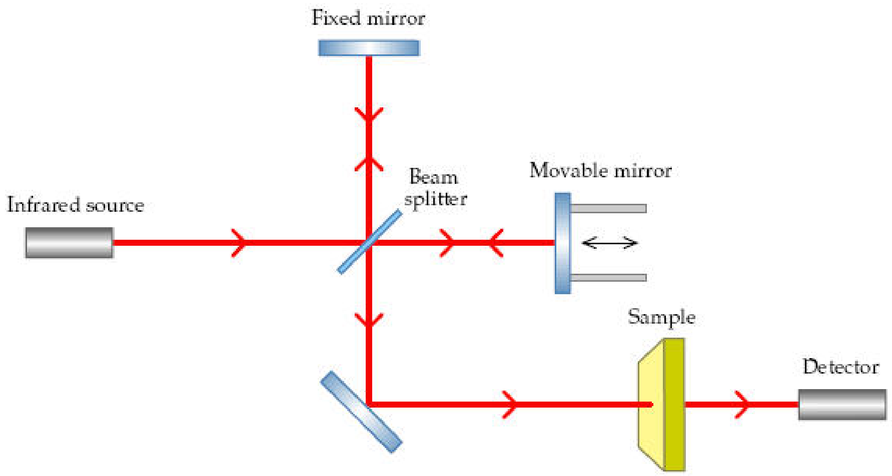

Figure 2.9: *Schematic of the apparatus for an FTIR study.*

The apparatus for FTIR, which is most commonly used for the IR absorption investigation is based on the *Michelson interferometer* and is shown schematically in Fig. 2.9. First, the IR radiation is directed as a parallel beam toward a beam splitter (a `half-silvered' mirror). This component reflects about 50% of the radiation down a path toward a fixed mirror, and transmits the remaining 50% down another path toward a second, movable mirror. These (fully silvered) mirrors reflect the beams back normally, to be recombined at the beam splitter. Here, half of the total is transmitted back toward the source and is discarded, and the other half is reflected down a new path, ultimately to be directed at the sample under investigation.

In addition to vibrational modes the absorption spectra in the mid infrared region can give us the information about the defects and impurities by monitoring their direct transition from the defect level to the conduction band minimum (electrons) or valence max maximum (holes). This defect transition can be treated based on the optical cross-section model of impurities which gives and energetically dependent interaction of light with the defect center. Such models have been used in CVD diamond to model absorption of nitrogen, phosphorus, boron and other impurities. The ionization energy which corresponds to the energy position of the defect in the forbidden gap of diamond is thus important information for defect diagnostics. For example the ionization energies of N, P, and B, are 1.7, 0.6, 0.37 eV respectively. However, when measuring such a defect concentration on ppm scale the simple FTIR transmission/absorption is not sensitive enough and one has to use other techniques such as photo-thermal deflection spectroscopy (PDS) or photocurrent based (PC) techniques. The PDS, similar to optical absorption measures all possible optical transition occurring within the material. The PC technique is discussed in Chapter 4.

2.3.3. Fourier-transform photocurrent spectroscopy (FTPS)

The Fourier-transform photocurrent (FTPS) technique has been used in this thesis based on its outstanding sensitivity in the IR spectral region [Lif93]. FTPC is based on traditional Fourier Transform Infra-red Spectroscopy FTIR spectroscopy [Gri86] (a system using transmittance/reflectance measurements), and, as a result, has 3 operating advantages: short acquisition time, high resolution and high light throughput giving good signal to noise ratio [Van02]. In the FTPS the photocurrent is measured under broad band illumination and its spectrum is calculated by computer from interference effects measured as a function of the optical path difference between the fixed and moving mirrors of the Michelson interferometer (interferogram), described above.

In first FTPS versions the photocurrent signal was measured using the continuous scan of the moving mirror using the dc amplification system. Recently a new technique has been developed [Rem07], applied here, which is called Amplitude modulated step scan Fourier transform photocurrent spectroscopy (AMFTPS) that provides higher sensitivity and new possibilities to characterize defects in intrinsic diamond namely the quantitative defect analysis of thin diamond layers.

The experimental setup for AMFTPS experiment is shown in Fig. 2.10. A Nicolet 8700 FTIR spectrometer is used for the step-scan amplitude modulation (AM) experiment, the intensity of the IR light is modulated periodically by mechanical chopping. The photocurrent from the sample is first fed externally to a lock-in amplifier referenced to the same modulation frequency. The analog output from the lock-in amplifier is connected to the external analog input of the FTIR spectrometer. Prior the interferogram scan, the lock-in output is off-set to zero. The maximized in phase signal is then digitized, recorded as an interferogram and Fourier transformed to obtain the photocurrent spectrum. The amplitude modulation allows the AC frequency to be tuned in a relatively wide range of frequencies from 10 to 10 kHz. This principle allows measuring practically all diamond samples even at very low (fA) photocurrent levels of the total IR photocurrent [Rem07].

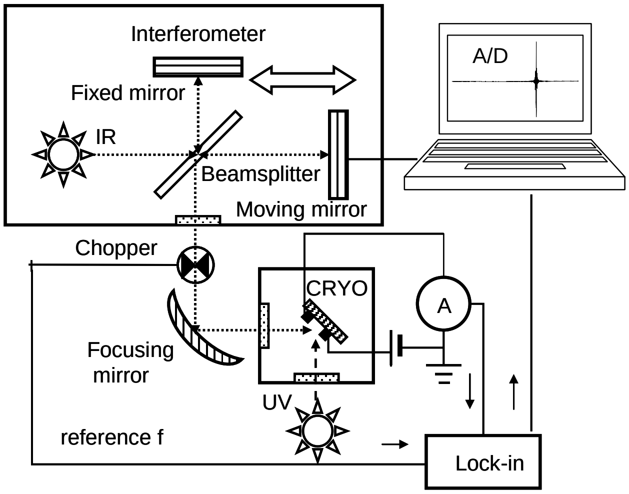

Figure 2.10: *Experimental setup for the AMFTPS: the interferometer with IR source, beamsplitter, fixed and moving mirrors, chopper, sample placed onto a cold finger of the cryostat, stable voltage source, current preamplifier (A), lock-in amplifier and A/D converter. The computer records the AC photocurrent amplitude as a function of the moving mirror retardation. 30W deuterium lamp can provide UV bias light*

2.3.4. Electron paramagnetic resonance (EPR)

In most solids, including diamond, electron spins are *paired* in the chemical bonds; that is, there are exactly as many spin-up electrons as there are spin-down, and the material has no net spin. Therefore there is no net electronic magnetic moment, and no interaction between the electron spins and any applied magnetic field. However, if impurity atoms are present, they may introduce unpaired electrons, in which case the material can be paramagnetic containing a number of unpaired spins, which under the influence of external magnetic filed can align giving rise so called *electron spin resonance* (ESR) or *electron paramagnetic resonance* (EPR). EPR thus detects defects which have an unpaired electron. In diamond, unpaired electrons are often localized at impurity atom sites or at lattice defects such as vacancies. Detailed information can be obtained about the identities of the atoms and symmetry, which surrounds the unpaired electron. Paramagnetic defects in diamond are often also optically active.

An EPR peak is observed when microwaves are applied at the resonance frequency of the unpaired electron in an external magnetic field. This resonance frequency is proportional to g, the spectroscopic splitting factor g. For a free electron, g=2.0023. Shifts from this value are indicative of the orbital contribution to magnetic momentum of the defect. Anisotropy in the g-value, evidenced by the orientational dependence of the EPR spectra, provides information on the symmetry of a defect and thus can be used to probe the local distortion in lattice geometry at the defect site.

A nucleus having angular momentum which is in the proximity of the paramagnetic defect can often be identified as a result of hyperfine interactions. The strength and orientation dependence of hyperfine couplings depend on the location of the nuclear spin (or spins) with respect to the unpaired electron. This gives possibility to diagnose precisely the type of nucleus, based on the EPR data. The ability to resolve g values and hyperfine coupling constants depends on the linewidths in the EPR spectra. Paramagnetic defect concentrations can be determined from the integrated intensity of the corresponding EPR peak. Sensitivity limits of 10^{10} cm^{-3} have been achieved for room temperature EPR measurements and improve inversely with temperature.

For example, an isolated impurity nitrogen atom, substituted for carbon in the diamond lattice, is known as a P1 center. The resonance frequency of a P1 center corresponds to g=2.0024, close to the free electron value. Analysis of the axially symmetric hyperfine couplings reveals that the unpaired electron occupies an antibonding orbital pointed along the C-N bond direction, and is localized primarily on the carbon atom.

The upper part of Fig. 2.11. shows a schematic absorption peak for an EPR experiment. To help in characterizing peaks such as this, most ESR systems run in derivative mode, as shown in the lower part of the figure. The linewidth ΔB is defined as the difference B_2 - B_1 between the positions of two peaks in the derivative spectrum, while the amplitude A is the peak-to-peak height. The integrated intensity can then be approximated by $\Delta B \times A$, which is proportional to the concentration of the paramagnetic species present. To get quantitative data from the integrated peak intensities, one must perform a calibration by using a sample for which the concentration of paramagnetic centers is known.

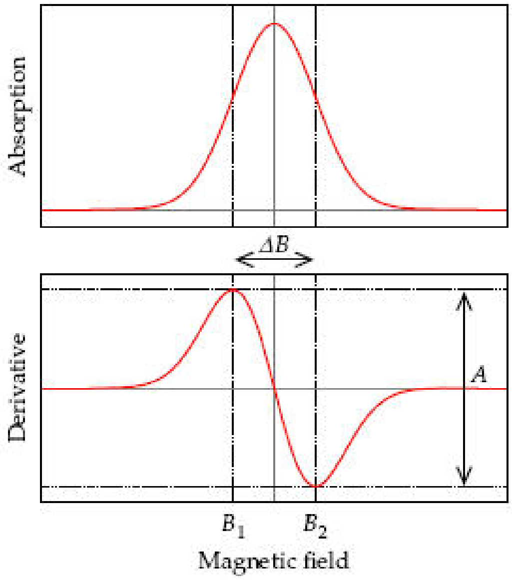

Figure 2.11: *Schematic of an absorption peak in an ESR experiment, shown in normal mode (upper plot) and derivative mode (lower plot).*

2.3.5. Micro-Raman spectroscopy

Laser Raman spectroscopy is a useful method for material identification. It is a straightforward, non-destructive technique requiring no large sample preparation. The Raman technique consists in illuminating a specimen with strong monochromatic light and in examining the non-linearly scattered light (Raman effect) by using a spectrometer. When electromagnetic radiation is scattered by a molecule or by a crystal, one photon of the incident radiation is annihilated and, at the same time, one photon of the scattered radiation is created. The scattering mechanisms can be classified on the basis of the difference between the energies of the incident and scattered photons. If the energy of the incident photon is equal to that of the scattered one, the process is called *Rayleigh scattering*. If the energy of the incident photon is different from that of the scattered one, the process is inelastic and it is called *Raman scattering*. Raman scattering was discovered experimentally in 1928 [Ram30]. When the light is scattered to lower energy the lines are called Stokes lines, the others, having higher energy are anti-

Stokes lines. A Raman spectrum is plotted as the intensity versus the difference in wavenumber between the incident radiation and the scattered light.

Natural diamonds exhibit a sharp first-order peak (triply degenerate) in the Raman spectrum at ~ 1332.44 cm^{-1} and a weak second-order feature centered at ~ 2750 cm^{-1} [Sol70]. In principle, the first order peak should have a Lorentzian line shape with full-width at half maximum (FWHM) typically ≤ 2 cm^{-1}. In diamond films grown by HPHT or CVD methods, various growth sectors can contain different concentration of defects and carbon in non-diamond forms. These non-diamond carbons may be graphitic [Zhu89, Nem88] or amorphous carbon [Fay94]. Raman scattering and photoluminescence spectroscopy enable the study and the characterization of these impurities and of structural imperfections in diamond [Bac92, Col92]. Recent improvements in the implementation of the Raman technique make also Raman spectroscopic imaging possible. In particular, images with spatial resolution better than 1 μm can be produced within few hours thanks to the availability of high-efficiency detectors and fast acquisition programs.

2.3.5.1. Micro-Raman experimental set-up

Initial confocal Raman spectra from the top face of the homoepitaxial diamond films were obtained in the Laboratory for Solid State Physics and Magnetism at the Katholieke Universiteit Leuven in order to assess the sample crystallinity. Raman mapping and luminescence measurements were performed at the Laboratoire d'Electrochimie et de Physique-chimie des Matériaux et des Interfaces of CNRS. The setups were principally similar. In Grenoble, the experimental set-up consists of a Jobin-Yvon/Horiba T64000 triple monochromator spectrometer equipped with a liquid nitrogen cooled multichannel CCD detector (1024 × 256 pixels) and a microscope to which a computer-driven XY table was attached. This gave the possibility to draw two-dimensional (2D) images. A piezoelectric device (accuracy better than 0.1 μm) allows varying the vertical distance between the objective and the sample surface for performing in-depth profile measurements. Different Argon lines (514.5 nm, 488 nm and 457.9 nm) from an Argon-Krypton ion laser were used as excitation source. During the experiments, all performed at room temperature, the power of the incident light was adjusted to avoid heating effects. No differences about the position of the diamond Raman peak have been detected, so heating induced by the laser light could be excluded as the origin of variations in the peak position. For microscopic spectral measurements, different magnifications objectives ×10 (numerical aperture = 0.25), ×50 (numerical aperture = 0.9) and ×100 (numerical aperture = 0.95) were used. A confocal diaphragm adjustable in size from 20 to 1000 μm provided the lateral and axial resolution of the measurements. For the ×100 objective, a 200 μm confocal diaphragm value corresponded to a sampling volume of approximately 0.7 μm in diameter and 2 μm in thickness. However, because of the high refractive index of diamond, the sampling volume was slightly higher. When using the ×10 objective, the probing depth in transparent materials was assessed to be larger than 100 μm. The ×10 objective was mostly used to get an estimate of the sample bulk characteristics and to record optical images by using light reflected from the sample and light transmitted through the transparent sample. This simple optical analysis allowed having a first indication on the surface morphology, as from the coloring it was particularly easy to identify the presence of impurities such as nitrogen. In some cases, crossed-polarization birefringence images were also acquired as they provide information about the existence of strain in the crystal. For photoluminescence measurements, spectra were only roughly corrected for instrument response.

When Raman (or photoluminescence) mapping was performed, full spectra were recorded for each point and then stored in an "image file". Therefore, data contained the complete information locally resolved within the studied spectral window and sample area. The width of the spectral window depended on the excitation wavelength and especially on the acquisition mode of the spectrometer: single spectrograph (2000 cm^{-1}), double subtractive (600 cm^{-1}) or triple additive mode (200 cm^{-1}). If necessary, measuring conditions may be chosen to ensure wavenumber shift accuracy better than 0.02 cm^{-1}.

2.3.6. Time-of-flight (TOF)

The electrical transport properties of diamond are strongly influenced by the presence of intrinsic defects, and extrinsic contaminants or dopants, most prominently nitrogen, silicon, boron and phosphorous, as well as different structural morphologies. Because undoped diamond is an isolator with a very high resistivity, the electrical charge mobility can not directly be measured using Hall-effect at room temperature. Therefore alternative methods for studying the electrical transport have to be used.

Transient photoconductivity Time-of-flight (TOF) measurements were applied in this thesis in order to measure the transport properties (mobility) of electrons and holes and to understand the charge transport and charge trapping kinetics with respect to the defects and impurities.

In the TOF setup UV light has been used to generate electron-hole pairs. Due to the strong absorption of a short laser flash with a photon energy above the diamond band gap the electron-hole pairs are generated in a narrow sheet, which is very close to the top surface of the sample. The UV laser source is based onto the third harmonic generated 2.7 ns pulses from a Nd:YAG laser pumping an UV doubled optical paramagnetic oscillator crystal. The laser pulse, generated by this technique has a wavelength of 215–220 nm, which is just above the band gap energy of intrinsic diamond. By using this UV pulsed light, a sheet of carriers is generated in the first 10 μm of the diamond layer. The sample is equipped with 2 blocking contacts (on the top and bottom surface) and the voltage is applied.

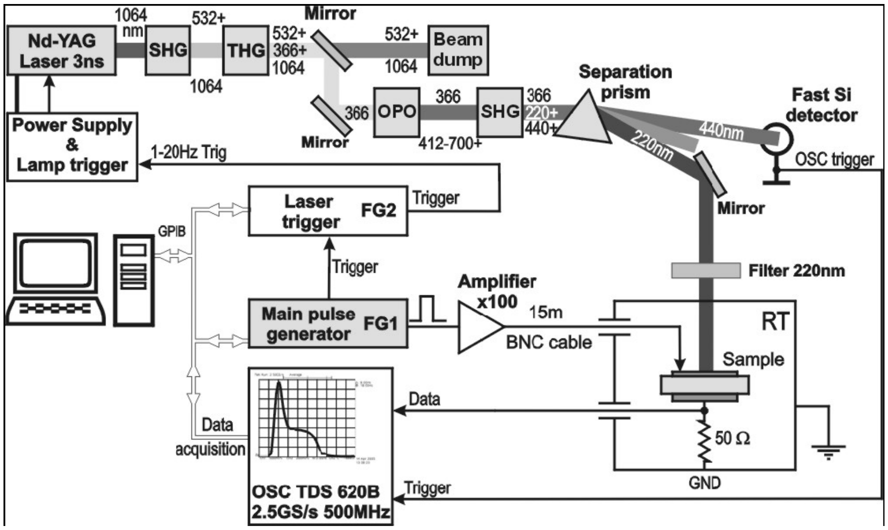

Figure 2.12: *Time-of-flight set-up. Nb:YAG pumped optical paramagnetic oscillator (OPO), tuneable from 420 till 700 nm is doubled by BBO crystals. The Si-detector is used as a trigger for the oscilloscope (OSC). FG1, FG2 are function generators: FG1 is producing a main voltage pulse (4ms length) that is 100x amplified and applied to the sample. FG2 is a delaying trigger for the Q-laser-switch. A 15m long coaxial cable is used to dump and shift the reflections on the voltage input side of the sample. The current is measured using a 50 Ohm impedance matched line.*

When a voltage is applied between the top and the back contacts after a laser flash, the carriers are generated and directly separated. While the upper electrode collects one polarity of the carriers the other polarity carriers are transported through the bulk of the sample towards the collection electrode. The carriers travel through the diamond from the top contact to the bottom contact under an electric field which we have varied from 0.3 V/µm to 1.4 V/µm. The 3 ms pulsed electric field was applied to the sample assuring a homogeneous electric field before dielectric relaxation occurs. The laser pulse was delayed by 50 µs to reduce any induced electric noise and to ensure a good match between electric field and laser pulse. The measurements were recorded using a 500 MHz digital oscilloscope and an averaging was done over 25 measurements to reduce the noise according to the signal. Schematic diagram of the laser Time-of-flight (TOF) measurements set-up is depicted in Fig.2.12.

These carriers arrival occurs at the electrode at the so-called *transit time*, this time allows calculating the carrier mobility. Therefore TOF is used to study the transport mobility and transport mechanism of intrinsic SCCVD diamond. Namely, the Time-of-flight (TOF) technique was used to measure the electron and hole mobility of the diamond samples grown at different conditions.

2.4. Gemological techniques

In the experiments carried out on the CVD free standing diamond crystals prepared in this thesis, also gemological characterization techniques have been used. These techniques have been carried out at HRD in Antwerp using the DiamondView™ instruments, developed by the Diamond Trading Company Limited (DTC). The gemological quality assessment is important as it allows the gemological characteristics directly relate to the crystallographic defects in diamond.

DiamondView™ works by producing a fluorescence image of diamond (Fig. 2.13.(a,b)). Specifically, DiamondView™ uses a camera to display the fluorescence pattern created on the surface of a diamond after it has been exposed to shortwave UV light. Given that the fluorescence colors and patterns from synthetic HPHT and CVD diamonds differ greatly from those of natural diamonds, DiamondView™ makes it possible for gemological laboratories and jewelry professionals to determine whether a diamond is natural or synthetic. CVD synthetics exhibit unique fluorescence characteristics, which allow their separation from HPHT and natural diamonds. Near colorless synthetics (both

HPHT grown and CVD) are very difficult to manufacture but have been produced on an experimental basis for research. DiamondView™ is used under license and developed by The Diamond Trading Company Limited.

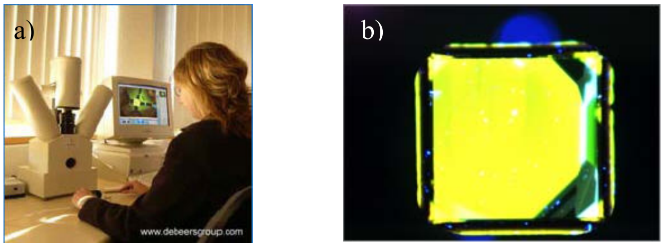

Figure 2.13: *a) DiamondView™ apparatus, b) DiamondView™ picture of a CVD homoepitaxial film attached to its HPHT Ib diamond substrate.*

To characterize colors of the CVD diamond samples grown we have used a Gran colorimeter. It should be noted that the color of diamond is related both to extrinsic defects and impurities, inclusions and light scattering centres. Thus monitoring the color of CVD diamond gives important information about the physics of defects in CVD diamond films grown.

The Gran colorimeter was first developed by Paul Gran in 1972 at Gran Computer Industries Ltd. The color of a diamond refers to the tone and saturation of color, or the depth of color in a diamond. The color of a diamond can range from colorless to a yellow or brown hue. A more colorless diamond is rarer and more valuable because it appears white and brighter to the eye. The HRD color grade scale classifies diamond color into 22 grades from letter grade D (colorless) through letter grade Z (fancy color). When color is determined using the Gran Colorimeter device, it measures from the color D to Z to Fancy Intense colors with an accuracy within ±½ of a color grade on loose stones from 0.25 to 10 carats (50 to 2000 mg) (as low as 0.15 carat (30 mg) or as high as 20 carats (4 g) with reduced accuracy), and one can specify which grading scale it should use (GIA, GEM, IGI, AGS, HRD, and other internationally recognized laboratories). The accuracy is within ±1 color grade for mounted stones. If a diamond is a "G" color the machine will tell whether it's a "high G" or a "low G." Usually the color determination is done on cut stones but not on thin films or plates. Therefore the obtained color might thus be different when a CVD plate would be used for a cut stone. Hence, this in combination with defect spectroscopy gives a good hint how the color of CVD plates compares with different concentrations of defect levels evaluated precisely by a defect spectroscopy.

2.5. References

[Bac92] P.K. Backmann , D.U. Wiechert, Diam. Rel. Mater. **1**(1992), 422.

[Bad90] A. J. Baden-Fuller, *Microwaves: An introduction to microwave theory and techniques,* (1990), Chapter 5.

[Bri07] O. Brinza, J. Achard, F. Silva, X. Duten, A. Michau, K. Hassouni, A. Gicquel, Physica Status Solid **204**(9) (2007), 2847.

[Col92] A.T. Collins, Diam. Rel. Mater. **1** (1992), 457.

[Dav81] G. Davies, The Jahn-Teller effect and vibronic coupling at deep levels in diamond, Rep. Prog. Phys. **44(7)** (1981), 787.

[Dav99] G. Davies, in Identification of Defects in Semiconductors, Vol. 51B of Semiconductors and Semimetals, edited by M. Stavola, Academic Press, New York, 1999, Chap. 1, p. 1.

[Fay94] L. Fayette, B. Marcus, M. Mermoux, L. Abello, and G. Lucazeau, *Diam. Relat. Mater.* **3** (1994) 438

[Fie92] J. E. Field, The Properties of Natural and Synthetic Diamond, Academic Press, London, (1992).

[Gic94] A. Gicquel, K. Hassouni, S. Farhat, Y. Breton, C. D. Scott,M. Lefebvre, M. Pealat, Diamond Relat. Mater. **3** (1994), 581.

[Gri86] P.R. Griffiths, J.A. de Haseth, Fourier Transform Infrared Spectroscopy., Wiley, New York (1986).

[Kam83] M. Kamo, U. Sato, S. Matsumoto, N. Setaka, J. Cryst. Growth, **62** (1983), 642.

[Lif93] T.M. Lifshits, Instrum. Exp. Tech. **36(1)** (1993), 1.

[Lig90] E. C. Lightowlers, in Growth and Characterisation of Semiconductors, edited by R. A. Stradling, P. C. Klipstein Adam Hilger, Bristol, 1990, Chap. 5, p. 135.

[Nem88] R. J. Nemanich, J. T. Glass, G. Lucovsky, R. E. Shroder, J. Vac. Sci. Technol. *A* **6** (1988), 1783.

[Pic02] C. Piccirillo, G. Davies, A. Mainwood, C.M. Penchina. Diam. Relat. Mater. **11** (2002), 338.

[Ram30] C. Ramaswamy, Indian J. Phys. **5** (1930), 97.

[Ree95] J. Reece Roth, *Industrial Plasma Engineering, Vol. 1:Principles* IOP Publishing, Bristol, (1995).

[Rem07] Z. Remes , M. Nesladek , P. Bergonzo, J. Barjon, F. Jomard, Phys. Stat. Sol. (a) **204** (9) (2007), 2950-2956.

[Sch98] D.K Schroder, Semiconductor Material and Device Characterisation (Second Edition), John Wiley and Sons, New York, 1998.

[Shi99] T. Shibata, T. Nakatsuji, K. Unno, E. Makino, in Proceedings of SPIE. Vol. 3891. Electronics and Structures for MEMS, edited by N. W. Bergmann, O.Reinhold, and N. C. Tien, SPIE, Gold Coast, Australia, 1999, pp. 336-343.

[Sol70] S. A. Solin, K. Ramdas, Phys. Rev. *B* **1** (1970),1687.

[Van02] M. Vanecek, A. Poruba, Appl. Phys. Lett. **80(5**) (2002), 719.

[Wil95] C. Wild, M. Funer, P. Koidl, Surf. Coat. Technol., **74(5)** (1995), 221.

[You86] R.A. Young, R.V. Kalin, Microelectronic Processing: Inorganic Material Characterization, American Chemical Society, Symposium Series 295, Washington DC, 1986, 49-74.

[Zhu89] W. Zhu, C. A. Randall, A. R. Badzian, R. Messier, J. Vac. Sci. Technol. A **7** (1989), 2315.

Chapter 3 Optimization of process conditions for thick SCCVD diamond growth

3.1. Introduction to the problematics

This chapter gathers the main experimental results reached in this thesis on the free standing single crystal CVD diamond growth. By mapping carefully the growth parameter domain and understanding how experimental parameters influence the physics of the growth it is tried to influence and control the main physical characteristics of the diamond layers. It is also important to note that the growth parameters are mutually related. For example, when the microwave power is changed, the substrate temperature is modified via complex plasma chemistry including atomic hydrogen recombination on the growing diamond substrate. The macroscopic experimental parameters thus govern the hydrocarbon add-addition mechanism and the surface growth mode on the atomic scale. By monitoring these processes with surface sensitive methods the macroscopic plasma parameters are assessed in order to relate to the properties of the epitaxial layers. Thus, experimental variables including the reactant gas pressure and concentration, substrate temperature, and sample stage are varied and monitored systematically in order to optimize the diamond layer quality and to control the (100) growth rate. Throughout this thesis only the growth on (100) substrate planes is investigated as this is the most important surface for obtaining high quality CVD diamond epilayers. This growth surface has specific growth mechanism as compared to (111) or (110) planes.

3.2. Homoepitaxial diamond growth: state of the art

An important effort has been devoted to establish highly reproducible deposition processes allowing the precise synthesis of diamond crystals. During the last 15 years, breakthrough results have been reported from several research groups through advanced studies mainly in Japan, the US, and Europe on homoepitaxial diamond growth. Natural or HPHT synthesized single crystals, which contain nitrogen or boron as impurities, are available as substrate diamond. Mirror-polished HPHT type-Ib single crystals have excellent structural properties and they are commercially available at a reasonable price and have therefore been widely used for homoepitaxial growth. Using these Ib-type samples as substrates for homoepitaxial growth in an ultra-pure gas phase allowed growing single crystal CVD layers with similar high structural quality but free of the contaminations present in the substrate. Crystal orientations that are commonly examined for homoepitaxial studies are (100), (111), and (110) faces. Intensive studies have shown that (100) diamond films crystalline quality is the best among films grown on fundamental crystal planes of the available substrates.

The optimization of the deposition process and understanding of the growth mechanism leading to very high-quality diamond samples is not complete yet. For the MPCVD process, one of the most important issues is to increase the diamond growth rate while maintaining high crystalline quality. Besides contaminations due to foreign elements, structural defects represent the most challenging problem for the homoepitaxial growth. Japanese researchers [Wat99, Tak00, Oku01] succeeded in depositing atomically flat homoepitaxial diamond using a very low methane concentration (approx. 0.05%) in the deposition gas mixture; however, the growth rates were too low (< 0.1 μm/h) for the technological exploitation of the material as the finally obtained film thickness is typically a few micrometers. In the last five years, several research groups have launched studies on the growth of thick (greater than 100 micrometer) homoepitaxial diamond (100) films at high growth rates of 1-20 μm/h by employing higher microwave power densities and by applying special growth conditions that are much different from conventional ones.

To enhance the growth rate, different routes have been proposed. Teraji *et al.* [Ter02, Ter05] using a CVD process at high microwave power (approx. 3.8–4.2 kW), succeeded in depositing flat homoepitaxial samples at higher methane concentrations (approx. 4%) and relatively higher growth rate (approx. 2.5 μm/h). Great advances in the deposition of high-quality homoepitaxial diamond have been made by Tallaire *et al.* [Tal04, Tal05a, Tal05b]. In particular, these authors used both pulsed microwaves (3.2 kW) and etching of the diamond substrate with a O_2/H_2 plasma before the deposition [Tal04, Tal05a]. They demonstrated that, with a process involving high continuous wave microwave with power densities and high pressures, and by adding very low amounts of nitrogen (2 to 10 ppm) the growth rates of single crystal CVD diamond can be increased from 6 to 16 μm/h while preserving very low defect concentrations of only 55 ppb for N_s in a sample doped with 10 ppm of nitrogen in the gas phase. Their pulsed wave process allowed the deposition of high quality, impurity-free samples at a high growth rate of approximately 22 μm/h. Finally, to suppress the formation of unepitaxial crystallites, Bauer *et al.* [Bau05] grew homoepitaxial diamond onto slightly off-axis substrates at 1400 W microwave power and 10%

CH_4 in H_2. The issue of high growth rate has also been addressed by several other groups [Yan02, Cha04], which used nitrogen to achieve growth rates above 100 µm/h.

However till now, to the best of our knowledge nobody has published reports on obtaining high electronic quality grade freestanding > 100 micron thick single crystal diamond wafers except Element Six results, where TOF measurement would give high mobility values, which is demonstrated that it is achieved in this thesis. Therefore effects of each process parameter on the growth mode will be intensively discussed in the following paragraphs.

3.3. Standard procedures for substrate and film characterization

Throughout this work standardized procedures are used for substrate manipulation and control of the all necessary characteristics based on a set of characterization methods, explained in Chapter 2.

1. Surface morphology of substrates and layers grown is routinely characterized using a differential interference-contrast (DICM) optical microscope (OM), DICM optical microscopy was applied for macroscopic characterization of surface morphology because it clearly reveals the morphological features of homoepitaxial diamond films. This gives us a three dimensional appearance of the sample features with improved contrast that is not unlike the appearance of a specimen in a scanning electron microscope. This method enhances depth of focus so that thicker features can be observed at higher magnifications.

2. Scanning electron microscope (SEM) in electron backscatter diffraction mode (EBSD) is used for the characterization the layer orientation and other local growth defects respectively. On the other hand the SEM is rather insensitive to the surface morphological features of homoepitaxial films such as round hillocks or bunching steps which cannot be easily monitored.

3. Micro-Raman Spectroscopy was utilized first to assess the crystallinity of the deposited layers as well as in order to analyze the possible influence of HPHT diamond substrate defects in the Raman spectra. Then the presence of residual stress induced in the samples as a consequence of the prolonged growth experiments was investigated applying Raman mapping.

4. Microscopic surface structures were characterized mainly by electron diffraction methods such as AFM and STM, providing real-space information of

atomic-scale surface structures. Scanning tunneling microscopy (STM) was used as a suitable method for investigating topography of surface atoms with atomic resolution, reflecting electronic states of surface atoms, although STM requires electrical conductivity [Tak00]. On the other hand, atomic force microscopy (AFM) is widely used because it yields information on the bunching step structure and surface roughness through comparably easy operations, in addition to the fact that AFM is applicable for insulators.

3.4. Effect of methane concentration

3.4.1. Introduction

In general, surface morphology of homoepitaxial diamond films varies microscopically and macroscopically depending on the methane concentration (C_{me}). The (100) substrates are preferred for high quality single crystal diamond growth due to the low defect density obtained, discussed in Chapter 1.

Several types of defects occur on the surface when increasing C_{me}. As discussed in Chapter 1, unepitaxial crystallites and growth hillocks are often observed on homoepitaxial diamond films as macroscopic anomalous growth. These anomalous features were already reported in the early stage of homoepitaxial growth study [Kam88]. Especially when the film is substantially thick, the film surface tends to be covered with these anomalous-growth regions [Tsu94, Bau05, Ham05]. Growth hillocks might grow faster than other homoepitaxial regions and bunching steps are formed beside the growth hillocks. Although the formation mechanism of the growth hillocks remains unclear, some hillocks have defective regions with unepitaxial crystallites in their center [Tsu94, Bau05].

Another defect in epitaxial layer is secondary nucleated crystals. Two kinds of nucleation modes are reported for unepitaxial crystallites. One is nucleation on the substrate surface and the other is nucleation in the homoepitaxial film [Tak99]. When the former mode dominates the anomalous nucleation, the unepitaxial crystallites should have almost the same size. The number density of the unepitaxial crystallites is likely to be higher in the sample edge region than in its center [Tsu94], but their average number density depends on C_{me} and substrate temperature (T_S).

Interesting growth modes also appear when C_{me} is less than 0.15%. In this case the diamond surface morphology resembles that of the case where diamond is exposed to the hydrogen plasma, which means that diamond growth under such low C_{me} obeys etching by atomic hydrogen [Ri06]. Under the extremely low C_{me} of 0.025%, unepitaxial crystallites are suppressed to nucleate; consequently, atomically flat surfaces are formed throughout the crystal plane of the substrate [Wat99, Wat00]. But because of the very slow growth rate of ca. 20 nm h^{-1}, this growth condition cannot be applied for practical purposes of homoepitaxial film deposition. In the higher C_{me} range of 6–10%, a macroscopically flat surface sometimes appears [Tsu96, Lee95, Shi90, Kiy97]. The surface is, however, microscopically rough because of substantial two dimensional nucleation growths on terraces [Tsu96]; the electrical properties of boron-doped diamond films grown under these conditions are worse [Kiy97], which might be attributable to dominant two-dimensional nucleation growth on terraces. Those worse properties imply that the macroscopic flatness of homoepitaxial films is not always a good indicator of film quality.

As the growth is reportedly pursued by the step flow mechanism, depending on the miss orientation angle of the substrate surface with respect to the (100) crystallographic plane, the substrate surface quality is also very important. For instance polishing lines – for example oriented in the <110> direction – can introduce barriers for the step flow leading to step bunching. At the same time dislocations or impurities at the surface can act as a source of new atomic steps during the growth enhancing the step bunching even more.

3.4.2. Experimental

In order to investigate the diamond growth mechanism on the (100) surface and find an appropriate growth domain with the α-parameter close to 3 favoring (100) surfaces C_{me} in the gas mixture was systematically varied (from 1% to 16%) while keeping other growth parameters the same.

The series of diamond films has been deposited in the MW PECVD reactor, described in Chapter 2 using commercially available HPHT, 1×1 mm^2 type Ib (100) diamond substrates. The misorientation angle with respect to the (100) plane of these substrates was varied from lower than 1.5° to about 8°. Prior to growth, all diamond substrates were chemically oxidized using an acidic solution of $H_2SO_4 + KNO_3$ (300 °C, 30 min) to remove surface contaminants, followed by rinsing in ultra-pure water.

Sample N°	CH_4/H_2, %	Pressure, Torr	Power, W	Temperature, °C	Growth time, h
190804euos	1	180	700	720	24
260804euos	2	180	720	700	24
270804euos	4	180	700	730	40
300804euos	6	180	630	730	24
170904euos	8	180	650	720	24
180904euos	10	180	650	700	21

Table 3.1: *Growth conditions of a series of samples grown at different* C_{me} *in the gas phase.*

The gases used for the CVD growth were 6N (99.9999%) hydrogen and 4N (99.99%) methane. Deposition conditions for the homoepitaxial growth for the C_{me} series were as described in Table 3.1. The total gas flow was maintained at 500 sccm. The deposition time was held around 24 h in order to obtain a useful thickness of a few tens of µm, which allows discussing the surface morphology. The temperature of the substrate was monitored using an optical pyrometer. After growth, the surface morphology of the deposited films was studied by means of optical microscopy, scanning electron microscopy (SEM) and atomic force microscopy (AFM). This was done in order to determine the effect of different methane concentrations on the surface quality.

3.4.3. Results and discussion

The surface morphologies of the different methane concentration series of (100) homoepitaxial diamond films are shown in Fig. 3.1 and 3.2. It was found that there were two major types of surface morphologies appearing. For a methane concentration in the range of 1 - 5% samples attained a typical crater-type surface morphology as a consequence of simultaneous growth of (100) and (111) growth planes in competition in a view of non optimal α-parameter. A closer examination of the samples surface structures by AFM as depicted in the Fig. 3.1(3) reveals that growth pits appear composed mainly of side (111) facets, which allows to point to a non-optimized α-parameter at this methane fraction range, favoring rather (111) facet growth.

A further increase in C_{me} from 5 to 10% has a visible influence on the suppression of (111) growth planes in competition with (100) planes and leading to the preferential growth of <100> facets. The surface morphology of CVD diamond films grown with C_{me} above 5% differs notably as shown in Fig. 3.2. These epitaxial layers consist of substantially flat extended regions as shown on the SEM and OM images of a low magnification in Fig. 3.2(1).

The SEM and OM images of a higher magnification Fig. 3.2 (2) show a detailed view of observed defects. A number of unepitaxial crystallites and cracks were the dominant defect structures observed at the higher C_{me} regime, which is consistent with other studies in the literature [Jan90]. It is believed that the formation of unepitaxial crystallites is attributed to the secondary nucleation on the surface in the initial stage of the crystal growth. The presence of the cracks is most likely due to growth induced defects which propagated over the substrate edges and the lateral layer growth which has been restrained by the holder edges.

In order to characterize the surface morphology of the samples in detail, AFM images for all the samples were obtained. Fig. 3.1(3) and 3.2(3) show a top-view AFM images of the surface topography of the homoepitaxial diamond films. Despite the macrosopcic defect present, the typical average surface roughness R_{rms} of diamond films grown with thickness of a few tens of microns using C_{me} less than 5% is in the order of 100 - 300 nm on a scanned area of $5 \times 5\ \mu m^2$.

However for higher $C_{me} > 5\%$, the situation is different. Fig. 3.2(3) shows the results of growth runs using a C_{me} higher than 5% and leading to an average surface roughness R_{rms} for the typical flat regions of about 4–6 nm on a scanned area of $5 \times 5\ \mu m^2$. This unique result indicates that when increasing the methane concentration to values higher than 5% the α-parameter is coming close to 3 which favors the (100) growth mechanism and low defect density. However, some number of growth defects, induced by a secondary nucleation on the surface of the films shown in Fig. 3.2 remains leading to disturbances of an ideal step flow.

Fig. 3.3 represents the growth rate of deposited diamond films as a function of C_{me}, while the total gas flow rate was maintained at 500 sccm. The saturation behavior of the growth rate is observed with an increase of C_{me}. A possible mechanism of this saturation phenomenon occurring for low-power MW PECVD

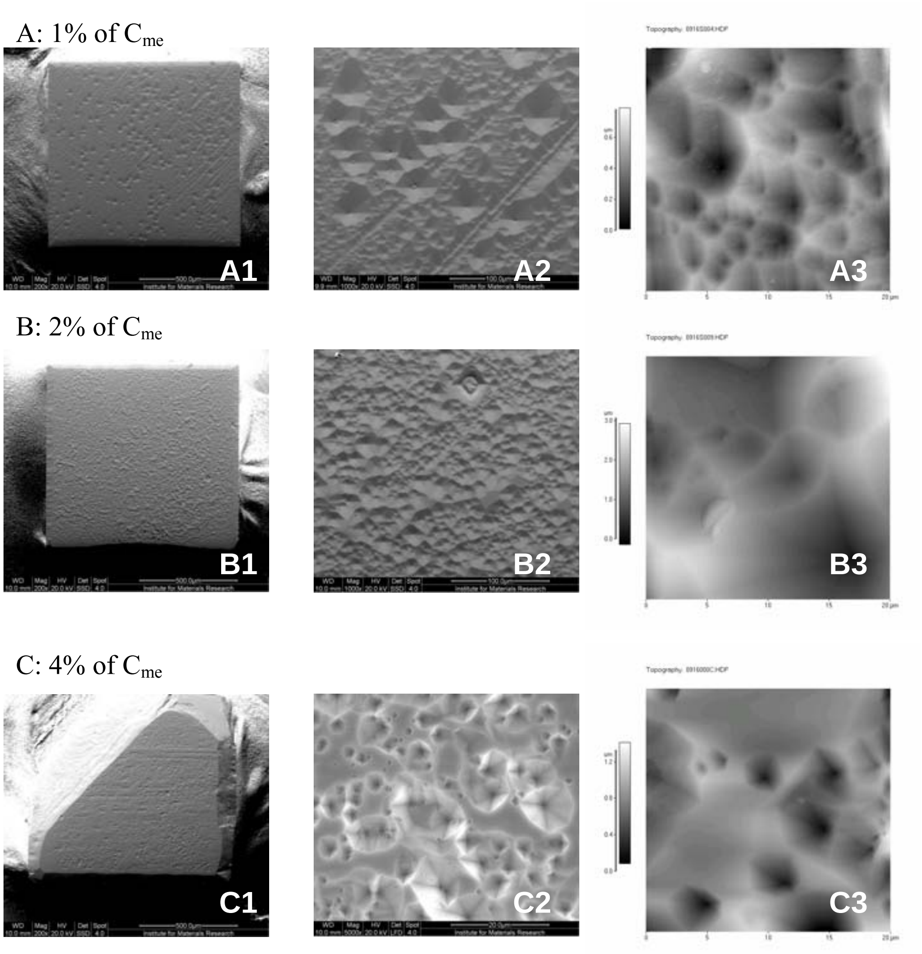

Figure 3.1 : *Comparison of the surface morphology of the samples grown at 1, 2, 4 % of* C_{me} *(A1, A2, A3 – 1%; B1, B2, B3 – 2%; C1, C2, C3 – 4% respectively), where (1): SEM images of the samples (x200); (2): SEM images of the samples (x1000); (3): AFM images of the samples.*

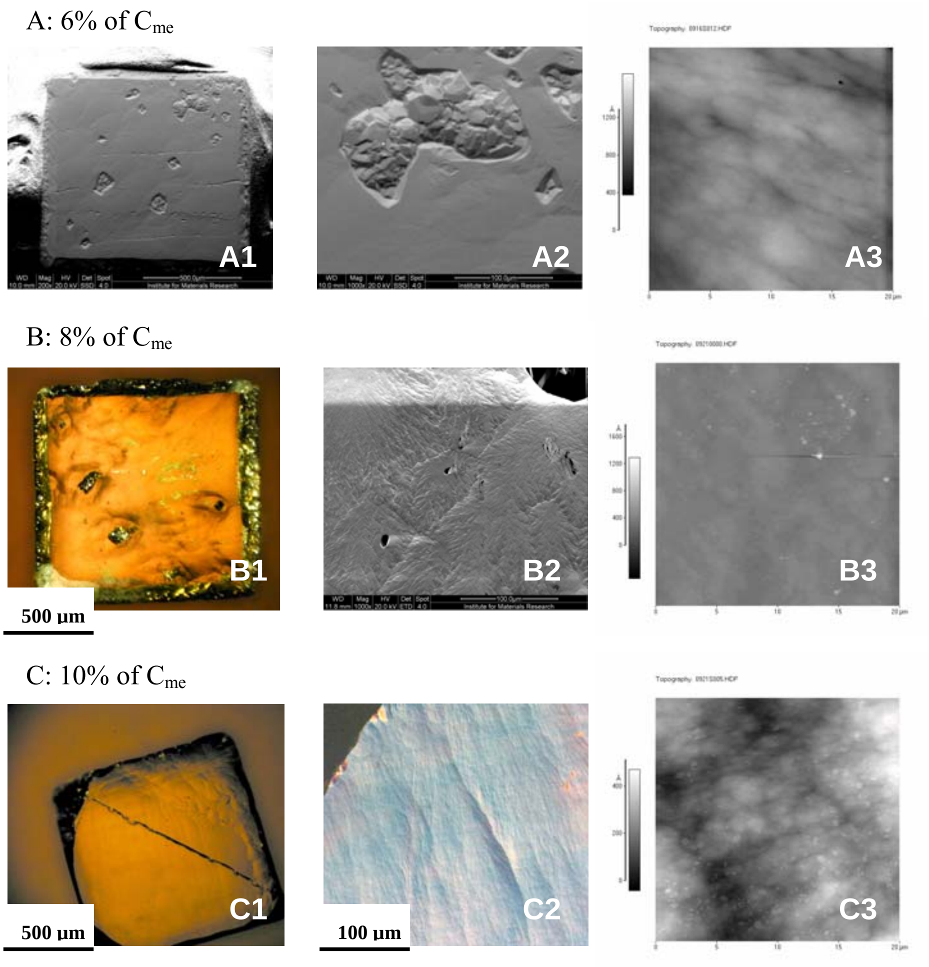

Figure 3.2: *Comparison of the surface morphology of the samples grown at 6, 8, 10 % of C_{me} (A1, A2, A3 – 6%; B1, B2, B3 – 8%; C1, C2, C3 – 10% respectively), where (1): SEM or DICM images of the whole samples; (2): SEM or DICM images of the samples of higher magnification; (3): AFM images of the samples.*

at such high C_{me} might be: (i) insufficient creation of both atomic hydrogen and effective carbon precursors attributable to low microwave power density; (ii) covering of the top surface with methyl group or non-diamond phases attributable to the low reaction rate, which leads to decreased nucleation-site density.

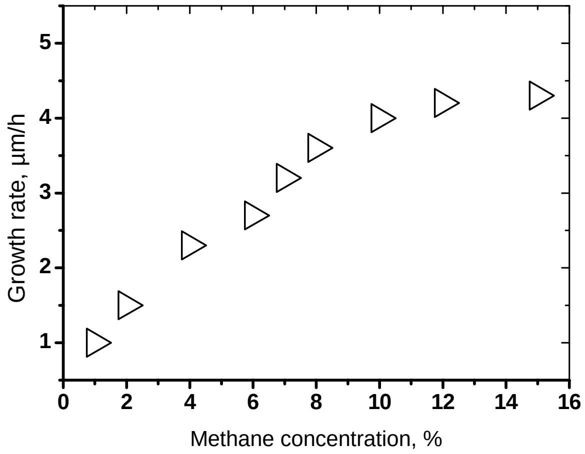

Figure 3.3: *Growth rate of deposited diamond films as a function of CH_4 concentration in H_2, maintaining a total gas flow rate of 500 sccm.*

Clearly, methane addition directly influences the deposition rate. The quality of the film also depends on the relative quantity of hydrocarbon added.

The foregoing obtained results lead to the conclusion that under the given circumstances the best results are obtained at C_{me} between 6 - 16% in terms of quality and growth rate. In the following the work has been concentrated on homoepitaxial growth with these particular process parameters in order to reduce the secondary nucleation and to prepare surfaces with low defect density, free of scratches and polishing lines on the surface. As will be shown in the next section, we have tried to pre-treat the substrate surface using an O_2/H_2 plasma.

3.5. Effect of pretreatment and substrate quality

3.5.1. Introduction

Crystalline defects on the substrate surface and in the subsurface region have an unfavorable effect on the quality of homoepitaxial diamond films. Fig.3.4. shows an example of as-received substrates from different batches: an ideally polished substrate and a substrate with some of the typical polishing faults randomly spreading throughout the whole substrate surface. Additional substrate defective morphology optical images are presented further in this section and will be shown discussed in the Raman mapping section.

In this context, defects primarily means dislocations, other crystal defects and microcracks, but also includes twin boundaries, point defects, low angle boundaries and any other disruptions to the crystal lattice. Once present these dislocation structures cannot simply terminate in the layer but generally multiply and expand, causing dislocations and associated defects in the overgrown CVD layer, resulting in stress, defects and cracks as the layer is grown thicker.

Two types of defects can be revealed: 1) those intrinsic to the substrate material quality. In selected natural diamond the density of these defects can be as low as 50 mm^{-2} while in HPHT Ib substrate material it can be 10^7 mm^{-2} or greater if not properly selected [Wil05]. 2) Those resulting from polishing, including dislocation structures and microcracks in the form of `chatter tracks` along polishing lines. The density of these can vary considerably over a sample, with typical values ranging from about 10^2 mm^{-2}, up to more than 10^4 mm^{-2} in poorly polished regions or samples.

Substrate quality varies dramatically and may consist of a few differently accomplished parts which detrimentally reflect in the structural quality and homogenity of the grown film. These polishing defects introduce additional dislocations. When a homoepitaxial film is deposited on the substrate with dislocations that propagate in the CVD diamond during the growth, the band A emission appears, which evidences dislocations, clearly apparent in CL images [Ter06]. The dislocations terminating at the surface can also be an additional source of the secondary nucleation leading to the growth of unepitaxail crystallites. Such embedding of unepitaxial crystallites in the homoepitaxial film has been reported, producing also a spreading pattern of the band A emission [Tak03]. Because such defects must be removed for electronic device applications investigation of the dislocation distribution in the film and elucidating the effects of substrate defects on the dislocation formation in the film are important research subjects.

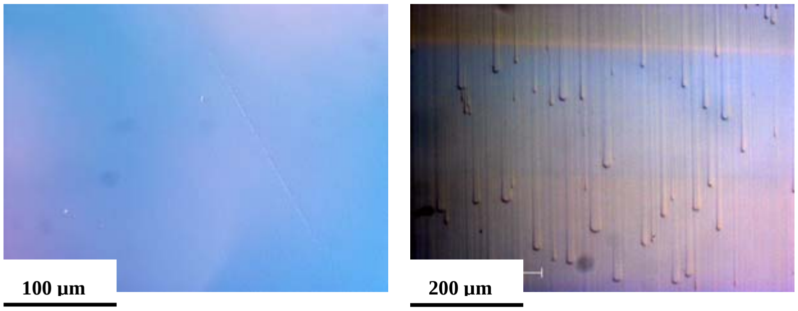

Figure 3.4: *DICM images of the as-received substrates: a) nearly ideally-polished substrate surface; b) substrate with polishing faults.*

One of the ways of removing the defects induced at the substrate surface are additional pretreatment carried out before the growth. The main idea behind treatment used in this work is that by anisotropic etching, (e.g. etching parameter α, defined by the similar way as the growth parameter α with the difference that the growth rate is now negative), we can find such conditions that (100) surface planes will dominate the surface morphology after etching, e.g. all non (100) micro-planes or polishing defects are removed rapidly.

The basic pretreatment before the growth is a chemical etching of diamond surface to remove non diamond carbon residual and spurious metal traces coming from polishing. In some cases the chemical etching has a positive effect on the suppression of etch-pits and growth hillock formation [Wan00]. This cleaning procedure is implemented as follows: diamond substrates are chemically oxidized using an acidic solution of $H_2SO_4 + KNO_3$ (300 °C, 30 min) to remove surface contaminants, followed by rinsing in ultra-pure water. This chemical etching procedure has, however, no function to remove the polishing-induced defects. These results indicate that suitable combination of pretreatments toward the mirror-polished substrate is required to obtain high quality diamond growth.

One specific method of minimizing the surface damage of the substrate, is to include an in situ plasma etch on the surface on which the homoepitaxial diamond growth is to occur. In principle this etch needs not be in situ, nor immediately prior to the growth process, but the greatest benefit is achieved if it is in situ, because it avoids any risk of further physical damage or chemical contamination of the substrate. Oxygen and hydrogen plasma are alternative methods to for example, those utilizing halogens, other inert gases or nitrogen can be applied to diamond to etch the surface damaged layer to remove the polishing lines and to produce suitable surfaces for subsequent CVD diamond epilayer growth. Typically, the etch consists of oxygen or/and hydrogen etch and then moving directly into synthesis by the introduction of the carbon source gas. Microwave plasma, quasi-ECR microwave plasma and RF plasma are some of the methods that can be utilized for this purpose. The etching rate is typically 1-10 $\mu m \cdot h^{-1}$ under optimized etching conditions; the etched depth of diamond is ca. 1 µm in most cases [Yam05]. The surface becomes rough with pits in the case of etching using microwave plasma [Wan00, Yam05]. As the etch is aggressive, it is particularly important for this stage that the chamber design and material selection for its components be such that no chamber material is transferred by the plasma into the gas phase or to the substrate surface.

3.5.2. Experimental

In order to reduce the secondary nucleation and to prepare surfaces with low defect density, free of scratches and polishing lines on the surface it was tried to pre-treat the substrate surface using an O_2/H_2 plasma at conditions described in Table 3.2.

Pre-treatment conditions		Growth conditions	
Pressure	70 Torr	Pressure	180 Torr
Power	900 W	Power	600 W
Temperature	800 °C	Temperature	750 - 1200 °C
Gas flow	500 sccm	Gas flow	500 sccm
O_2/H_2	4 %	CH_4/H_2	6 %

Table 3.2: *Plasma pretreatment and growth conditions.*

Plasma etching of the samples was performed for different etching times ranging from 5 min to 90 min inside the same MW PECVD reactor chamber used for growth and working with typical mixtures of 1–5% O_2 in H_2 gas. The temperature of the sample during the etching was varied in the range between 700–900 °C to obtain an optimal surface for the film growth. Afterwards the pretreated samples were observed by an optical microscope and AFM. An assessment of the diamond quality was made by a standard confocal Raman spectrometer at room temperature using the 514.5 nm line of an Ar-laser.

3.5.3. *Results and discussion*

3.5.3.1. Surface morphologies of HPHT substrates before and after plasma pre-treatment

Fig. 3.5 (a) shows AFM top-view image (10×10μm^2) of a typical surface from the flat regions in between the polishing faults as shown in DICM image in Fig. 3.5(b) of as-received mechanically polished diamond substrates. The pattern produced by mechanical polishing typically runs parallel to one direction for the surface of as-received good quality diamond substrates. The typical surface morphology of the well accomplished areas on the polished substrates consists of large (about 200 nm) and small (about 20 nm) periodic patterns, and the height range of the large periodic pattern is about 4 nm. All of the values of R_{rms} determined by AFM images of the as-received diamond substrates were not more than 3 nm.

As discussed, in order to reduce the defect density and impurities present at the surface of substrates we have used an O_2/H_2 plasma pre-treatment to prepare a surface with a lower roughness. We have used two configurations of the substrate holders, 'open' and 'enclosed' type (see Chapter 2).

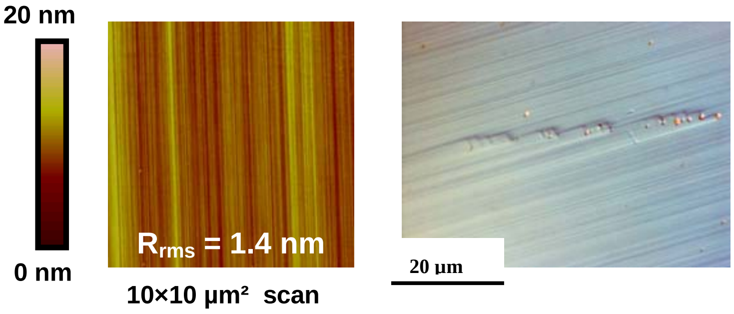

Figure 3.5: *AFM and DICM image of the typical as-received substrate.*

For the closed type of the holder, discussed in the Chapter 2 and using a ratio of 4% O_2 in H_2 we increased the etching time from 5 min to 90 min. The surface morphology change for etching times between 5 and 60 min is shown in Fig. 3.6, leading to a clean surface covered with step lie features over the entire surface for 40 min etching time (see Fig. 3.6 (c)). In this case, R_{rms} did not change so much between before and after etching.

For 60 min etching time a surface consisting of a large number of square-shaped etch pits with fourfold symmetry (see Fig. 3.6 (d)) appears. This figure also shows that a well developed etch pit has side facets composed of steps. The steps developed along the <110> direction, which indicate that the (100) diamond surface is etched by migration of steps along <110>. The etch pits probably initiated at polishing grooves and lattice defects such as dislocations in the substrate or impurities at the surface, originating the step flows in case of etching, i.e. they can act as a source of steps influencing the deposition or etching rate over the entire surface [Lee95]. Thus the developed anisotropic etching procedure leads to preparation of surface optimized for the homoepitaxail growth.

Dimensions of the pits are increased with the etching time. For a 90 min etching time, shallow polishing lines flattened although more deep polishing grooves did not disappear. This fact indicates that etching of surface defects by in situ O_2/H_2 plasma etch is insufficient to remove polishing grooves of a large depth on the original substrate surface.

Moreover, many etch pits appeared on the surface of the diamond substrate, as shown in Fig. 3.7 (c). However, dimensions of the etch pits increased. The etch pits had mainly a fourfold symmetry, the depth of which ranged from 100 to 200 nm and lateral dimensions from 0.5 to 2 nm, respectively.

A similar effect has been observed using an ‘open’ configuration of the holder (see Fig. 2.4 (c)), which modified the plasma sheet close to the substrate surface. Fig. 3.7(a, b) shows AFM top-view height and amplitude images of the substrate surface pretreated for 60 min using an ’open’ type of holder, where the amplitude image is given to show the enhanced contrast of a hollow etch pattern and spreading of differently shaped etch features. The etch pits and holes covered the whole substrate surface, the depth of which ranged from 100 to 250 nm and lateral dimensions from 5 to 10 nm, increasingly roughening the substrate surface. The R_{rms} value in this case was about 32 nm.

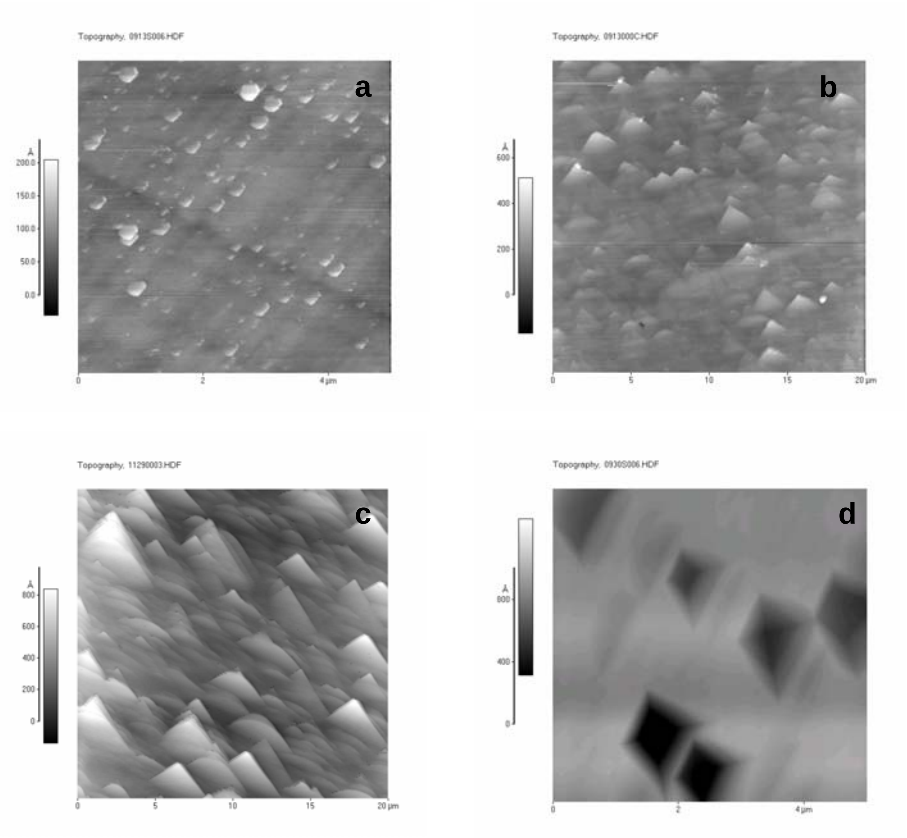

Figure 3.6: *AFM topography of the substrates etched in 4% O_2/H_2 plasma at approximately 800 °C for a) 5 min; b) 20 min; c) 40 min; d) 60 min.*

Therefore the etch time/temperature has been selected to enable any remaining surface damage from processing to be removed, and for any surface contaminants to be removed, but without forming a highly roughened surface and without etching extensively along extended defects (such as dislocations) which intersect the surface and can cause deep pits (see Fig. 3.7(a)).

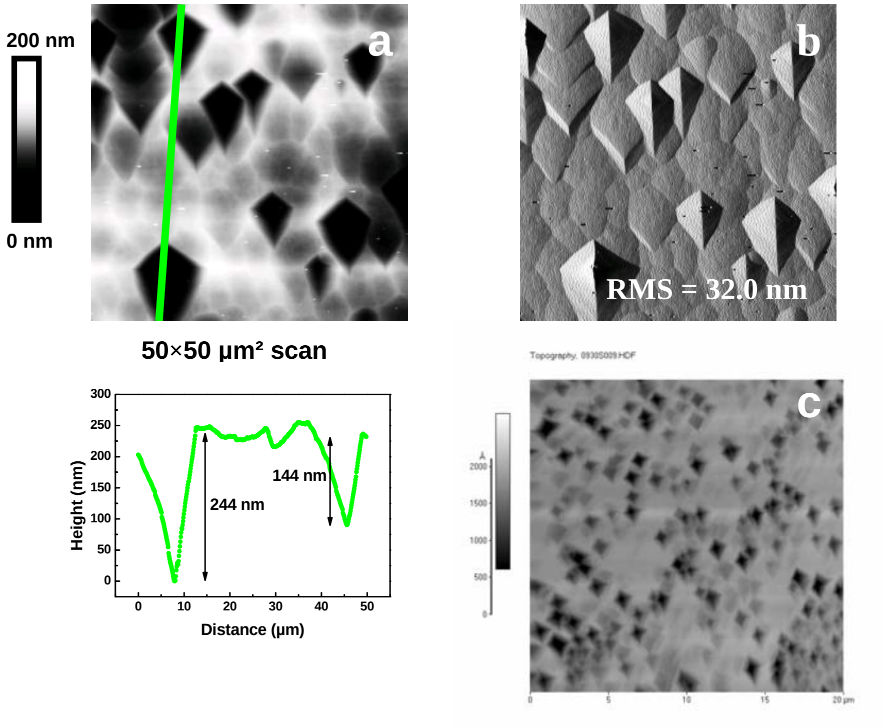

Figure 3.7: *Comparison of AFM images of two substrates pretreated using (a, b) open holder; (c) enclosed holder, but otherwise similar conditions. Also the height profiles can be seen for image (a).*

3.5.3.2. Surface morphologies of films grown with plasma pretreatment

After the plasma pre-treatment step of the substrates, homoepitaxial diamond growth was performed using 6 – 15 % C_{me} together with the standard growth conditions mentioned in Table 3.2.

Figure 3.8 (a, b) shows optical DICM images of the surface morphology of a 90 minute plasma pre-treated substrate surface and the corresponding homoepitaxial diamond film grown on it for 24 hours at 6% C_{me}. The DICM image of the pretreated substrate corresponds to the AFM image discussed in the previous section in Fig. 3.7(c). As it is seen on the optical image the polishing lines are flattened and a number of etch pits appeared on the substrate surface as a result of etching. One could not observe any secondary nucleation on the whole surface of the film. The surface consisted of smooth regions with round shaped features with lateral sizes < 30 µm. The film surface inherited some deep polishing lines which have not been flattened by the etching treatment. The growth rate of this film was calculated to be about 2.3 µm/h.

Figure 3.8(c, d) shows optical DICM images of the surface morphology of a 60 minute plasma pre-treated substrate surface using an 'open' holder and the corresponding homoepitaxial diamond film grown on it for 7 hours at 10% C_{me}. The DICM image of the pretreated substrate corresponds to the AFM image discussed in the previous section in Fig. 3.7(a, b). As it is seen on the optical image the substrate surface has a hollow rough pattern which consists of large etch pits densely covering the surface as a result of aggressive etching in a dense plasma sheet, created by an open type of holder. The subsequent growth of a film on such a surface inherits the substrate surface pattern. There is a correspondence between the etch holes on the substrate surface and round "bubble-like" features on the film surface which could be interrelated.

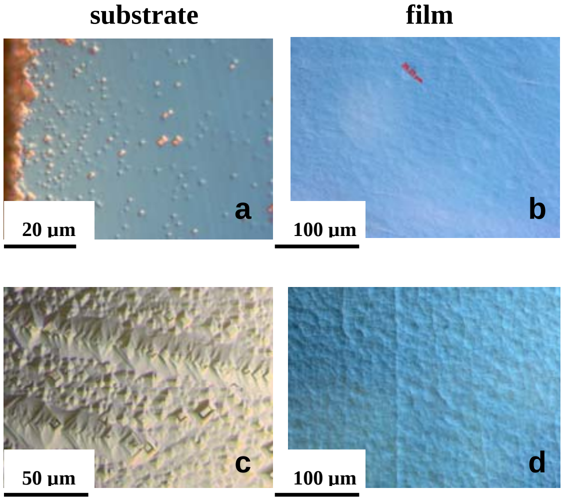

Figure 3.8: *Comparison of DICM images of two substrates pretreated and respective films grown at (a, b) open holder; (c, d) enclosed holder, but otherwise similar conditions.*

Fig. 3.9 shows an optical microscope image of the surface morphology of the homoepitaxial diamond film grown for 27 hours at 12% C_{me} on a 60 minute plasma pre-treated surface. The AFM morphology has been demonstrated in the previous section in Fig. 3.6(d). When pre-treated during 40 minutes, similar results are obtained. Non-epitaxial imperfections could not be observed: neither unepitaxial crystallites nor pyramidal hillocks have been found on the surface of the grown film. DICM optical image of the film surface shown in Fig.3.9 (b) demonstrates that there were no etch related round features. Only polishing deep grooves remained from the substrate surface. Figure 3.9(c) shows an AFM image of a near-atomically flat surface observed over the whole area of the deposited film. According to the AFM observation of a film grown at 12% C_{me}, the root mean square surface roughness (R_{rms}) on average is 0.8 nm for a $5 \times 5\mu m^2$ scanned area, whereas the thickness of the film is about 120 μm, which corresponds to a growth rate of about 4.5 μm/h. It must be noted that a term of 'a near-atomically flat surface' accepted in this thesis is defined for a surface with R_{rms}<< 1nm on average. This result was first in the literature that reported on achieving very low roughness CVD diamond films for important film thickness.

This result points to the conclusion that the optimal etching pretreatment configuration is when using an enclosed type of holder for 60 min etching time. When pretreated during 40 minutes, similar results are obtained. Non-epitaxial imperfections are could not be observed.

The film in Fig. 3.10 was grown for 1 hour at 10% C_{me}, thickness 4 μm, while Fig. 3.11 shows a film that was grown for 159 hours at a 10% C_{me}, thickness 630 μm. The growth rate was calculated to be approximately 4 μm/h. It is clear that the surface morphology does not change dramatically by growing for a longer period or increasing the methane content, which together with the effect of increased C_{me} itself will be discussed further in detail in Section 3.9. Almost no non-epitaxial imperfections could be observed in either image. These films were almost completely free of defects with neither unepitaxial crystallites nor pyramidal hillocks. SEM pictures (Fig. 3.11 (a, b)) show only a small number (< 2 mm^{-2}) of square-shaped inverted pits with fourfold symmetry and sizes < 50μm.

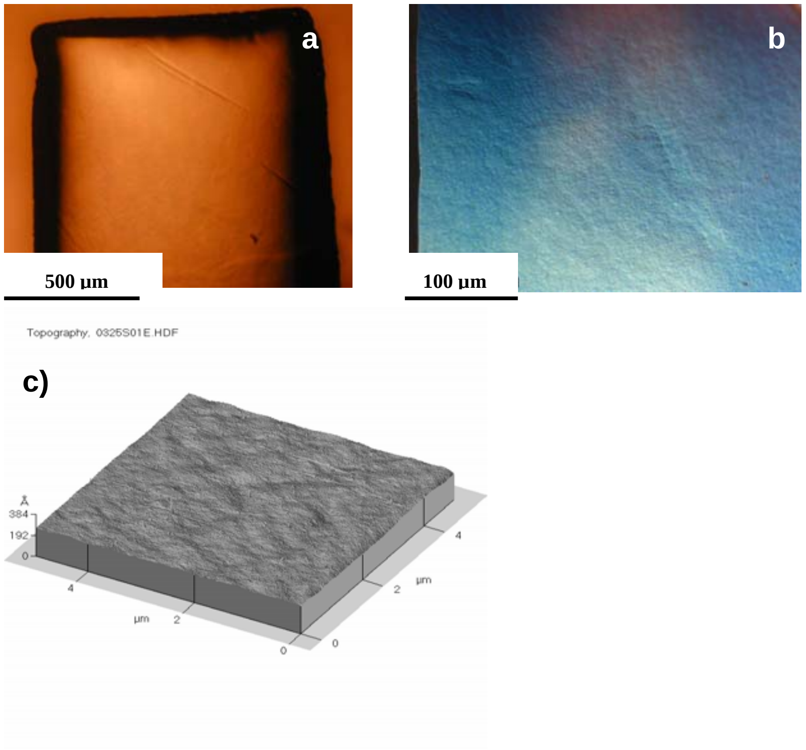

Figure 3.9: *DICM images (a, b) and AFM image (c) of a sample (1 × 1 mm^2) grown at 12% CH$_4$/H$_2$ ratio for 27 h on a 60 min 4% O$_2$/H$_2$ plasma pre-treated substrate with a thickness of 120 µm.*

The surface quality is usually known to decrease with an increased thickness [Mun95], which is not so dramatic in our example. The AFM measurements indicate that for the film grown for 161 hours (Fig.3.11(c)), the surface roughness (R_{rms}) on average is about 1.5 nm on a 5 × 5 µm^2 scanned surface size over the whole area of the sample whereas the thickness of the film is 630 µm.

Although the preparation of near-atomically flat CVD diamond epilayers has already been presented in the past fro submicron thick layers [Tsu94], the results presented in this thesis show for the first time near-atomic roughness for very thick single crystal CVD diamond layers. However, the presence of some individual defects has influence on the maximum (peak-to-peak) surface roughness, which is in the order of 50 nm on some individual spots. Growth on substrates of 1 × 1 mm^2, 2.5 × 2.5 mm^2 and Ø = 5 mm yielded the same quality (see Fig.3.9, 3.10, 3.11) over the entire surface and similar growth rates.

All of the monocrystalline diamond layers grown on the pre-treated for 40-90 min plasma substrates using an enclosed type of holder (see Fig. 2.4(b)) exhibit much lower roughness values as determined by AFM, between 0.5–1.5 nm for the same scanned area. Note that the substrate was not taken out of the reactor after the etching step further. The quality of the produced surface in terms of R_{rms} is an enhancement when compared to that of the smoothest areas of non-pre treated specimens of the C_{me} series grown at similar methane rich conditions discussed in the previous section. There the obtained R_{rms} was 4–6 nm as mentioned above.

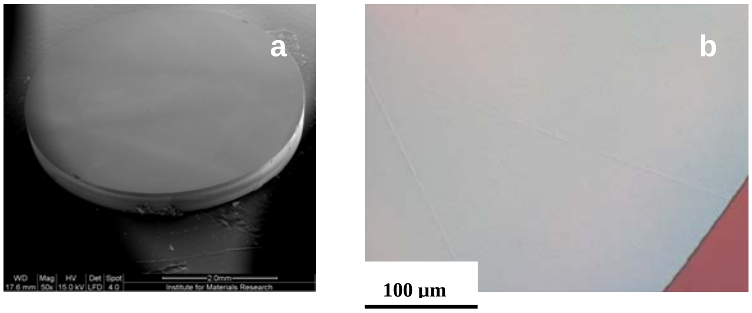

Figure 3.10: *SEM (a) and OM (b) images of a sample (Ø=5 mm) grown at 10%* CH_4/H_2 *ratio for 1 h on a 60 min 4%* O_2/H_2 *plasma pre-treated substrate.*

Fig. 3.12 shows the comparison of the DICM images of the non-pretreated substrates regions and the corresponding regions of the films grown onto them at methane rich conditions but otherwise similar conditions except the initial substrate structural quality. As shown on the DICM images (Fig. 3.12 (a, b) and (c, d)) the developed optimal etching pretreatment removes only the shallow polishing lines and scratches while not affecting the deep grooves on the substrate surface (also see Fig. 3.22(a, b) and 3.25 (a, b)). Therefore the deposited film inherits all the deep substrate polishing faults. The better the initial substrate structural quality the higher quality diamond film will be deposited on it as demonstrated in Fig.3.12 (e, f).

These experiments demonstrate that by the application of the precisely developed O_2/H_2 plasma etching procedure prior to the growth, not only the occurrence of

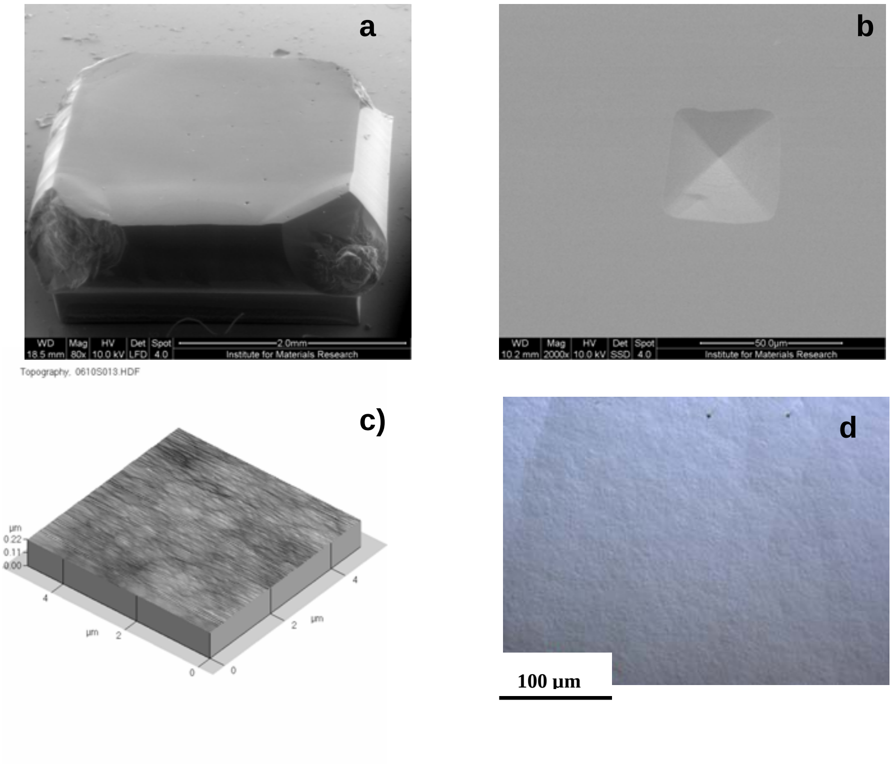

Figure 3.11: *SEM images (a) of a whole sample (2.5 × 2.5 mm^2) grown at 10% CH_4/H_2 ratio for 161 h on a 60 min 4% O_2/H_2 plasma pre-treated substrate and (b) an etch pit defect. DICM (c) and AFM topography (d) images of the sample surface.*

large elevations like cusps, sharp points and polishing defects on the homoepitaxial layers can be prevented or at least strongly reduced but also the surface roughness remains low. This can be explained by the fact that a number of highly active step sources like foreign particles are etched away relatively easily, thus the step bunching into macroscopic steps are reduced. This is on the basis that the substrate must be carefully selected before the deposition.

Fig. 3.13 shows a typical structure of the samples of this study and the stages of the growth process. At the beginning of the growth a high density of etch pits is present, generated by the O_2/H_2 etching pre-treatment.

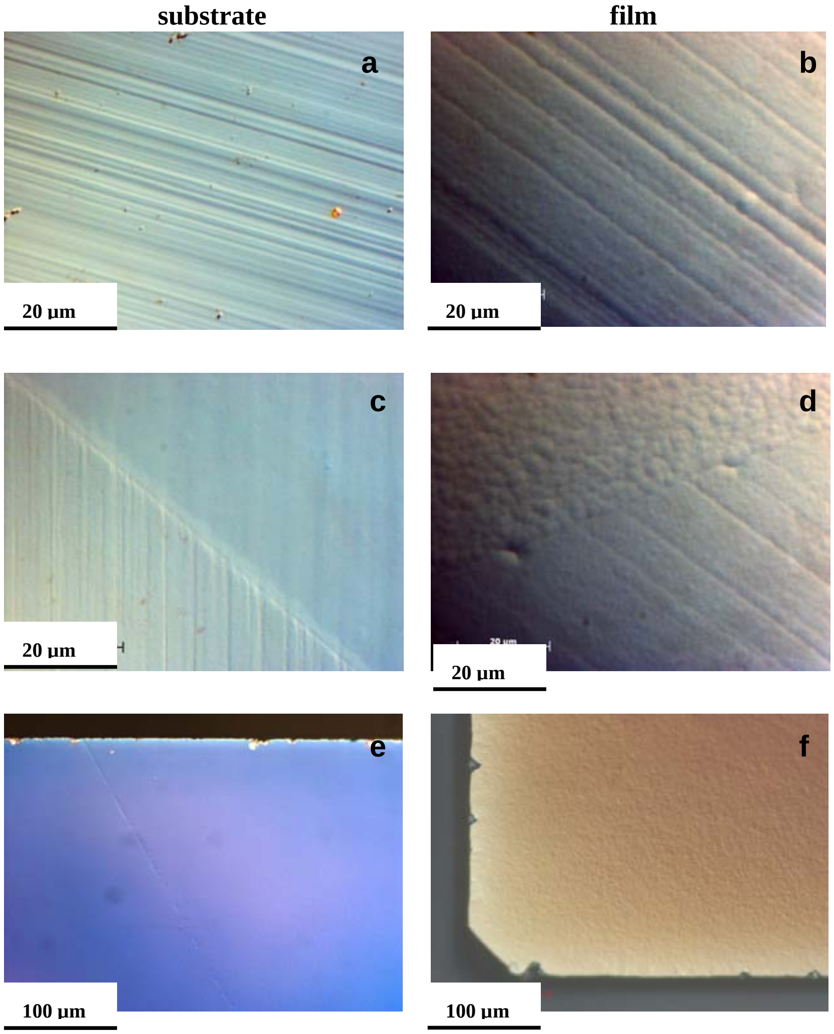

Figure 3.12: *DICM images. The images in the left column show the substrates morphologies (a, c, e); the images in the right column show the corresponding films grown onto the respective substrates (b, d, f).*

Then closing up of the etch pits is governed by the van der Drift selection and the well known α-parameter, followed by the atomic island growth mechanism. It is likely that the island growth is favored by the combination of an increased methane concentration with a low misorientation angle of the substrate and a relatively low growth temperature leading to single crystalline layers of high quality. The defect content and the crystallinity of such layers will be discussed later in Chapter 4.

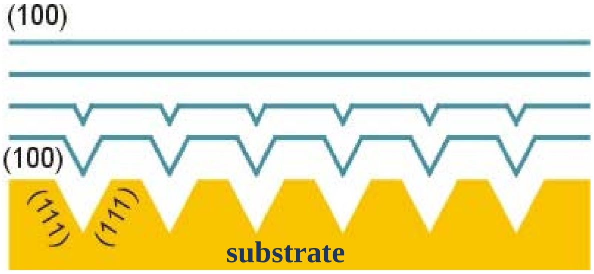

Figure 3.13: *Schematic description of the change of the surface during the growth process by van der Drift selection, based on the Vollmer-Weber type of growth.*

3.5.3.3. Raman characterization of films grown on pretreated substrates

Micro-Raman spectroscopy has been used to show how the high methane concentration and plasma pretreatment affects the film quality in terms of crystallinity and non-diamond content. Fig. 3.14 shows a confocal Raman spectrum obtained at the top face of a 250 µm thick homoepitaxial layer grown at 7% CH_4/H_2 revealing no other features than a very sharp diamond-related peak, i.e. the Raman peak, related to the sp^3-hybridised C at 1332.5 cm^{-1} is clearly present. Furthermore, there is no luminescence of N-vacancy complexes, which should appear at approximately 2100 cm^{-1} etc. This indicates that the homoepitaxial layers are of high quality, containing no non-diamond phases. As there is neither a shift of the position of the diamond peak we can also conclude that no internal stresses are present in the film. As shown in the inset of Fig. 3.14 obtained from higher resolution confocal Raman measurements, the full width at half maximum (FWHM) of the diamond-related peak of the CVD diamond layer was as low as 1.7 cm^{-1}, which was limited by the spectral resolution of the system. This value is equal to the lowest value for a perfect diamond crystal. The peak characteristics are independent of the position on the sample.

Almost all the films grown had the value of the FWHM was in the range of 1.5 – 2 cm^{-1}, indicating an overall higher quality and a lower level of stress in the CVD films. This means that the homoepitaxial layer exhibited extremely good crystalline quality, no presence of crystalline imperfections, thus a high degree of atomic ordering of the sp^3-hybridised carbon.

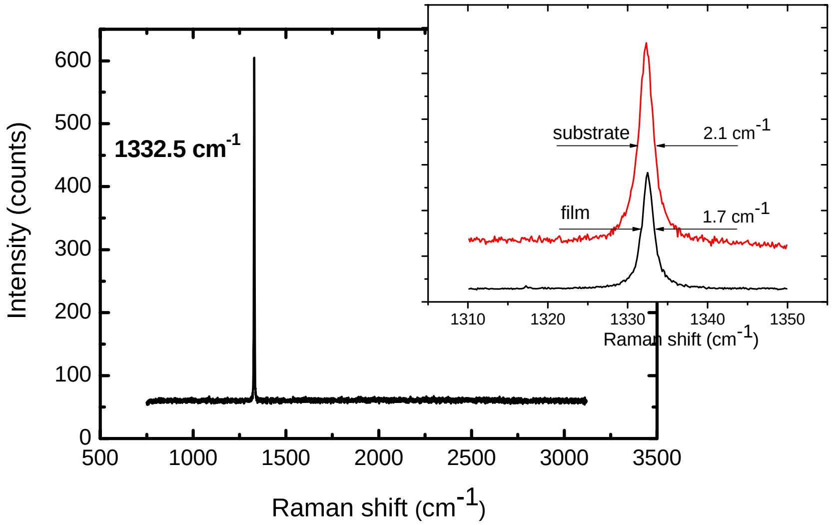

***Figure 3.14**: Typical Raman spectra of a homoepitaxial diamond layer. The FWHM was as low as 1.7 cm^{-1}. The inset compares the FWHM of the Raman lines of the HPHT substrate and the CVD film.*

3.6. Effect of temperature

3.6.1. Introduction

Similar to the methane concentration C_{me}, the substrate temperature T_S during diamond deposition is also an important parameter that determines the growth rate and crystalline quality of homoepitaxial diamond. Homoepitaxial diamond is typically grown in a T_S range of 600–1200 °C. Graphite is formed dominantly at T_S greater than 1200°C, but the growth rate is very small at T_S below 500 °C [Mat82, Kam83, Kam92]. These tendencies are theoretically reasonable [Fre91, Spe94].

Theoretically the growth rate of homoepitaxial films has activation energy, E_a, and is known to depend on T_S according to the Arrhenius relationship exp ($-E_a/RT_S$), with the gas constant R. The activation energies E_a reported by Chu *et al.* were 8 ± 3 $\mathrm{kcal \cdot mol^{-1}}$ for the (100) crystal plane, 18 ± 2 $\mathrm{kcal \cdot mol^{-1}}$ for the (110) crystal plane, and 12 ± 4 $\mathrm{kcal \cdot mol^{-1}}$ for the (111) crystal plane for T_S of 750–1000 °C [Chu92]. Maeda *et al.* obtained 7–15 $\mathrm{kcal \cdot mol^{-1}}$ for the (100) crystal plane and 20 $\mathrm{kcal \cdot mol^{-1}}$ for the (111) crystal plane [Mae95], whereas Sakaguchi *et al.* reported 8.5 $\mathrm{kcal \cdot mol^{-1}}$ for the (111) crystal plane [Sak99]. These values are not identical with each other. T_S depends dominantly on the plasma density at the sample, which is modified along with changes in the plasma conditions and leading to various radical densities at the substrate surface. The modification of plasma condition affects E_a, which might cause the spreading of E_a. External heating of the sample holder allows controlling T_S without changing the plasma condition. The RF heating of a graphite susceptor is usually used as an external heating, however this was not possible in the thesis work due to high plasma densities used, which need intensive cooling.

Other previous reports on E_a have mostly been carried out using a CVD apparatus without the external heating. Therefore the absolute values of the reported E_a must be examined well. E_a tends to be large for crystal orientations with a high growth rate. The average value of E_a for spontaneously nucleated diamond particles is calculated to be 14 $\mathrm{kcal \cdot mol^{-1}}$ [Kam92]. When the combustion flame method was applied for homoepitaxial diamond growth using acetylene as the source gas, E_a was as high as 12 $\mathrm{kcal \cdot mol^{-1}}$ for both the (100) and the (111) crystal planes and 18 $\mathrm{kcal \cdot mol^{-1}}$ for the (110) plane, even though both T_S of 1000–1400 °C and the plasma density were much higher than for the case of typical MW PECVD [Wei95], indicating that E_a depends strongly on the diamond's crystal orientation.

Because a diamond surface is covered with hydrogen during chemical vapor deposition, the surface terminating hydrogen must be first abstracted to form surface-excited sites; the second carbon radical adsorbs onto the surface-excited sites. Theoretical predictions of chemical reactions for diamond growth are described in detail by Spear et al. and Buttler *et al.* [Spe94, But01]. Under typical low-pressure diamond CVD conditions, each reaction equation can be described as follows (for details see Chapter 1):

		Rate constant	
Hydrogen abstraction:	$C_DH + H \rightarrow C_D^{\bullet} + H_2$,	(k_1)	(1)
Hydrogen adsorption:	$C_D^{\bullet} + H \rightarrow C_DH$,	(k_2)	(2)
Diamond growth:	$C_D^{\bullet} + C_xH_y \rightarrow C_D - C_xH_y$,	(k_3)	(3)
Graphite formation:	$HC_D\text{–}C_D^{\bullet} \rightarrow Cgr = Cgr + H$,	(k_4)	(4)

$$\chi\, C_D^{\bullet} = k_1\, [H] / (k_{-1}\, [H_2] + k_2\, [H] + k_3\, [C_xH_y] + k_4\,) \times \chi C_DH\ . \qquad (5)$$

Here, C_xH_y is a reaction precursor, C_D is carbon with a diamond structure, $C_D^{\bullet}$ is excited state of C_D, χC_DH is the number density of C_D–H sites, and $\chi\, C_D^{\bullet}$ is the number density of $C_D^{\bullet}$ sites. Therefore, the growth rate increases with increasing $\chi\, C_D^{\bullet}$. Under typical growth conditions, where methane is highly diluted and the reaction temperature is ca. 900 °C,

Eq. (7) is approximated as [Spe94]

$$\chi\, C_D^{\bullet} \approx k_1/k_2 \times \chi C_DH\ . \qquad (6)$$

The reaction rate of hydrogen abstraction (k_1) has T_S dependence with activation energy of 5 $kcal \cdot mol^{-1}$, whereas that of hydrogen absorption (k_2) has no T_S dependence [But01]. Therefore, the number density of surface active site increases with increasing T_S. Decomposition of source methane gas into the methyl radicals cannot be expected on substrate surfaces in the T_S range used. On the other hand, when T_S is greater than ca. 1050 °C, graphite formation becomes considerable on the substrate [Spe94]. Equation (6) also indicates that the number density of reaction site $\chi\, C_D^{\bullet}$ does not depend on the atomic hydrogen density [Spe94, But01]. Actual growth surfaces are then not flat but have steps and terraces. The theoretical calculation indicates that desorption of hydrogen from the step edge is easier than that from the terrace. Therefore, carbon precursors are adsorbed preferentially at the step edges as has been discussed in Chapter 1. The activation energy E_a obtained experimentally is higher than that of $\chi\, C_D^{\bullet}$, which suggests the diamond growth is limited by reaction processes other than the hydrogen abstraction. Fundamental experiments of diamond growth along with theoretical aspects are needed to elucidate diamond growth mechanisms.

3.6.2. Experimental

The homoepitaxial films were deposited at different substrate temperatures, but otherwise using common process conditions of 6% C_{me}, chamber pressure of 180 Torr and deposition duration of 24 hours. All the substrates of this series have been pretreated prior to the deposition using a specially developed etching procedure which has been described in detail in the previous section and summarized in Table 3.3.

Plasma pre-treatment conditions	
Pressure	70 Torr
Power	900 W
Temperature	800 °C
Gas flow	500 sccm
O_2/H_2	4 %
Time	60 min

Table 3.3: *Standard plasma pretreatment conditions, using an enclosed holder.*

Sample N°	CH_4/H_2, %	Pressure, Torr	Power, W	Temperature, °C	Growth time, h
291104euos	6	180	850	750	23
61204euos	6	180	950	840	24
111204euos	6	180	1050	920	25
141204euos	6	180	1150	1010	24
171204euos	6	180	1250	1110	24
210105euos	6	180	1450	1200	26

Table 3.4: *Growth conditions of a series of samples grown at different temperature* T_S .

The substrate temperature was varied altering the discharge power as indicated in Table 3.4 because the substrate temperature could not be controlled independently from other process conditions in the system used for this work.

3.6.3. Results and discussion

In order to preserve the (100) surface quality the α-parameter value discussed in the section 3.4 has been further parameterized. Accordingly, the substrate temperature has been varied in a range of 700 – 1200°C with the aim to identify the temperature regime in which diamond deposition is optimized in terms of quality and growth rate.

Figures 3.15 and 3.16 show the surface morphology of six homoepitaxial films grown at a temperature interval of 700 – 1200°C. The morphologies are different at the altered substrate temperature and serve to highlight the α-parameter decrease with an increase of the substrate temperature. Based on the result in Fig. 3.15 and 3.16 one can see a systematic change of the surface morphology with an increase of T_S. At lower deposition temperatures between 700 - 850°C there are macroscopically smooth areas with no presence of secondary nucleation neither twin formation on the samples surfaces. There is a "bubbled" structure gradually transiting into a step-like pattern which is shown on a few DICM images taken from different regions present on a sample grown at 750°C (see Fig. 3.15(A1-3)), whereas as a result of the growth at 840°C a microscopically rough step-like structure is produced. Both samples (Fig. 3.15(A, B)) are composed of two different regions shown on the optical micrographs, which are probably induced by a slight substrate misorientation.

The SEM micrographs of the samples grown at the temperature higher than 900°C (Fig. 3.15(C)) reveal a transit to a different growth domain mode with the pronounced multitwin formation (as indicated with arrows in Fig. 3.15(C2)) .

The SEM and OM imaging techniques are combined to give more detailed information in the regions studied on the different surface structures. The SEM microphotographs of higher magnification are presented in order to identify the shapes of the twin defect structures while the OM images are more sensitive when observing the step bunching patterns with flat terraces (see Fig.3.15 (2,3), 3.16(2,3)).

From growth mechanism studies [But07] it is known that penetration twins are often observed on nominal (100) surfaces. According to this growth model they are formed by nucleation of twinned islands on a local surface region that has

(111) microstructures, such as might occur at etch pits on (100) planes (around dislocations) or macrostep edges (on vicinal (100) planes). Once formed these local twinned regions will not go away. This process eventually leads to the complete deterioration of the (100) surface since the growth steps cannot pass the twin boundary. In the growth configuration that has been studied the following process in detail has been as follows.

For the temperatures 700 – 850°C in this study the penetration twins are suppressed by a rapid overgrowth from the (100) region surrounding them. While in the temperature range of 900- 1200°C the twinned structures form more rapidly forming the core of growth hillocks, all depending on the relative growth rates of the slowest growing surfaces and the α-parameter [Wil93, Tam94]. As depicted in Fig.3.15 (C2) and 3.16(2) the twins grown on the (100) facet are developed in the form of a cubo-octahedron which occurs for $1.5<\alpha<2$ [Yan99], none of these twins is perfectly shaped. There is also an increased multitwin formation on the edges. Consequently the penetration twins help to the step bunching on the (100) regions in between the twins, by anchoring the step flow.

The steps are separated by the flat terraces of different sizes indicated in Fig. 3.16(3). When increasing the temperature, both SEM and OM micrographs for the samples grown in a temperature range of 920-1200°C show an increase in the flat (100) macro step bunched regions in between the twins, which mostly concentrate at the substrate edges. The twin formation on the edges gives rise to the lateral polycrystalline growth which promotes the propagation of steps across the substrate surface. The cracking of the samples edges is induced by a not well optimized substrate holder design.

AFM images assess the surface structural quality and the surface roughness on the different scales. Fig.3.15(4) and 3.16(4) show top-view AFM images of all the diamond samples of the temperature series in 3D representation in order to better illustrate the actual spacing of the terraces and their flatness. The AFM measurements indicate that the value of the root mean square surface roughness R_{rms} of the films grown in the 900 - 1200°C temperature interval ranged on average from 1 to 3 nm for a scan size of $5 \times 5\ \mu m^2$ at the flat terraced regions in between the twins, which is comparable to the results obtained for high C_{me} domain samples with the exception of that the high T_S samples are macroscopically rough.

Therefore the behavior of the (100) diamond growth rate has been also experimentally observed in the substrate temperature interval of 700-1200°C.

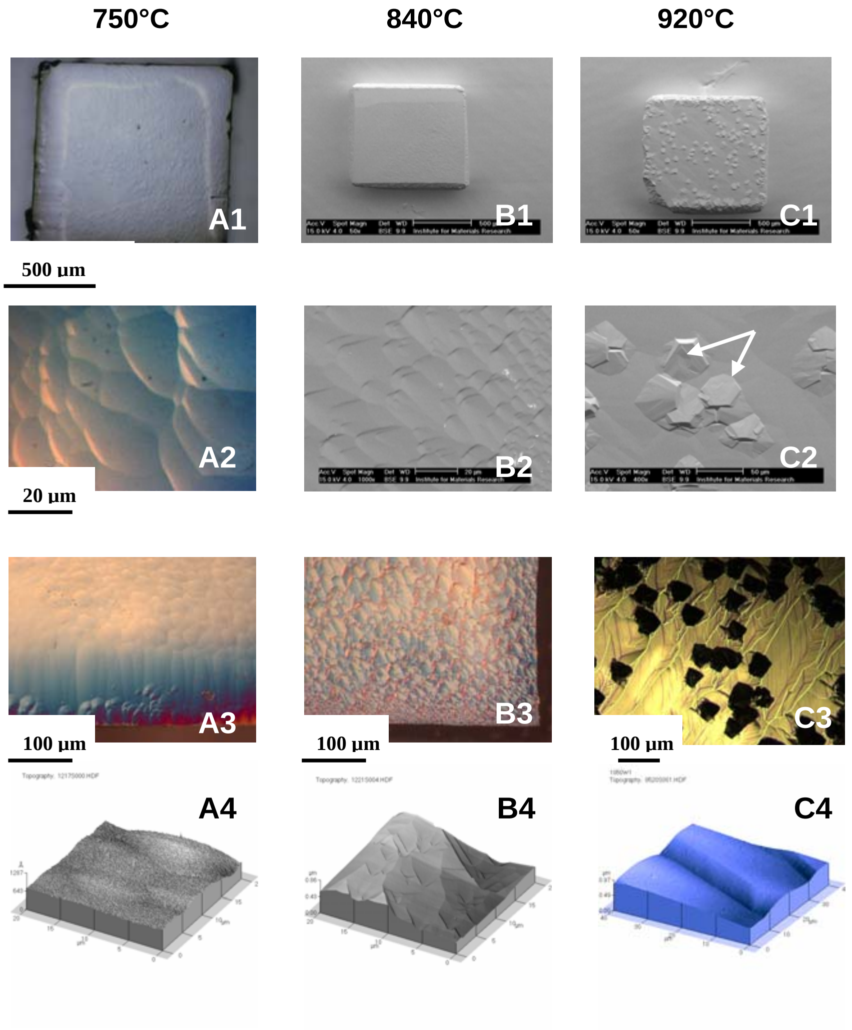

Figure 3.15: *Comparison of the surface morphology of the samples grown at* T_S *= 750 °C; 840°C; 920°C (A1-4; B1-4; C1-4 respectively), where (1): SEM or OM image of the whole sample; (2) SEM or OM image of higher magnification; (3): OM image of 500x700µm*^{2} *size; (4): AFM image of the sample ..The arrows point to the twins.*

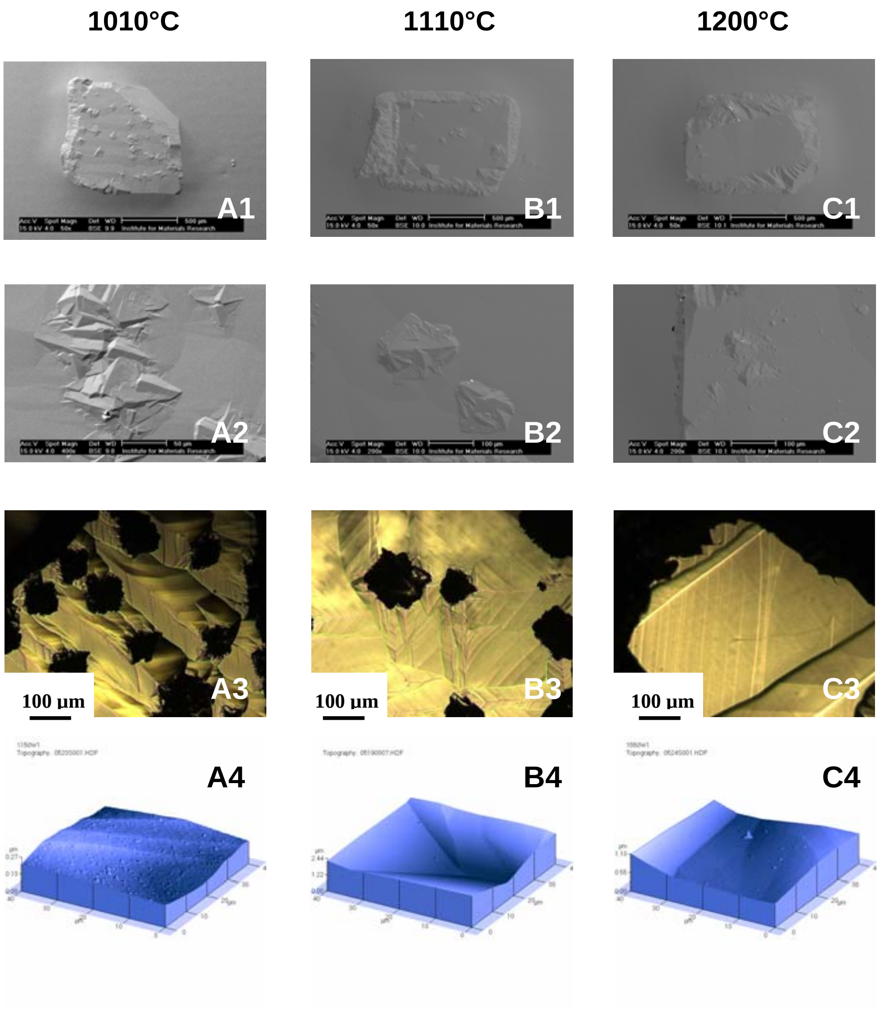

Figure 3.16: *Comparison of the surface morphology of the samples grown at T_S = 1010 °C; 1110°C; 1200°C (A1-4; B1-4; C1-4 respectively), where (1): SEM image of the whole sample; (2) SEM image of higher magnification; (3): OM image of 500x700µm^2 size; (4): AFM image of the sample.*

The E_a for the growth rate on (100) surface at the methane concentration of 6%, estimated in the substrate temperature range of 800–1000 °C, is 9 kcal mol^{-1}, which is consistent with the reported value for homoepitaxial (100) diamond for low-power MW PECVD [Chu92].

In this high C_{me} range, the growth rate is recognized to increase with increasing substrate temperature, as shown in Fig.3.17. Low E_a behavior for the dependence of the growth rate from T_S was observed for the C_{me} of 6 % which is consistent with other reports [Ach05, Ste98, Ter04]. The nearly linear dependence suggests that the growth model is relatively simple. The abovementioned result leads to the conclusion that under the given circumstances the best surface morphology results have been obtained at T_S around 700 – 750°C and C_{me} between 6 – 16 %. In the following the study has been concentrated on the investigation of the high C_{me} growth domain of the homoepitaxial growth with rather low temperature-power conditions. The substrate temperature is demonstrably one of the important parameters that determine the growth rate and crystalline quality.

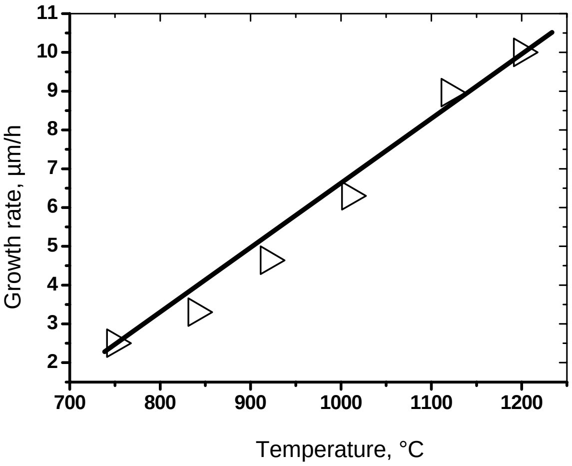

Figure 3.17: *Growth rate of deposited diamond films as a function of temperature T_S.*

3.7. Effect of misorientation angle

3.7.1. Introduction

The effect of the misorientation angle (θ_{mis}), which has been already briefly mentioned in Section 3. 4. θ_{mis} is defined as the declination angle of a flat plane of the polished substrate surface from the nearest crystallographic plane. The angle θ_{mis} affects the growth mode of the diamond crystal, similar to the methane concentration C_{me} and the substrate temperature T_S. Therefore, growth conditions must be optimized considering θ_{mis} to improve homoepitaxial film quality. Specifically for the step-flow growth mode, the growth rate is proportional to the number of radicals that reach the step edges through the migration along the terrace. With increasing θ_{mis}, a number of steps/terraces is increasing because the average terrace width is small, thereby increasing the growth rate. The saturation of the growth rate appears when the average terrace width determined by θ_{mis} is smaller than the average migration length of radicals. This growth model seems to explain well the experimental data. The possibility of surface migration on diamond surface under typical CVD conditions is theoretically reported [Fre97]. This model predicts the average migration length of radicals to be 1–10 nm at the substrate temperature of 700°C, which is consistent with experimental results. In this model, the diamond surface is covered with hydrogen, meaning that the number density of the surface reaction site depends on hydrogen abstraction rate as discussed in Chapter 1 and this is for the optimal experimental conditions (low temperatures) low because of stable hydrogen bonding with diamond, this explains also relatively low growth rate in the conditions reported here. Second, the substrate temperature seems to be also low for radical migration. Lattice vibration of the substrate promotes radical migration, and the degree of the lattice vibration is related to the Debye temperature of the substrate material. For example, the Debye temperature of silicon is ca. 600 K, whereas for diamond, however, the Debye temperature is ca. 2000 K, meaning that the diamond substrate, of which the typical temperature is below 1000 K, is cold in the viewpoint of the lattice vibration under the diamond CVD condition. Remarkable surface migration is unlikely to occur on the diamond surface under the low temperature condition, as suggested theoretically [Har93, Meh90].

Microscopically, the 2×1/1×2 double domain structure was reported to be formed on the (100) crystal plane at lower θ_{mis}, whereas the surface comes to have the 2×1 single domain structure with increasing θ_{mis} [Tsu94, Tak99]. The relationship between the growth rate and θ_{mis} was reported in detail by Tsuno *et al.* [Tsu96]. When Cm was as small as 1%, the growth rate increased in proportion to θ_{mis}, but the growth rate saturated above a certain θ_{mis} (i.e. >5°). This feature was explained by using the step-flow growth mode. When the methane concentration was as high as 6%, the growth rate was independent of θ_{mis}, and two-dimensional nucleation growth was observed. Based on the experimental results, it was suggested that as θ_{mis} increases, the anomalous growth including formation of unepitaxial crystallites tends to be suppressed [Bau05]; also at high θ_{mi} bunching steps appear over the entire sample surface with an average terrace width of ca. 1 µm.

3.7.2. Experimental

The growth was carried out in the same deposition system as has been already described with the identical experimental conditions if not mentioned otherwise using a gas mixture of hydrogen (7N) (99.99999%) and methane (4N) (99.99%) . In order to improve the purity of hydrogen and accordingly the films purity as will be shown in Chapter 4 the hydrogen generator purification system was applied, which allowed producing (7N) hydrogen purity.

Sample N°	θ_{mis},°	CH_4/H_2, %	Pressure, Torr	Power, W	Temperature, °C	Growth time, h
21205euos	0.08	10	180	620	710	119
101205euos	0.92	10	180	600	720	94
141205euos	2.07	10	180	600	700	119
160106euos	2.87	10	180	600	700	161
280106euos	3.99	10	180	620	700	111
100106euos	5.91	10	180	570	700	126
210106euos	8.09	10	180	650	700	135
250106euos	9.07	10	180	610	700	69

Table 3.5: *Growth conditions of a series of samples grown at different* θ_{mis}.

The misorientation angles of mirror-polished substrate surfaces with respect to the (100) plane in the range of 0–9° were determined by X-ray diffraction with a precision of ± 0.01°. All the substrates of this series have been pretreated prior to the deposition using a specially developed etching procedure which has been summarized in the previous section in Table 3.3. The dimensions of the substrates were 3 × 3 × 0.5 mm^3. All the growth experiments were carried out with the optimal experimental conditions found in the previous sections: specifically, high C_{me} and low T_S have been used. The growth conditions are mentioned in Table 3.4.

3.7.3. Results and discussion

In order to decouple the influence of misorientation angle and the surface quality on the secondary nucleation, substrates with low surface defect density, and additionally O_2/H_2 plasma etching were used to obtain surfaces free from scratches and polishing lines.

Low deposition temperature of 700°C in combination with high methane concentrations have been chosen in favour of the growth of (100) facets promoted by the van der Drift selection rule, i.e. the morphology is governed by the dominance of the fastest growing crystal direction. This means that the growth rate of (100) facets growing in (100) direction will be presumably larger than that of other differently oriented crystallites that could be hereby avoided.

The surface morphology of CVD diamond films grown at 700°C differs notably with the surface misorientation angles of (100) substrates, as shown in Fig. 3.18. The following results have been obtained. For the films with θ_{mis} in the range of 0-3° step bunching is not clearly observed, and smooth surfaces with atomic island structures (Fig. 3.18(E, D)) and randomly appearing round growth features of lateral sizes of <100 µm and heights of <50 nm are optically observed, which is shown in Fig. 3.18 (E) for about 500 µm thick layers (21205euos, 101205euos, 141205euos). The round hillocks are found to originate from the not optimized etching pretreatment giving rise to an enlarged size of etch pits which at present growth mode promote the 3D defective structures formation in a round bubble shape as discussed in Section 3.5. Thus in this growth conditions we have not observed the step flow/bunching.

The optical images of the sample grown on a 3.99° misoriented substrate for 111 h shown in Fig. 3.18(C1-2) demonstrate a combination of flat areas with atomic island structures similar to the samples grown on 0-3° misoriented substrates.

This is seen in the magnified DICM image together with a number of etch-pits which are the sources of steps appearing in some regions. An increased number of etch pits after the etching step is caused by an increase of θ_{mis} value which is consistent with other reports [Ri06]. Here, at θ_{mis} of about 4° a change of the growth mode from the clear island mode to the step flow mode has been observed.

The steps are also observed on the film deposited for 126 h on the 5.9° off angle surface Fig. 3.18(B1-2). This sample contains a considerably less number of regions where atomic island structures are present; the sample is consistently covered with the step bunching patterns running across the whole sample surface.

The growth on the substrate with θ_{mis} of 9.1° for 69 h produced macroscopically rough step-like structures Fig.3.18 (A1-2). The faces show an increase in roughness due to accumulation of steps to bunching patterns when increasing the degree of misorientation. The above discussed results show that growth steps of different sizes causing a rough surface are notably developed on the highly misoriented surfaces after deposition therefore AFM measurements could not be performed on the films grown on 6-9° misoriented substrates due to an increasingly rough morphology. Under these conditions and for 6–9° of misorientation, the growth mode is mainly the step-flow mode as confirmed by the observed step bunching (see Fig. 3.18). Neither pyramidal hillocks nor unepitaxial crystallites were observed on the series of 0–9° misoriented films. However square-shaped pits of a size of < 50 µm were found on the grown films.

Another observation related to the growth conditions used is that no drastic change in the deposition rate with respect to the substrate has been found, contrary to the influence of a variation of the used C_{me} in the range of 6 – 15 %. As an example a growth rate of 10 µm/h was achieved for the highest CH_4 content used here (15%) together with the 'open'- type of holder. To achieve a deeper insight into the atomic growth mechanism on the films grown on the substrates with θ_{mis} of 0 – 3° at high C_{me} of 10-15% and low T_S of about 700°C AFM characterisation has been implemented, which will be thoroughly discussed in Section 3.9, where the island growth model will be elaborated.

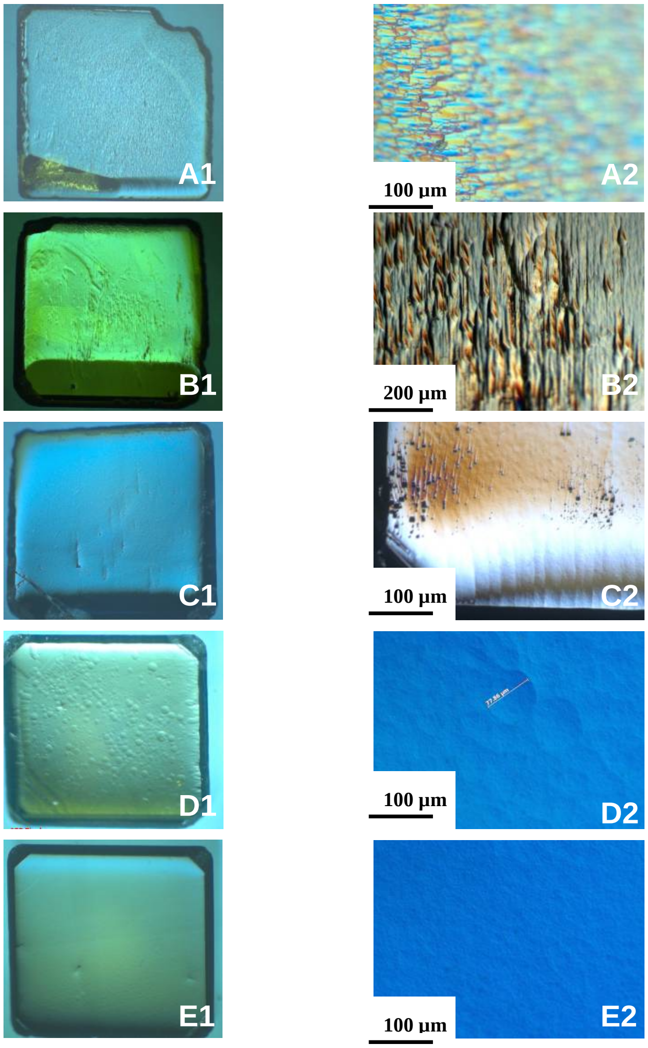

Figure 3.18: *DICM images of a series of films grown at different* θ_{mis}*: 9.07; 5.91; 3.99; 2.07; 0.08° (A, B, C, D, E respectively). The images in the right column show the whole samples surface; the images in the left column show their detailed view.*

3.8. Micro-Raman mapping before and after growth

3.8.1. Introduction

The aim of this section is to study by Raman spectroscopy mapping the influence of the substrate quality (zoning, disorientation of sectors, N concentration in zones, etc.) on the resulting quality of the layers grown. The Raman setup has been discussed in Chapter 2.

The parameters of Raman lines, such as the intensity, the wavenumber and the full width at half maximum give different information about the crystal quality and therefore it is very important to study their behavior. For a given measurement geometry, the intensity of the Raman line partially reflects the absorption of light from the crystal and provides evidence of possible disoriented sectors in the crystal lattice. Each Raman line exhibits a frequency shift (width change) whenever a strain is present in the crystal. Width and frequency of the Raman peak are closely related to each other. Variation of the wavenumber can depend on the presence of impurities, such as nitrogen, which can either cause a change in the lattice constant [Fie92] and/or reduce the phonon lifetime.

When detecting the Raman spectrum, at the same time the PL spectrum is detected. The PL spectrum provides another important assessment of the crystal quality revealing the presence of defects centers such as H3, $(N\text{-}V)^0$, amorphous carbon etc., discussed later. Therefore, the combination of Raman imaging, together with optical and birefringence images represents a wide source of information on the crystal quality, and in particular as far as concerning the spread of impurities such as N.

3.8.2. Experimental

Several HPHT Ib Sumitumo substrates were studied by Raman spectroscopy. In this paragraph, 2D spectral images obtained on two 2.5×2.5 mm^2 substrates and on the films deposited onto them are discussed. After the careful characterization of the substrates by DICM and Raman spectroscopy, the two homoepitaxial layers have been deposited onto the respective substrates using the standard process conditions summarized in Table 3.5 including the plasma pretreatment step.

Sample N°	Substrate N°	CH_4/H_2, %	Pressure, Torr	Power, W	Temperature, °C	Growth time, h
10707euos	Sb1	10	180	600	700	34
30707euos	Sb2	10	180	500	700	23

Table 3.5: *Growth conditions.*

Raman spectra were taken using the following conditions: an objective with low magnification (×10, depth of field equal >100 µm) and a 514.5 nm laser focused on the surface, were used to analyze the whole sample, the point spacing being 25 µm, whereas for Sb2 besides using the aforementioned conditions an excitation in the UV range (363 nm) in order to use higher resolution conditions. It must be noted that the spectral resolution using the 363 and 514 excitations are different, that is why this induces the width images difference. Second, the 363 nm excitation is located on an absorption feature of nitrogen. Thus, the use of this excitation wavelength increases the contrast on the intensity images which is due to differences in the nitrogen content. When more detailed information was needed, a high magnification objective (×100, depth of field equal to 10 - 20 µm circa, the point spacing was 0.6 µm) was employed. Images were created by extracting the line of interest (diamond line) from the "image field" and by fitting each individual spectrum by using a Lorentzian curve and by using a linear background. The parameters of the line, such as the intensity, the wavenumber and the full width at half maximum, were plotted as function of the spatial coordinates in order to assess their variation in the whole crystal surface.

Crossed-polarization birefringence images were also acquired as they provide information about the existence of strain in the crystal.

3.8.3. Results and discussion

3.8.3.1. Mapping of substrates before growth

In Figures 3.18 and 3.19 Raman imaging results are shown for the two Sumitumo substrates. Optical images (a) and cross-polarized birefringence images (b) were recorded in order to get first information on the analyzed crystals. As observable in both cases, the two optical images recorded in transmission mode, have a yellowish color indicating the presence of a larger amount of nitrogen in a portion of the crystal with respect to the rest. The cross-polarization birefringence images give information about the strain in the crystal, corresponding to the very bright regions, and observable in both substrates. For both substrates the 2D maps were recorded by analyzing the whole surface with a step increase of 25 µm. For the substrate Sb1 in Figure 3.19 a zebra-like pattern on the frequency and width images is induced by an imperfect flatness of the sample leading to the observed interference pattern. The intensity map for Sb1 (Fig.3.19(c) is weaker in correspondence with the sites where nitrogen is present in higher concentration, due to the higher absorption, while the width, in the all yellow region observable in the optical image, is about 0.2 cm^{-1} larger than in the rest of the crystal. When comparing the intensity, PL intensity, frequency and width images with the optical images it is seen that they perfectly correspond. Thus, the contrast in stripe-like sectors which is evidenced as horizontal lines is induced by differences in the nitrogen content.

For the substrate Sb2, in Fig. 3.20, two very distinguishable growth sectors can be identified in all the maps, which correlate to different nitrogen content. The intensity map (Fig.3.20(c)) exhibits for the substrate Sb2 a much brighter area, which is caused by a sharp difference in the nitrogen content. Consequently, in the more yellow regions the highest concentration of nitrogen is present. This result indicates that the substrate Sb2 is not purely monocrystalline. The width variation, displayed in map (f), is in this case more important than for the other substrate, showing a strained area in the vicinity of the corner. The strain is expected to be higher in the vicinity of the corner, where the "edge" effects are higher. For the whole crystal, the contrast on the frequency and width images has to be related to differences in the nitrogen content. However, the frequency and width images (Fig.3.20 (e,f)) show in the entire substrate surface a very low contrast, always, equal to ±0.05 cm^{-1} at maximum.

In order to study the local variation of the Raman-line parameters, high-resolution 2D maps were performed in different zones of the substrates. The results of local measurements in the areas of typical polishing defects common for the both substrates are illustrated in Fig. 3.21 (analyzed area equal to 100×100 μm^2). These Raman maps were recorded by using a 363 nm laser and an objective ×100 - depth of field equal to about 10-20 µm, giving a spatial resolution of 0.6 µm. Only at these high resolution conditions it was possible to detect the polishing defects in the intensity images, usually easily observed with DICM optical microscopy as discussed in Section 3.5. Again the higher absorption areas on the intensity image correspond to the areas with higher nitrogen concentration, where the width image has a little contrast

a) Optical image in transmission mode **b) Cross-polarizers**

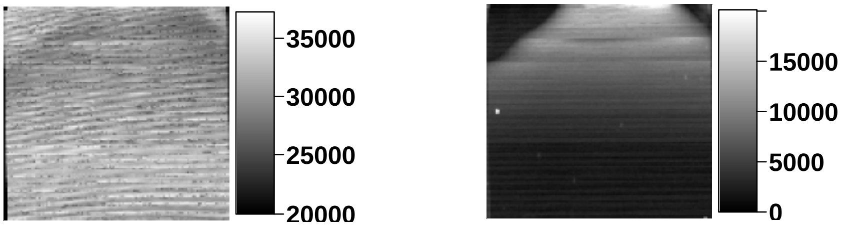

c) Intensity (a.u.) **d) Photoluminescence**

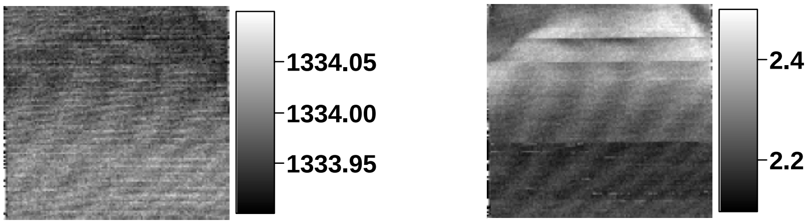

e) Frequency (cm^{-1}) **f) Width (cm^{-1})**

Figure 3.19: *Micro-Raman 2D images of Sb1 (objective magnification equal to x10) using a 514 nm laser excitation source. a) optical image recorded in transmission mode; (b); crossed-polarisation birefringence image. Maps c), d), e) and f) represent respectively the spatial variation on the whole substrate surface of the Raman intensity peak, the photoluminescence signal, the Raman shift and the full width at half maximum of the Raman peak.*

a) Optical image in transmission mode

b) Cross-polarizers

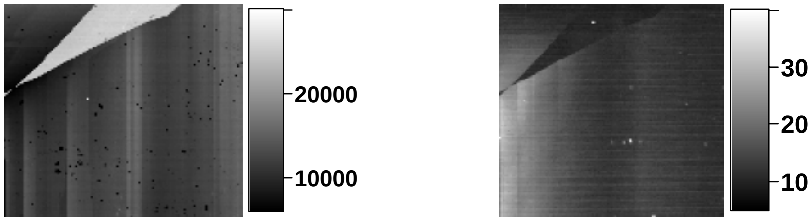

c) Intensity (a.u.)

d) Photoluminescence

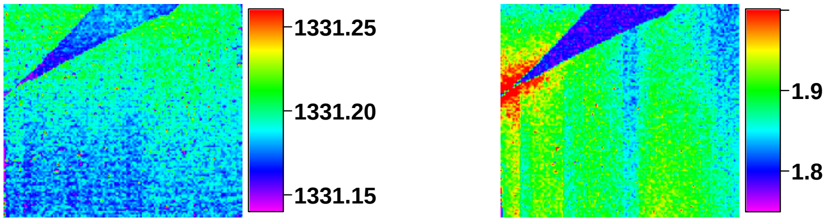

e) Frequency (cm^{-1})

f) Width (cm^{-1})

Figure 3.20: *Micro-Raman 2D images of Sb2 recorded using an excitation in the UV range (363 nm) and an objective x10. a) optical image recorded in transmission mode; (b) crossed-polarisation birefringence image. Maps c), d), e) and f) represent respectively the spatial variation on the whole substrate surface of the Raman intensity peak, the photoluminescence signal, the Raman shift and the full width at half maximum of the Raman peak.*

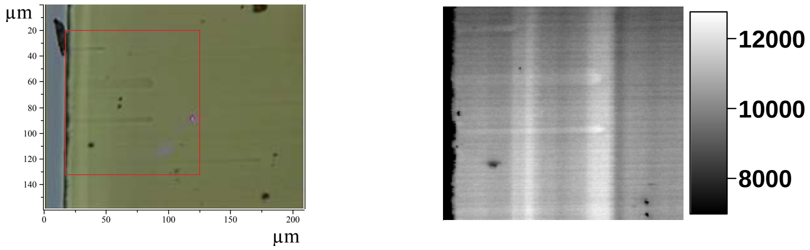

a) Optical image in transmission mode **b) Intensity (a.u.)**

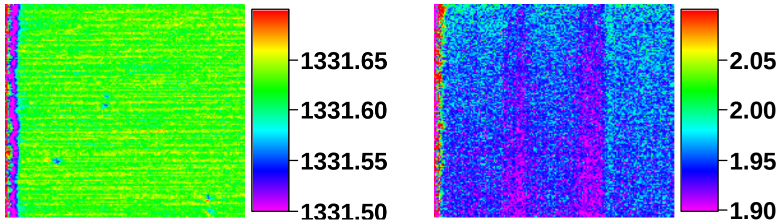

c) Frequency (cm^{-1}) **d) Width (cm^{-1})**

Figure 3.21: *Surface Raman imaging of the area with polishing defects of Sb2 recorded by using an excitation in the UV range (363 nm) and an objective magnification ×100, the probing depth is high (10-20 µm with the current detection conditions). a) Optical image with the polishing defects. The highlighted box in the optical image indicates the analyzed area (100 × 100 µm^2, point step equal to 0.6µm). Maps b), c) and d) represent respectively the spatial variation on the whole substrate surface of the Raman intensity peak, the Raman shift and the full width at half maximum of the Raman peak.*

corresponding to the intensity image, whereas the width change is only about 0.05 cm^{-1}. In conclusion, both analyzed substrates show an average width value ranging between 1.6 cm^{-1} and 2.4 cm^{-1} at maximum, with a local variation that never exceeds a few 0.1 cm^{-1}.

3.8.3.2. Mapping of grown films

The 2 substrates Sb1 and Sb2 investigated by micro Raman imaging technique in the previous section have been used as the seeds for the deposition and investigation of the growth influence on the structural quality and strain distribution in the homoepitaxial layers. The substrate and the film optical images of both 10707euos and 30707euos samples are compared in Fig. 3.22(a, b) and 3.25 (a, b). The observation reveals that the films inherited the deep polishing grooves relief that have not been flattened enough by the plasma etching pretreatment of the substrates before the deposition as has been already discussed in Section 3.5.

Micro-Raman 2D images of film 10707euos grown on substrate Sb1 recorded using an excitation laser (363 nm) and an objective ×10 are shown in Fig.3.22. The frequency of the diamond line is homogeneous for the most of the crystal. However, the edges of the crystal, in fact, the part which is grown laterally outside the substrate are stressed compressively. The circular area which can be detected within the center of the crystal is most probably an artifact, due to the fact that the crystal is not perfectly flat. Some defects detected on the optical, intensity, frequency images and partially on the width image are indicated with the arrows on the intensity image in Fig 3.22(d).

Fig.3.23. shows a detailed analysis of one of such defects. The optical image which is recorded with cross polarizers reproduces the intensity image as shown in the map (b). The contrast is due to misoriented areas. Within the centre of the defect (map d) stress is shown to be compressive, while 4 tensile “spots” are detected in a rectangular pattern. The strain field is localized about 30 μm around the centre of the defect. This square pattern is more or less oriented along the <110> directions. A cross-like pattern is detected on the width image (map e) with the same approximate directions. The origin of such defects probably comes from the etch pits on the substrates which are dislocation related.

The same kind of defects are observed with cross-polarized microscopy and analyzed in Fig.3.24 (1). PL spectra (2) recorded at the defect centres (a, d) and indicated in the photoluminescence map (3) show a broad band, centered at about 600 nm, which is known to be amorphous carbon attributed. These amorphous carbon clusters are detected at the interface between the epilayer and the substrate and a few microns in size, easily detected by OM. Otherwise, the PL spectra probed from the flat areas, which are typical for both samples as shown in Fig.3.24 (2(b, c, e)), all of them show the PL defect lines of the H3 (305.2 nm) and $(N\text{-}V)^0$ (575 nm)

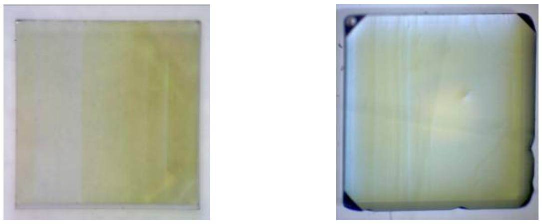

a) Substrate Sb1 **b) Film 10707euos**

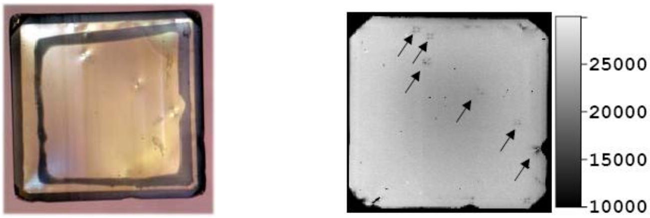

c) Cross polarizers **d) Intensity (a.u.)**

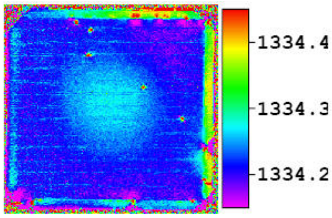

e) Frequency (cm^{-1}) **f) Width (cm^{-1})**

Figure 3.22: *Micro-Raman 2D images of film 10707euos grown on substrate Sb1 recorded using an excitation laser (363 nm) and an objective x10. a) Optical image of Sb1 recorded in transmission mode; b) optical image of film 10707euos recorded in reflection mode; c) crossed-polarisation birefringence image of the grown film. Maps d), e) and f) represent respectively the spatial variation on the whole substrate surface of the Raman intensity peak, the photoluminescence signal, the Raman shift and the full width at half maximum of the Raman peak. The arrows on the intensity image point to the defects found.*

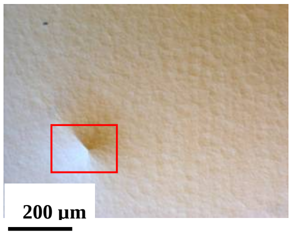

a) DICM image

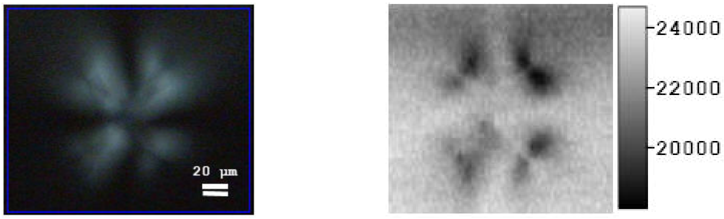

b) Cross polarizers

c) Intensity (a.u.)

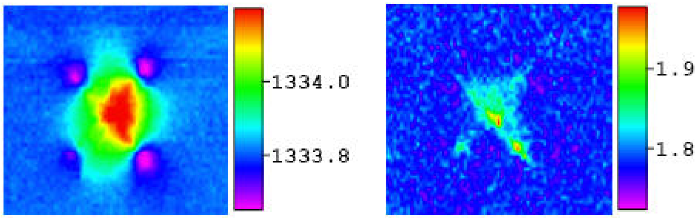

d) Frequency (cm^{-1})

e) Width (cm^{-1})

Figure 3.23: *Surface Raman imaging of the area with cross-like defects at film 10707euos recorded by using an excitation in the UV range (363 nm) and an objective magnification x100. The highlighted box in the DICM image (a) indicates the analyzed area (200 x 140 µm^2, point step equal to 0.6µm), indicated in the cross-polarized image (b). Maps c), d) and e) represent respectively the spatial variation on the whole substrate surface of the Raman intensity peak, the Raman shift and the full width at half maximum of the Raman peak.*

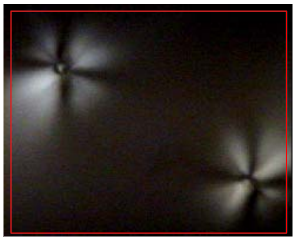

1) Cross polarizers

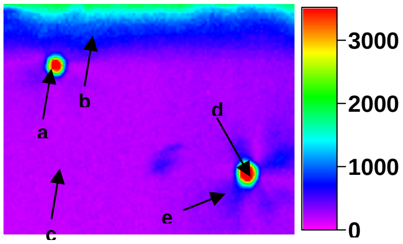

3) PL intensity at ~ 600 nm

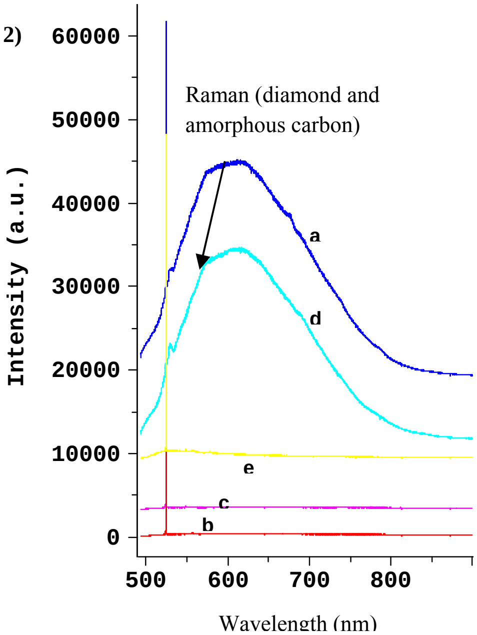

Figure 3.24: *Surface Raman imaging of film 10707euos, probed area identified by the square in the cross-polarized image (1). The five PL spectra (2) (indicated as a, b, c, d, e) correspond to the analyzed points indicated by the arrows in the false-color photoluminescence map (3). (PL spectra are not corrected for the instrument response).*

centers. Another feature at about 786 nm is hardly observed with the present acquisition conditions.

The second sample 30707euos shows no presence of cross-like defects which is demonstrated in Fig. 3.25. The frequency of the diamond line (map e) is rather constant above the seed crystal. The triangular area, which is a substrate growth sector with a lesser nitrogen content, is also detected on the film frequency image, but the contrast is low. From the abovementioned we can conclude that the overall quality of the crystals in terms of stress is rather good.

a) Substrate Sb2 **b) Film 30707euos**

c) Cross polarizers **d) Intensity (a.u.)**

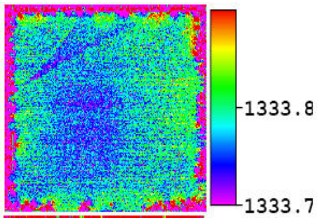

e) Frequency (cm^{-1}) **f) Width** (cm^{-1})

Figure 3.25: *Micro-Raman 2D images of film 30707euos grown on substrate Sb2 recorded using an excitation laser (363 nm) and an objective x10. a) Optical image of Sb2 recorded in transmission mode; b) optical image of film 30707euos recorded in reflection mode; c) crossed-polarisation birefringence image of the grown film. Maps d), e) and f) represent respectively the spatial variation on the whole substrate surface of the Raman intensity peak, the photoluminescence signal, the Raman shift and the full width at half maximum of the Raman peak.*

3.9. Model of the island-growth mechanism

3.9.1. Introduction

The surface morphology of homoepitaxial diamond films varies microscopically and macroscopically depending on C_{me}, T_S and θ_{mis}. It is generally recognized that the actual growth surfaces are not flat but have steps and terraces and the main growth mechanism of diamond growth is the step flow mechanism. Several research groups have made efforts to characterize the mechanisms of homoepitaxial growth on the (100) diamond surface in terms of surface morphology [Lee97, Tsu94, The00]. In the present study, AFM and STM confirm that the surfaces of (100) grown layers exhibited a morphological change from different sized growth steps and terraces dominating the surface morphology to a near-atomically flat island type of surface.

The following morphological features have so far been observed on the (100) diamond films grown by CVD: monatomic-height or single–layer steps along <110>; diatomic–height or double–layer steps along <110>; growth hillocks which facets are comprised of steps and unepitaxial crystallites. Under typical growth conditions in which C_{me} is 0.5–2%, T_S is 700–900 °C, with a misorientation angle θ_{mis} of ca. 3°, bunching steps are usually observed on the homoepitaxial surface, whereas the 2×1 single-domain structure appears microscopically. The step-bunching surface comprises flat terraces with double-step height of 0.18 nm between two terraces [Hay96, Tsu94, Lee95, Tak00]. The average terrace width is consistent with the θ_{mis} of the substrate examined. On the other hand, when C_{me} is higher than 2% and θ_{mis} lower than 3°, the surface has 2 ×1/1 × 2 double-domain structures. These features are inferred to originate from higher growth rates of two-dimensional nucleation on terraces instead of the lateral growth rate from steps [Tsu96, Tsu94].

During the growth the as-grown homoepitaxial (100) diamond surface is reconstructed and terminated with hydrogen. Dimer rows are observed to extend beneath terraces in the direction perpendicular to the step edge lines. Steps on the (100) surface are categorized into the S_A-type step that is parallel to the dimer rows on a terrace or the S_B-type step that is perpendicular to the dimer rows. Experimental observations suggest diamond growth from the edge of the S_B-type step is dominant on the (100) crystal plane [Tsu91]. This growth mechanism is supported theoretically in Chapter 1. In this growth model, the dimer shift process from the edge of S_B-type step is the largest endothermic process and its energy is reported to be 6 kcal·mol^{-1} [But01]. This is close to our value of observed activation energy of 6 kcal mol^{-1}. On the other hand, some reports suggest that growth from the S_B-type step edge is unremarkable [Kaw95].

In epitaxial growth of thin films, the growth mechanism that determines the different surface morphologies and therefore the physical properties of films must be understood from the point of view of the atomic structure of the surface.

3.9.2. Experimental

Single-crystal diamond layers have been grown using the standard optimal process conditions summarized in Tables 3.7 and 3.8 and the deposition setup described in Chapter 2.

Plasma pre-treatment conditions	
Pressure	70 Torr
Power	900 W
Temperature	800 °C
Gas flow	500 sccm
O_2/H_2	4 %
Time	60 min

Table 3.7: *Standard optimal plasma pretreatment conditions, using an enclosed holder.*

After growth, the single-crystal layer is either chemically oxidized or plasma hydrogenated or graphitized. Oxidation of the diamond sample is carried out by using the chemical acidic treatment as has been already described in order to remove all contaminants on the diamond surface.

For hydrogenation, the sample is put back into the deposition chamber and the hydrogenation treatment is carried out in a pure hydrogen plasma. For this hydrogenation treatment, we create a plasma at a substrate temperature of 700 °C and a pressure of 70 Torr. A microwave power of 700 W and a hydrogen flow of

Sample N°	C_{me},%	*p*, Torr	***P**,* W	T, °C	time, h	$\theta_{mis,}$ °	holder
101206euos	10	180	600	720	94	0.9	enclosed
141206euos	10	180	600	700	119	2	enclosed
241005euos	10	180	550	700	125		enclosed
180806euos	15	180	590	700	22	0.6	open
241106euos	7	180	550	700	1		enclosed
70305euos	7	180	560	700	4		enclosed
290806euos	15	180	500	700	18		open

Table 3.8: *Growth conditions of a selection of samples studied in this section.*

500 sccm is used and the plasma is kept on for about 1 - 5 min after the pressure stabilization (which takes about 2 minutes). After removing the sample from the vessel and a subsequent contact with the ambient, the surface resistance drops to about 20–100 kΩ/cm^2, as measured by a two-point contact method using carbon contacts. After the hydrogenation treatment the surface graphitization is carried out using the Ar beam graphitization conditions described in Table 3.9.

Ar-treatment conditions	
Pressure	5.8 10^{-5} torr
Beam voltage	500 V
Beam current	9 mA
Discharge voltage	38 V
Discharge current	0.19 A
Time	5 min

Table 3.9: *Ar-treatment conditions.*

The morphology of grown diamonds was characterized by means of DICM, AFM and STM measurements. The AFM measurements were performed using a Vecco Multimode microscope equipped with the quadrex module operating in tapping mode using etched Si tip-probes (Nanoscensors GmbH, tip radius 5-10 nm).STM measurements were carried out using an Omicron UHV STM (Ultra High Vacuum STM) apparatus at T = 77.5 K, equipped with a PtIr tip-probe. UHV is used to prevent the surface to attract adsorbates again after annealing.

3.9.3. Results and discussion

The growth of atomically flat homoepitaxial layers has been already demonstrated by Okushi *et al.* [Oku01], where the step flow growth mechanism is considered to be the main growth mechanism. The layers exhibited atomically flat surfaces for film thicknesses between 1 - 10 µm with tens of nm thick terraces separated by monatomic steps running parallel to the (110) direction, as it was observed by atomic resolution AFM (see Fig.3.26).

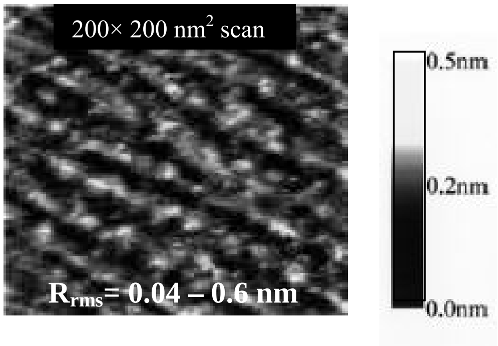

Figure 3.26: *AFM topography of atomically flat surfaces (adopted from ref. [Oku01])*

In this study high methane concentrations, low temperatures and misorientation angles between 0-3° were used to evaluate its influence on the (100) diamond growth mechanism. Step bunching is not macroscopically seen, and smooth surfaces are optically observed. The typical surface morphologies observed with DICM microscopy of the films grown in this specified growth domain conditions are demonstrated to be substantially flat, which is shown in Fig. 3.27 (a) for about 500 µm thick layers (here sample 241005euos). Round hillocks with lateral sizes of <100 µm which differ from typical rectangular pyramidal hillocks were found to randomly cover the sample surface (Fig. 3.27 (b) – sample 101206euos). In contrast to the OM images, such growth hillocks are only slightly apparent in the corresponding SEM images, indicating that the hillocks resemble electronically those in the remaining flat regions. Some relation has been found between the plasma etching pretreated surface morphology and the consequently grown film surface morphology. The round hillocks were found to correspond to etch pits of larger dimensions due to not well tuned plasma etching conditions together with the ‘open’ substrate holder type. Formation of such round shaped features on the sample surface is suggesting the change of growth mode from the lateral growth to island growth using the methane rich conditions.

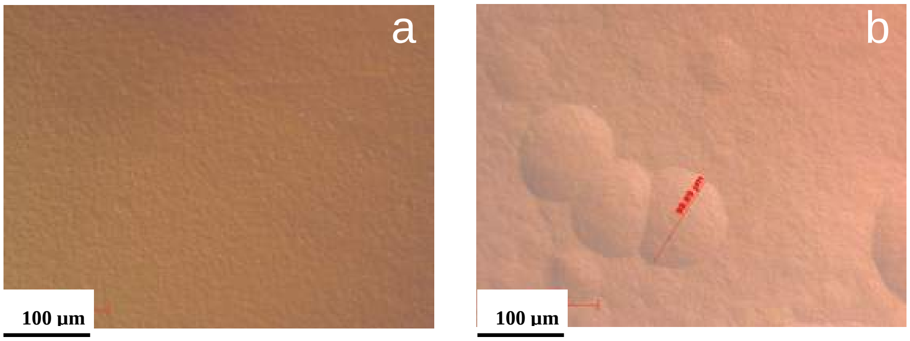

Figure 3.27: *Typical optical microscopy images of homoepitaxial diamond films grown at 10% CH_4/H_2 using substrates with 0 – 3° misorientation angles: (a) flat region; (b) region with round hillocks.*

To achieve a deeper insight into the atomic growth mechanism AFM characterization has been implemented on the films grown on 0 – 3° misoriented substrates at 10-15% C_{me}.

Fig. 3.28 shows typical height and amplitude surface morphologies of the good quality homoepitaxial diamond films grown on 0 – 3° misoriented substrates, where the amplitude image is given to show the enhanced contrast of nm-sized features. In the figure, (a) represents a top-view height and (b) amplitude AFM images for (1×1) μm^2 for a θ_{mis} of 0.6° at 15% C_{me} for 22 h deposition (sample 180806euos). Values of the surface roughness in the range 0.5 – 1 nm for the 1×1 μm^2 were measured on this film. Fig.3.28 (c) represents a top-view height and (d) amplitude AFM images for (150×150) nm^2 scan size for θ_{mis} of 2° at 10% C_{me} for 119 h deposition (sample 141206euos). In our case the values of the surface roughness were in the range of 0.1 – 0.3 nm for a 150×150 nm^2 scan size. As shown in the figure, 3. 28 near-atomically flat surfaces that consist of a few tens of nm sized ‘grains’ have been clearly observed in both cases. This is evidently a different situation than the same nearly atomic flat diamond film surfaces grown by Okushi *et al.*, shown in the Fig. 3.26 grown by a step flow growth. This structure is further examined close in details.

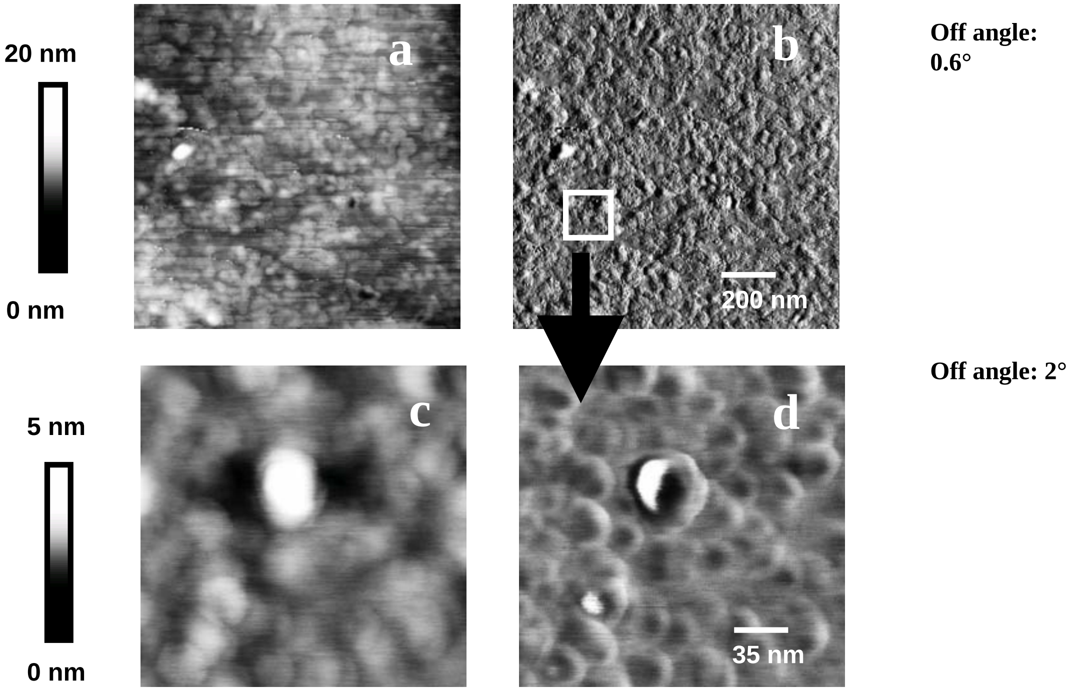

Figure 3.28: *Typical surface morphologies AFM images of a few hundred microns thick homoepitaxial diamond films grown on 0-3° misoriented substrate: (a) height and (b) amplitude AFM images for 150x150 nm*^{2} *scan size for the misorientation angle of 2° at 10%* CH_4/H_2 *ratio for 119 h deposition (sample 141206euos); (c) height and (d) amplitude AFM images for 1x1 µm*^{2} *scan size for the misorientation angle of 0.6° at 15%* CH_4/H_2 *ratio for 22 h deposition (sample 180806euos).*

In order to get atomic resolution surface images of the as-grown homoepitaxial layers to investigate the growth mechanism leading to such island structured surfaces, high resolution low nitrogen temperature (LNT) STM studies have been performed on the thin layers grown at the standard optimal growth.

The as-grown samples 70305euos and 241106euos grown at C_{me} of 7% have been pretreated by an Ar bombardment procedure described in Table 3.9 followed by annealing at 450°C for 3h. The surfaces of the samples have been shown to be conductive enough due to graphitization occurring on the diamond surface as a result of the Ar bombardment. Thus this technique is suitable for performing STM measurements and imaging the surface with high resolution.

The atomic resolution STM imaging of the sample 70305euos demonstrated in Fig. 3.29(a, b) reveals that the surface comprises nano-particles making up the atomic island appearance of the surface. The average distance between atoms that are visible inside the clusters is about 2.3 Å (see the profile in Fig. 3.29(b)), which is in a good correspondence with the typical interatomic distance of graphite evidencing that the surface is graphitized.

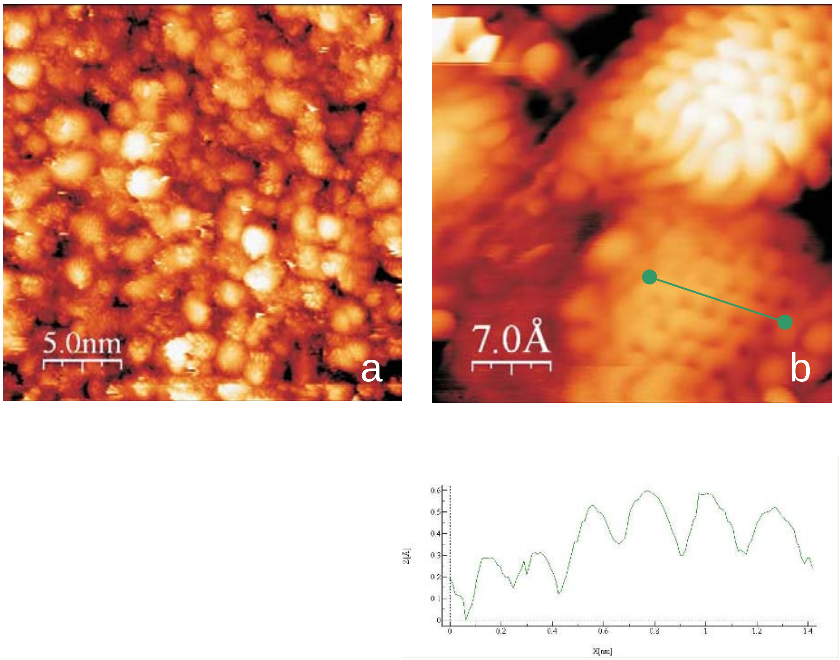

Figure 3.29: *STM images of a few microns thick homoepitaxial diamond films grown at high C_{me} on 0-1° misoriented substrate graphitized by Ar sputtering surface of as-grown diamond film.*

This phenomenon of nano-sized clusters brought up doubts about the monocrystallinity of the layers, though all other studies including the Raman supported it strongly. The subsequent hydrogenation step for 0.5 min of the sample surface followed by the additional STM measurements allows STM imaging of hydrogen terminated diamond surfaces with atomic resolution showing surprisingly that 2×1 domains which are ordered arrays of C-C dimer bonds on different terraces as a result of step flow hydrogen etching (see

Fig.3.30(a, b)). This is the evidence that the layer beneath the nano-sized clusters is purely monocrystalline and therefore the nano-sized clusters are only on the surface and in the nanometer range, which means that the sample is a single crystalline diamond, as confirmed by Raman spectroscopy in Section 3.8. However, the surface pattern is drastically different to the usual (100) diamond surface comprising micro or macro steps, hence that evidence points to the conclusion that the samples must be grown by another mechanism, i.e. the island growth mechanism.

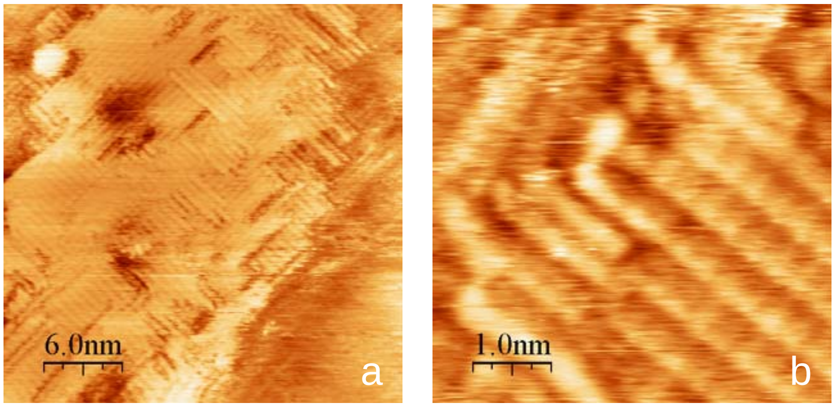

Figure 3.30: *STM images of a few microns thick homoepitaxial diamond films grown at high* C_{me} *on 0-1° misoriented substrate hydrogenated film surface after graphitization.*

The surface monocrystallinity is also confirmed by the AFM measurements. Fig. 3.31 show AFM images of the homoepitaxial films grown under the standard optimal growth conditions described above with C_{me} of 10% grown for 18 h (sample 290806euos) and subsequently hydrogenated for 5 min in the hydrogen plasma as described above. On smaller scale some structure can be seen on hydrogen terminated surface as expected from Refs. [Bob01, Bob03] which could not be observed on the oxidized or as-grown layers demonstrated in Fig. 3.28, where no step-like reconstruction but nano-sized islands have been observed.

This pointed to the hypothesis that the layer is not of monocrystalline nature. The cigar-shaped features that are visible are composed from the C–C dimers, lying in one direction 5.044 Å apart from the next dimers. Also the 2 × 1 reconstruction is observable, with dimers lying on terraces sized in the order of 2 by 2 nm and rotated to each other by 90° which are inherent of the single crystal diamond surface reconstruction. This is shown in Fig. 3.31(b). Thus the AFM imaging confirms the STM data.

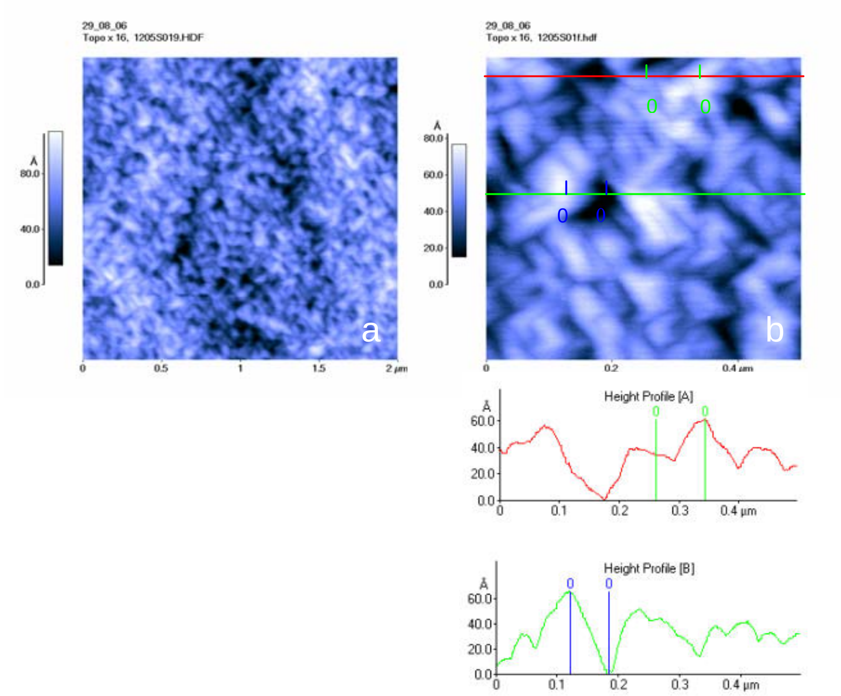

Figure 3.31: *AFM images (a, b) of hydrogenated homoepitaxial diamond films grown at high* C_{me} *on 0-3° misoriented substrates. Also the height profiles can be seen for image (b).*

On contrary as shown previously in the AFM and STM images of as-grown unprocessed layers, near-atomically flat surfaces consist of a few nm sized 'clusters'. These micrographs show that there are no atomic terraces visible. It clearly represents a different structure pattern to ref. [Oku01], where atomically flat surfaces have been achieved for only a few microns thick layers by the step flow growth mode. This evidences a morphological change from the step flow growth to the atomic island growth mode at the growth conditions domain defined in our study. Our results seem to be surprising in terms of the atomic morphology structure of epitaxial growth yielding sub-nm smooth surfaces for a few hundred micrometer thick (270 – 1000 µm) single-crystal films, since the surface roughness is generally known to increase with the film thickness.

This new growth CVD diamond mechanism, different from the step flow growth, leading to flat surfaces free of hillocks and secondary nucleation is one of the important results of this thesis.

3.10. Conclusions

The main aim of Chapter 3 was to prepare and to study the mechanism of growth of homoepitaxial CVD diamond films, aiming finally at preparing free standing single crystal diamond plates. At the same time as this thesis was progressing commercial companies such as Element Six and other research groups have been working on this topic. However, compared to all published results, this thesis came up with the idea of studying of very specific growth mechanism, not covered in the scientific literature, compared to generally accepted step flow growth which leads to atomically or macroscopically stepped surfaces. In this work it has been shown that near –atomically flat layers can be prepared by this technique for very thick films when the growth mechanism is kept stable for several hundreds of hours. The growth mechanism studied and leading to these results was discussed and includes the CH_3 radical addition mechanism and stabilization of the diamond structure. Specifically at high CH_4 concentrations used, which is the specific of this thesis, the carbon add-addition do not proceed only on the step edges but increasing the concentration of CH_3 radicals leads to increased probability of direct add-addition to the surface atoms. In this the growth proceeds at many sites and nano-sized clusters are formed onto the surface which continues growing and percolating together to nearly perfect structure. When the growth is interrupted the surfaces can be imaged on nano-scale confirming this type of the growth mechanism. By using LNT STM imaging we could see that the surface is composed of such nano-clusters which can be eventually etched confirming the perfect crystallinity of the CVD diamond with typical 2×1 reconstructed monocrystalline surface. In the classical picture of growth in the thermodynamical equilibrium, three basic types of the growth mechanism occur: these are the layer-by layer or Frank-van der Merwe type of growth, when the film grows with only the surface layer having fractional coverage at any instant i.e. the "interface width" at the film vacuum interface is one atomic layer. Second mode is the island or Volmer-Weber-type of the growth when the film does not "wet" the substrate since the Bauer condition is not met, and the "interface width" of the growing surface increases with time, describing the enthalpy balance of the film grown on the substrate, i.e. the condition that the surface energy of the growing film is less than or equal to the surface energy of the substrate minus the interfacial energy of the film and substrate is not satisfied.

Finally in the 'layer + island' growth mode or Stranski-Kastranov, after wetting the substrate, the film grows in an island mode and the interface width increases with time. This is not the tendency obtained here where the interface area is constant as at any time and the clusters of the same size appear on the surface. This is due to the fact that the abovementioned main growth modes are based on the thermal equilibrium of the surface with the gas phase. As the CVD diamond growth is strongly non-equilibrium process including the surfactant bonds such as the atomic hydrogen strongly attached to the surface, we believe that such surfactants exchanging at high rate with high concentration of methyl radicals significantly alter surface morphology and enable formation of atomically smooth films. In another words in the growth mode presented here the interfaces volume is kept constant translated to the nano-clusters wetting fully the underneath substrate and/or growing film. Due to lower growth temperature, including limited surface diffusion not allowing migration equilibration and high probability of the radical attachment the nano-clusters are formed at any times and with the same size being present on the surface. Imperfect nano-clusters interaction such as for example additional energetic expenses needed to overcome surface etch pits can lead to macroscopic features in the film. These can be reduced by optimal interactions of the growing surface with the plasma, in terms of optimization of the radical and atomic hydrogen exchange, surface energy (related to the potential energy in the plasma sheet), temperature and the growth rate. Based on this optimization nearly atomically flat surface can be prepared even for large film thickness.

Additionally, we have shown that the substrate surface quality strongly influences the quality of the crystal growth, the surface defects as dislocations and the growth sectors can be imprinted during the growth into the growing films, leading to crystallographic defects, clearly observed by the surface and structural techniques used in this thesis. The Raman spectroscopy mapping revealed that the optimized films are of excellent quality, with narrow FWHM Raman line, better than IIa natural crystals. The best results showed that the FWHM of 1.6 cm^{-1} can be obtained. In case of non perfect substrate the Raman imaging allowed localizing defects developed during the film growth and monitoring the propagation of imprinted detects in the film by monitoring the position of the Raman line (strain), its FWHM and the amplitude. These surface defects could be reduced by a surface pre-treatment which we developed, based on the anisotropic etching in O_2/H_2 plasma before the growth, leaving behind predominantly the (100) surface, which together with optimized α parameter led to the near-atomically flat surfaces. The α parameter optimization including CH_4 and T_S parametric field optimization let growth of films in the best process condition window, which reproducibility was also studied. Finally, a clear difference between the films grown by the “surface cluster” island-growth mechanism compared to the step-flow growth mechanism grown films was observed, where the substrate shape is imprinted to the diamond films. It is believed that this is accused of optimization the growth conditions and the “surface cluster”- island type of growth. The quality of the layers grown in terms of crystallographic defects is studied in Chapter 4.

3.11. References

[Ach05] J. Achard, A. Tallaire, R. Sussmann, F. Silva, A. Gicquel, J. Cryst. Growth **284** (2005), 396.

[Bau05] T. Bauer, M. Schreck, H. Sternschulte, B. Strizker, Diam. Relat. Mater. **14** (2005),266.

[Bob03] K. Bobrov, A. Mayne, G. Comtet, G. Dujardin, L. Hellner, A.Hoffman, Phys. Rev. B **68** (2003), 195416.

[Bob01] K. Bobrov, A. J. Mayne, G. Dujardin, Nature **413** (2001), 616.

[But01] J. E. Buttler, D. G. Godwin, in: Properties, Growth and Applications of Diamond, edited by M. H. Nazareand, A. J. Neves, Inspec/IEE, London, (2001).

[But07] J.E. Butler, I. Oleynik, Phil. Trans. R. Soc. Lond. A (2007).

[Chu92] C. J. Chu, R. H. Hauge, J. L. Margrave, M. P. D’Evelyn, Appl. Phys. Lett. **61** (1992), 1393.

[Cha04] A. Chayahara, Y. Mokuno, Y. Horino, Y. Takasu, H. Kato, H. Yoshikawa, N. Fujimori, Diam. Relat. Mater. **13** (2004), 1954.

[Fie92] J. E. Field, The Properties of Natural and Synthetic Diamond, Academic Press, London, (1992).

[Fre97] M. Frenklach, S. Skokov, J. Phys. Chem. B **101** (1997), 3025.

[Fre91] M. Frenklach, H. Wang, Phys. Rev. B **43** (1991), 1520.

[Har93] S. J. Harris, D. G. Goodwin, J. Phys. Chem. **97** (1993), 23.

[Ham05] M. Hamada, T. Teraji, T. Ito, Jpn. J. Appl. Phys. **44** (2005), L216.

[Hay96] K. Hayashi, S. Yamanaka, H. Okushi, K. Kajimura, Appl. Phys. Lett. 68 (1996), 1220.

[Jan90] G. Janssen, W. Vollenberg, L. J. Giling, W. J. van Enckevort, J. J. D. Schaminee, and M. Seal, Surf. Coat.Technol. 47, 113 (1990).

[Kam83] M. Kamo, Y. Sato, S. Matsumoto, N. Setaka, J. Cryst. Growth 62 (1983), 642.

[Kam88] M. Kamo, H. Yurimoto, Y. Sato, Appl. Surf. Sci. **33/34** (1988), 553.

[Kam92] M. Kamo, T. Ando, Y. Sato, M. Bando, J. Ishikawa, Diam. Relat. Mater. **1** (1992), 104.

[Kiy97] H. Kiyota, E. Matsushima, K. Sato, H. Okushi, T. Ando, J. Tanaka, M. Kamo, Y. Sato, Diam. Relat. Mater. 6, 1753 (1997).

[Kaw95] H. Kawarada, H. Sasaki, A. Sato, Phys. Rev. B **52** (1995), 11351.

[Lee95] N. Lee, A. Badzian, Appl. Phys. Lett. **66** (1995), 2203.

[Lee97] N. Lee, A. Badzian, Diam. Relat. Mater. **6** (1997), 130.

[Mat82] S. Matsumoto, Y. Sato, M. Tsutsumi, N. Setaka, J. Mater. Sci. **17** (1982), 3106.

[Mae95] H. Maeda, K. Ohtsubo, M. Irie, N. Ohya, K. Kusakabe, S. Morooka, J. Mater. Res. **10** (1995), 3115.

[Mun95] P. Munzinger, O. Weis, Diam. Relat. Mater. **4** (1995), 958.

[Meh90] S. P. Mehandru, A. B. Anderson, J. Mater. Res. **5** (1990), 2286.

[Oku01] H. Okushi, Diam. Relat. Mater. **10** (2001), 281.

[Ri02] S. G. Ri, H. Yoshida, S. Yamanaka, H. Watanabe, D. Takeuchi, H. Okushi, J. Cryst. Growth **235** (2002), 300.

[Ri06] S. G. Ri, H. Watanab, M. Ogura, D. Takeuchi, S. Yamasaki, H. Okushi, J. Cryst. Growth **293** (2006), 311–317.

[Spe94] K. E. Spear, M. Frenklash, in: Synthetic Diamond Emerging CVD Science and Technology, edited by K. E. Spear and J. P. Dismukes , John Wiley & Sons, New York (1994).

[Sak99] I. Sakaguchi, M. N. Gamo, K. P. Loh, H. Haneda, T. Ando, J. Appl. Phys. **86** (1999), 1306.

[Shi90] H. Shiomi, K. Tanabe, Y. Nishibayashi, and N. Fujimori, Jpn. J. Appl. Phys. **29** (1990), 34.

[Ste06] H. Sternschulte, T. Bauer, M. Schreck, B. Stritzker, Diam. Relat. Mater. **15** (2006), 542.

[Ste98] W.Steeds, A. Gilmore, et al., Diam. Relat. Mater**. 7**(10) (1998), 1437-1450.

[Tak00] D. Takeuchi, H. Watanabe, S. Yamanaka, H. Okushi, K. Kajimura, Diam. Relat. Mater. **9** (2000), 231.

[Ter02] T. Teraji, S. Mitani, C. Wang, T. Ito, J. Cryst. Growth **235** (2002), 287.

[Ter05] T. Teraji, M. Hamada, H.Wada, M. Yamamoto, K. Arima, T. Ito, Diam. Relat. Mater. **14** (2005), 255.

[Tal04] A. Tallaire, J. Achard, F. Silva, R.S. Sussmann, A. Gicquel, E. Rzepka, Phys. Status Solidi, A Appl. Res. 201 (2004) 2419.

[Tal05a] A. Tallaire, J. Achard, F. Silva, R.S. Sussmann, A. Gicquel, Diam. Relat. Mater. **14** (2005), 249.

[Tal05b] A. Tallaire, J. Achard, F. Silva, A. Gicquel, Phys. Status Solidi, A Appl. Res. **202** (2005), 2059.

[Tam00] H. Tamura, H. Zhou, Y. Hirano, S. Takami, M. Kubo, R. V. Belosludov, A. Miyamoto, A. Imamura, M. N. Gamo, T. Ando, Phys. Rev. B **62** (2000), 16995.

[Tam94] M. A., Tamor, M. P. Everson, J. of Materials Research **9**(7) (1994), 1839-1848.

[Tsu91] T. Tsuno, T. Imai, Y. Nishibayashi, K. Hamada, N. Fujimori, Jpn. J. Appl. Phys. **30** (1991), 1063.

[Tak00] T. Takami, I. Kusunoki, M. N. Gamo, T. Ando, J. Vac. Sci. Technol. B **18** (2000), 1198.

[Tak03] S. Takeuchi, M. Murakawa, K. Komaki, Surf. Coat. Technol. **169/170** (2003), 277.

[Tsu96] T. Tsuno, H. Shiomi, Y. Kumazawa, S. Shikata, S. Akai, Jpn. J. Appl. Phys. **35** (1996), 4724.

[Tsu94] T. Tsuno, T. Tomikawa, S. Shikata, N. Fujimori, J. Appl. Phys. **75** (1994), 1526.

[Tak99] D. Takeuchi, H. Watanabe, S. Yamanaka, H. Okushi, K. Kajimura, phys. stat. sol. (a) **174** (1999), 101.

[Ter04] T. Teraji , T. Ito, J. Cryst. Growth **271** (2004), 409.

[Ter06] T. Teraji, Phys. Stat. Sol. (a) **203** (2006), 13.

[Tak99] T. Takami, K. Suzuki, I. Kusunoki, I. Sakaguchi, M. Nishitani-Gamo, T. Ando, Diam. Relat. Mater. **8** (1999), 701.

[Tsu94] T. Tsuno, T. Tomikawa, S. Shikata, T. Imai, N. FujimAppl.Lett. **64**(5) (1994), 572.

[The00] F. de Theije, J. Schermer, W. J. P. van Enckevort, Diam. Relat. Mater. **9** (2000), 1439.

[Wat99] H. Watanabe, D. Takeuchi, S. Yamanaka, H. Okushi, K. Kajimura, T.Sekiguchi, Diam. Relat. Mater. **8** (1999), 1272.

[Wat00] H. Watanabe, D. Takeuchi, S. Yamanaka, H. Okushi, K. Kajimura, T. Sekiguchi, Diam. Relat. Mater. **9** (2000), 231.

[Wan00] C. L. Wang, M. Irie, T. Ito, Diam. Relat. Mater. **9** (2000), 1650

[Wil93] C. Wild, P. Koidl, W. Muller-Sebert, H. Walcher, R. Kohl, N. Herres, R. Locher, R. Samlenski, R. Brenn, Diam. Relat. Mater. **3** (1993), 158.

[Wil05] B. Willems, L. Nistor, C. Ghica, G. Van Tendeloo, presented at SBDD-X, LUC Belgium, February 2005.

[Wei95] R. A. Weimer, T. P. Thorpe, K. A. Snail, and C. E. Merzbacher, Appl. Phys. Lett. **67** (1995), 1839.

[Yan99] C. S. Yan, Y. K. Vohra, Diam. Relat. Mater. **8**(11) (1999), 2022-2031.

[Yan02] C. S. Yan, Y. K. Vohra, H. K. Mao, R. J. Hemley, Proc. Natl. Acad. Sci. **99** (2002), 12523.

[Yam05] M. Yamamoto, T. Teraji, T. Ito, J. Cryst. Growth **285** (2005), 130.

Chapter 4 Optical and electronic properties of freestanding SCCVD diamond films

4.1. Introduction

Due to its excellent physical and chemical properties CVD diamond advances novel semiconductor materials for high temperature, high power devices. Owing to its chemical stability, high heat conductivity, negative affinity diamond has recently come to be seen as a promising material for many other applications ranging from electronics to bioelectronics. All these applications require the capability of producing semiconductor-grade homoepitaxial diamond films with atomic level surface smoothness (flatness) and substantially no defects or impurities. The defects which are by thermodynamic laws always essentially present in any crystal structure can be studied by defect spectroscopy methods. In general, the electronic structure of a crystal usually prevents electrons from acquiring energies within the forbidden energy band gap. Unless excited by energy such as heat or electromagnetic waves, electrons from the valence band cannot move to a high-energy state above the band gap i.e. to the conduction band. However if a energy source is provided that excite electrons from valence band or from occupied defect states into higher unoccupied states (see also Chapter 2), these transitions can be monitored allowing to characterize gap impurities and defects in diamond with a sensitivity down to sub-ppm means.

The most common characterization techniques are already discussed in Chapter 2. Among them, Raman spectroscopy is used for determining the phase purity and crystallinity of diamond, defect and impurity complexes are usually studied by Photoluminescence (PL) or Cathodoluminescence (CL), Optical absorption, Photocurrent, Electron Paramagnetic Resonance etc. They are labeled by the characteristic energy E_{zpl} of the zero phonon (purely electronic) transition of the center [Cla92] or by their energy position in the gap. As discussed in Chapter 2, the most common defect/impurity complexes found in both bulk and thin film diamond involve nitrogen (substitutional or interstitial) and lattice vacancies. However there are over 300 defects states known for natural and synthetic diamond. The main purpose of this experimental chapter is therefore to characterize the homoepitaxial CVD diamond in terms of presence of defects and their influence on the electrical transport characteristics, which is the most important measure for using these films for electronic applications.

4.2. Gemological characterization

4.2.1. Introduction

The gemological means of characterization, usually intended to evaluate characteristics related to the gemological stone quality, give also important information about the crystal growth and incorporation of impurities. Consequently it is indirectly very useful for growth optimization of crystals for electronic applications.

4.2.2. Experimental

In order to perform the gemological characterization of the CVD diamond layers, the Ib substrates were completely removed by laser cutting followed by polishing of the films so that the CVD samples could be measured without interference of the underlying substrates. The Ib substrates were entirely removed by laser cutting using a Nd:YAG laser and specific procedures of step angle controlled cutting proprietary developed at WTOCD in Lier. Subsequent polishing was performed prior to spectroscopic analysis and color grading. Use was made of the WTOCD-developed 3D-processing tool (SOLID) for lasering diamonds, which is composed by adding 3 degrees of freedom (1 translation and 2 rotations), a measuring device and dedicated software.

All samples were investigated under cross polarizers under diffuse illuminations. The color grade was determined with a Gran colorimeter. Surface luminescence images of the CVD plates were recorded using the DiamondView^{TM}.

The characteristics of samples grown are summarized in the Table 4.1 After the CVD diamond plate were removed from the substrate, they were oxidized in a hot mixture of H_2SO_4 and KNO_3 for 30 minutes and then rinsed in an ultrasonic bath in deionised water to remove hydrogen and graphite from the surface. The samples were studied in the oxidized surface state, unless stated otherwise. For photocurrent spectroscopy technique the gold contacts were evaporated onto the oxidized surface.

4.2.3. Results and discussion

Gran colorimeter grading. Fig. 4.1 shows the optical micrographs of the samples under study as summarized in Table 4.2 together with the gemological color grading. Usually the color determination is done on cut stones i.e. jewelry

Sample	C_{me}, %	p, Torr	P, W	T,°C	Time, h	Remarks	Source gases	Techniques
60405euos	10	180	610	700	114		H_2 (6N); CH_4 (4N)	TOF, PL
290705euos	10	180	550	700	263		H_2 (6N); CH_4 (4N)	EPR, CL, PL
181005euos	10	180	530	700; 740*	143		H_2 (6N); CH_4 (4N)	EPR, CL, PL
250805euos	10	180	550	700 ;750*	163		H_2 (6N); CH_4 (4N)	EPR, CL, PL
100905euos	10	180	570; 710	700; 740*	144+143	two holders	H_2 (6N); CH_4 (4N)	EPR, CL, PL
90805euos	10	180	510	700	166	dirty chamber	H_2 (6N); CH_4 (4N)	EPR, CL, PL
100605euos	10	180	530	700; 800*	161		H_2 (6N); CH_4 (4N)	EPR, CL, PL
80306euos	10	180	600	700	161	3° θ_{mis}	H_2 (7N); CH_4 (4N)	PL, FTPS
100106euos	10	180	570	700	126	6° θ_{mis}	H_2 (7N); CH_4 (4N)	PL
200306euos	10	180	600	700	158		H_2 (7N); CH_4 (4N)	PL, FTPS
101006euos	10	180	650	700; 820*	56	open holder	H_2 (6N); CH_4 (4N)	PL
261105euos	10	180	640	700	136		H_2 (6N); CH_4 (4N)	CL
300506euos	10	180	580	700	159		H_2 (6N); CH_4 (4N)	EPR, CL,PL
60207euos	10	180	600	700	85	open holder	H_2 (7N); CH_4 (6N)	TOF

* Unintentional deposition temperature increase

Table 4.1: *Growth conditions of relevant freestanding SCCVD diamond films studied.*

but not on thin films or plates. Therefore the obtained color might thus be different when a CVD plate would be used for a cut stone. Hence, this gives only a hint of the color and a measure to compare CVD plates.The color of diamond refers to the tone and saturation of color, or the depth of color in a diamond.

It can range from colorless to a yellow or brown hue. A more colorless diamond is rarer and more valuable because it appears white and brighter to the eye. The clarity of diamond is related directly to the concentration of non-diamond carbon and other macroscopic optical defects.

From the data from the Gran colorimeter (diamond grading) in Table 4.2 one can see that for this series of samples the best gemological color is achieved for the samples from shorter runs, i.e. 60405euos, 80306euos, 100106euos, 200306euos, 101006euos. This structural quality was superior and the deposition runs went without any disturbances, constantly keeping and monitoring the plasma/sample growth surface interface without any modification of plasma conditions during the growth. Color E is 2nd on a scale starting with D, representing a perfect colorless or white diamond (see Fig. 4.1). The data in Fig. 4.1 suggest that the structural quality and defect density is negatively influenced when the deposition time is increased, needing specific technical substrate holder modifications.

Sample	Thickness, mm	Color
60405euos	0.27	E
290705euos	0.48	KL
181005euos	0.73	GH
250805euos	0.37	GH
100905euos	0.34	H
90805euos	0.55	G
100605euos	0.40	FG
80306euos	0.39	EF
100106euos	0.32	EF
200306euos	0.40	EF
101006euos	0.35	EF

Table 4.2: *Thickness and color as determined with a Gran colorimeter for a selection of freestanding SCCVD diamond samples.*

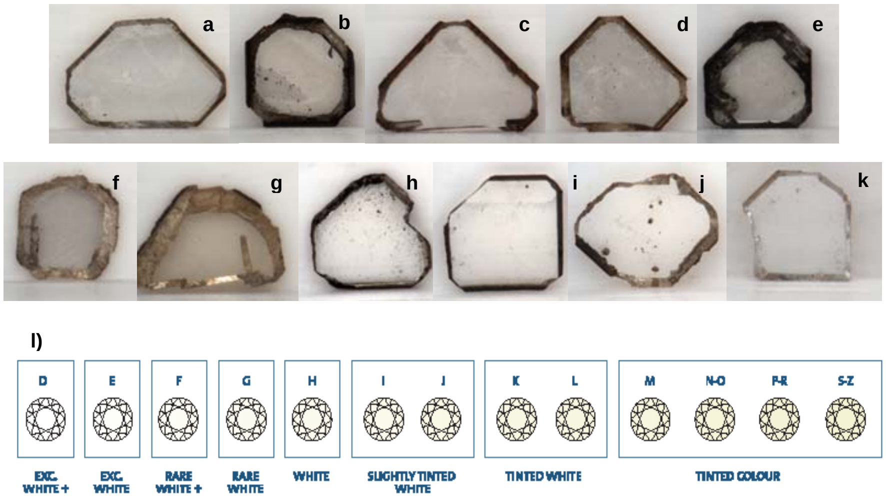

Figure 4.1: *Photomicrographs of freestanding SCCVD diamond plates described in Table 1. a) 60405euos; b) 290705euos; c) 181005euos; d) 250805euos; e) 100905euos; f) 90805euos; g) 100605euos; h) 80306euos; i) 100106euos; j) 200306euos; k) 101006euos. l) The color grade scale (here HRD chart) used for gemological evaluations, which classifies diamond color into 22 grades from letter grade D (colorless) through letter grade Z (fancy color).*

Cross-polarized imaging. Anomalous birefringence, caused by residual internal strain, is a useful feature for the identification of CVD synthetic diamond [Wan03, Mar04]. The results of a study under cross-polarizers are presented in Fig. 4.2. In previous studies [Wan05] such images revealed that the HPHT substrate shape is imprinted into the CVD layer. However based on the images recorded under diffuse illumination the original location of the substrate could not be seen for the 11 plates under study here. This is a remarkable result as often the original substrate location is observed. This suggests that the CVD diamond epilayer is grown by another growth mechanism then the work in ref. [Wan05] where step flow was dominating the growth.

Additionally, samples show cross shaped birefringence features when viewed through the (100) face (Fig. 4.2) as already discussed in Chapter 3, Section 3.8. Those birefringence features i.e. induced changes of the index of refraction, are characteristic for CVD samples and are due to dislocations running all the way through the sample [Mar04]. Small areas of localized strain with relatively higher order interference colors surrounding tiny defect centers were also observed. Anomalous birefringence caused by residual internal strain is also a common feature of natural type IIa diamond. While large variations in intensity have been observed, natural type IIa diamonds generally show much stronger anomalous birefringence than is seen in CVD synthetic diamonds [Mos99]. These are known as banded and “tatami” patterns, that are the predominant strain characteristics of natural type IIa diamonds. The characteristic strain pattern of single crystal CVD synthetic diamond is distinctly different as discussed above. The number and spreading of the cross-shaped features vary among all samples investigated. There is a clear striking distinction between the sample 90805euos and the other samples. This shows a “tatami”-like pattern (see Fig. 4.2 (f)) which is inherent of natural IIa stones where in the first higher interference colors are observed over the complete plate. This pattern looks similar but nevertheless has a different origin.

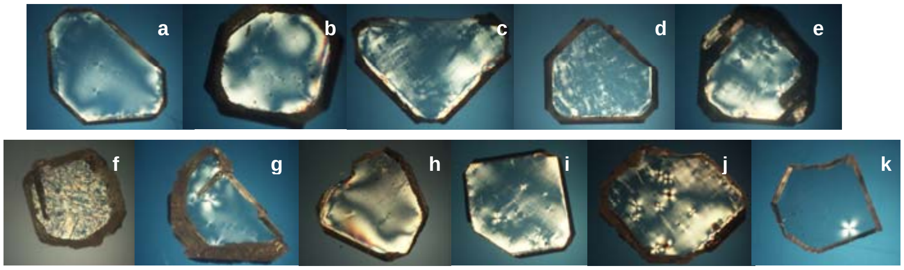

Figure 4.2: *Photomicrographs under crossed-polarizers of SCCVD diamond plates after substrate removal and polishing, showing birefringence features in a cross shape: a) 60405euos; b) 290705euos; c) 181005euos; d) 250805euos; e) 100905euos; f)90805euos; g) 100605euos; h) 80306euos; i) 100106euos; j) 200306euos; k) 101006euos.*

DiamondView^{TM} Imaging. When examined by the DiamondView^{TM} the samples exhibited weak reddish fluorescence as illustrated in Fig.4.3, suggesting the presence of $(N–V)^0$ centers. The blue luminescence is believed to emanate from bundles of dislocations in arrangements not seen in natural diamonds (band A) [Mar04]. Higher purity crystals show only blue luminescence (band A). For some HPHT-grown synthetic type IIa diamonds and many natural IIb diamonds [Shi97, Kin98] blue phosphorescence is very common, but is rarely seen in natural type IIa diamonds. As in the aforementioned birefringence images, the original position of the HPHT-grown synthetic substrate is also not observed which is different to single crystal diamond from other research groups, like those from Element Six. Natural type IIa diamonds in the DiamondView^{TM} typically display characteristic "mosaic" networks of polygonized dislocations or dislocations lying in slip bands [Mar04]. Although the samples examined in this study showed some variation in color and purity due to deposition conditions, it is clear that deposition of non-diamond carbon during crystal growth at moderate growth rates was minimized, leading to the formation of near-colorless gem-quality crystals. The SCCVD diamonds showed subtle but distinct differences in gemological properties from commercial and other research group samples [Wan03, Mar04].

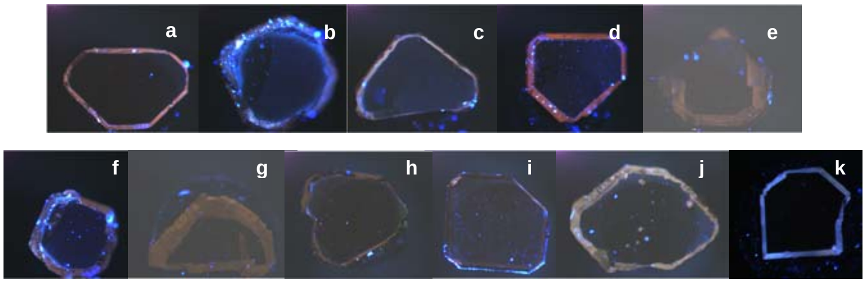

Figure 4.3: *DiamondView™ images of SCCVD diamond plates after substrate removal and polishing showing reddish and blue luminescence: a) 60405euos; b) 290705euos; c) 181005euos; d) 250805euos; e) 100905euos; f) 90805euos; g) 100605euos; h) 80306euos; i) 100106euos; j) 200306euos; k) 101006euos.*

4.2. Photocurrent characterization

4.2.1. Introduction

Photocurrent spectroscopy is a powerful tool allowing detection and characterization of defect-induced localized electronic levels in the energy gap of the nominally undoped diamond that has dark current resistivity and a relatively high mobility-lifetime product [Ros99, Rem05]. To overcome the problem of low photocurrent signals in the sub-band gap region and especially in the IR region, Fourier transform photocurrent spectroscopy (FTPS) has been introduced

[Van02, Van03] This experimental setup, also built at IMO, University of Hasselt, has been discussed in Chapter 2.

4.2.2. Experimental

In photocurrent measurements a constant voltage is applied on two ohmic contacts and the photocurrent spectrum is evaluated as a function of the incident photon energy. In the dual beam photoconductivity experiments (DBP) [Lee89, Rem07], an auxiliary UV lamp (deuterium or xenon lamp) provides a constant DC photocurrent. The photoionization spectrum is scanned by the AC photocurrent which is superimposed on the DC photocurrent. The AC photocurrent measured by a lock-in amplifier probes the photoionization spectrum in the diamond band gap region in the near UV, visible and near IR spectral regions (below 5.5 eV) in the standard setup. The xenon or halogen lamps, the diffraction grating and the mechanical chopper provide the periodically modulated quazi-monochromatic light. The AC photocurrent is linear with light intensity in DBP, because the UV bias light removes the spectral dependency of the mobility-lifetime product by keeping the occupation of gap states constant. Additionally, UV-induced photoconductivity decreases the RC constant of the electrical circuit which is important in otherwise highly resistive samples. As discussed in Chapter 2, for the Fourier Transform Infrared (FTIR) absorption measurements a Nexus of ThermoNicolet was used. The spectra were recorded in the 7000–400 cm^{-1} range.

4.2.3. Results and discussion

FTIR. First, standard FTIR spectroscopy was used to measure optical transmission in a wide spectral range before studying the photcurrent. It revealed that the analyzed CVD samples are high quality high purity diamonds (Fig. 4.4) with low defect density. Based on the FTIR there are no traces of nitrogen-related centers visible in the one-phonon region of 1500 to 500 cm^{-1} within the limits of the FTIR sensitivity. Further on, in none of them, the H-related absorptions 3123 or 3323 cm^{-1} were observed [Mar04].

The measured free standing single crystal CVD diamond layers are of high optical quality, and can be labeled as type IIa diamonds as shown as a typical example for the sample 80306euos in Fig 4.5.

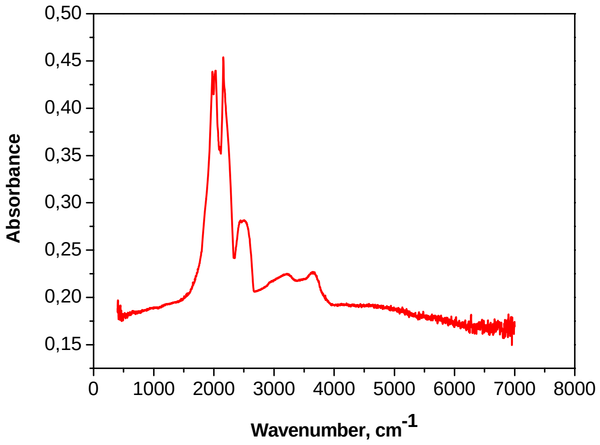

Figure 4.4: *FTIR optical absorption spectrum of a SCCVD diamond sample 300505euos showing the high purity nature of the layer.*

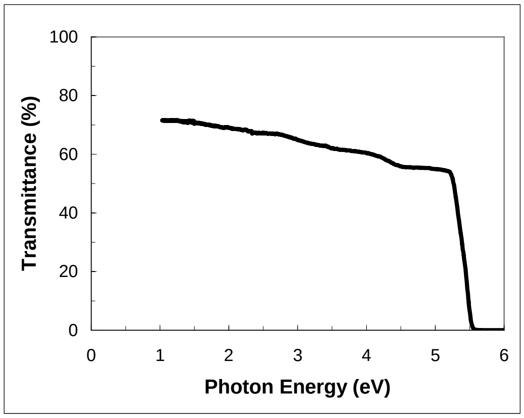

Figure 4.5: *Optical transmittance spectra of a polished, single crystal type IIa CVD diamond about 0.4 mm thick. Sample 80306euos.*

The diamond samples are optically transparent up to 5.5 eV in the deep UV spectral region, were the transmittance drops due to the optical absorption gap, i.e. (indirect electron transitions from valence to conduction band. Below the fundamental optical gap small optical losses appear, however it is difficult to distinguish the small optical absorption from surface related scattering due to imperfect surface polishing.

Photocurrent measurements. The sub-band gap photocurrent is directly proportional to the concentration of the defect-induced localized states in the band gap, their photoionization cross section as well as the mobility-lifetime product that characterize the electron transport properties [Roh96]. In these measurements, the mobility-lifetime product is practically spectrally independent and the measured data can be recalculated to the optical absorption, giving direct evidence of the presence of defects. In general, the measured photocurrent is related to the optical absorption coefficient $\alpha(E)$ by using the equation:

$$I_{Ph} \sim e\,(1-R)\,N_{ph}\,\mu\tau\,(1-\exp(-\alpha d))F \tag{4.1}$$

In this formula e is the electric charge and F is the electric field applied. N_{ph} is the number of photons, μ is the carrier mobility, τ is the lifetime, d is the thickness of the sample, R is the constant. The full derivation of the expression the reader can find in the work of [Bub92]. If one wants to obtain $\alpha(E)$ and further on the photoionization cross-section $\sigma(E)$, $\alpha(E) = N_i f(E)\,\sigma(E)$; where $N_i f(E)$ is the number of occupied impurities one has to simplify the experimental measurement conditions by such a way that in Eq. (4.1) all parameters can be set independently on the energy of the incident light or they have to be known. Example is the DBP-FTPS where the mobility-lifetime product is kept constant by using a strong pumping beam of intensity higher than that of the monochromatic probing beam.

Another important aspect is to set the measured spectra on absolute scale. The intrinsic optical absorption is related to the concentration of states at the valence band maximum, conduction band minimum and the optical matrix elements, from the known optical absorption at the optical gap 5.5 eV and related to the indirect electronic transitions from valence band into the conduction band. Therefore the spectra can be set on the absolute scale. This optical absorption coefficient near the optical gap 5.5 eV should be approximately the same for all high optical quality single crystal diamond samples. Thus, when knowing this values of the optical absorption coefficient at certain energy, one can directly fit the sub-gap absorption calculated from the photocurrent in near IR, visible light and near UV region by putting the photocurrent spectrum onto the “absolute scale” using the optical absorption coefficient calculated from the transmittance spectra just at the optical gap at 5.5 eV, see Fig.4.6.

The sample 200306euos shown in Fig.4.6 exhibits the indirect optical absorption gap near 5.5 eV and the defect-induced optical absorption in the energy gap region. The photoionization shows an onset at photon energy of about 2.2 eV, which indicates the photoionization of single substitutional nitrogen [Ros99]. From the previous studies that compared the optical absorption coefficient in diamond with the total content of the substitutional neutral nitrogen as measured by electron paramagnetic resonance (EPR) follows that the residual nitrogen concentration for the sample 200306euos in Fig.4.6 is in the order of 1 ppm. Thus, relatively high residual nitrogen concentration is observed in this nominally undoped diamond crystal. This value is depending on the purity of the gases used and on the residual vacuum before the growth.

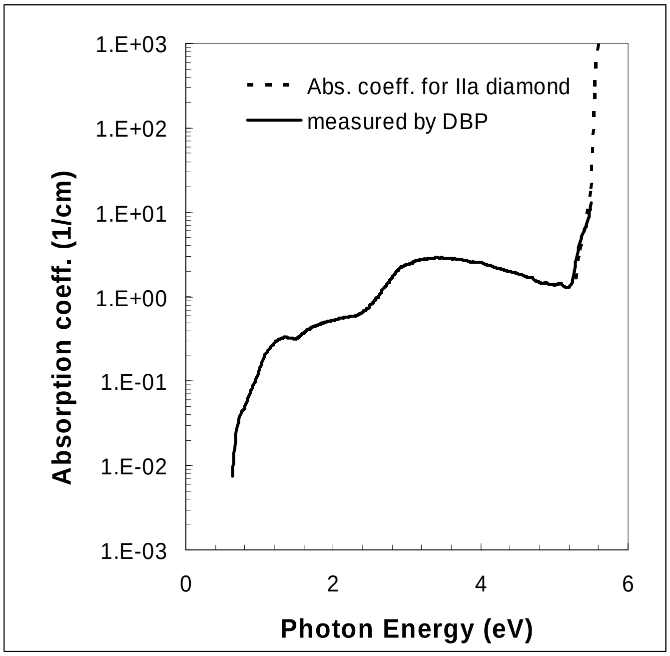

Figure 4.6: *The typical optical absorption coefficient of single crystal diamond sample 200306euos measured by using quazi-monochromatic light above 1.55eV (PC) and AMFTPS below 1.55 eV. The photoionization cross section spectrum was put on an absolute scale using the absorption coeficient. calculated from transimittance spectra at 5.5 eV*

Currently, improved gas purity and new deposition conditions are being introduced leading to the reduction of the nitrogen contamination during CVD diamond growth. Recently, reports on the growth of single crystal CVD diamonds with very low nitrogen concentration below 1 ppb have been published based on the EPR data was reported [Isb5]. However when measuring such samples by FTPS the measured values are higher. It is assumed N can exist in CVD diamond in the positively charged state, which is not detected by EPR.

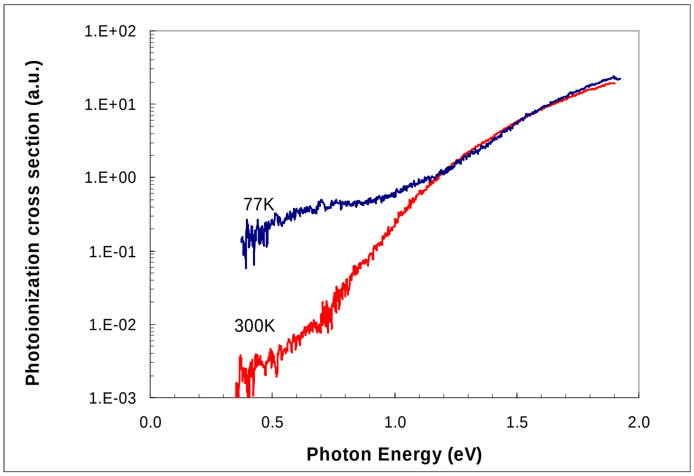

Figure 4.7: *The relative values of the photoionization cross section of the single crystal CVD diamond sample 200306euos in the IR region measured by AMFTPS at room and liquid nitrogen temperature normalized at 1.5eV to show the increased photosensitivity below 1.2 eV.*

Additionally, the photocurrent spectra shown in Fig. 4.6 and 4.7 point towards another set of defect states that appear in the near IR region below the onset of the nitrogen related photoionization. These defects are called D_x states appearing at ca. 1.2 eV above the valence gap and have been already observed in as grown or hydrogenated polycrystalline CVD diamond in which it diminished after oxidation treatment [Ros99]. This defect is clearly present in the sample 200306euos. For the first time the D_x defect in single crystal CVD diamond with a fully oxidized surface, excluding this defect to be surface related. It is speculated that the D_x defect may be the hydrogen-related defect H1 as this defect could be seen as discussed further in the EPR study. Further studies are necessary.

Fig. 4.7 shows that the photoionization spectrum at energies below 1.2 eV is very temperature sensitive. Additionally, the comparison of Fig. 4.6 and Fig. 4.7 suggests that at low energy the B-acceptor spectrum appears with the photionisation onset at about 0.36 eV. As the occupation of the B-acceptor level is temperature sensitive, this leads to the discussed pronounced temperature dependence of the IR spectra. Thus, it is proposed that at low temperatures the photoconductivity is due to photo excitation from the valence band into boron states above the valence band at 0.36 eV. Upon cooling the sample, the quasi-Fermi level for holes shifts to valence band and the free hole-dominated photocurrent increases. The calibration of the photocurrent spectra on the UV absorption suggests that the concentration of B in our sample is about 1 ppb. This value agrees well with data based on CL measurements carried out at the University of Erlangen presented further in this section.

4.3. Electron paramagnetic resonance characterization

4.3.1. Introduction

EPR is a quantitative technique used to determine the concentration of paramagnetic defects grown into the CVD diamond layers. Predominantly two main defects are detected the H1 and N_S^0 defects. It has been shown that the single substitutional nitrogen centre (N_S^0) concentration (EPR paramagnetic centre called P1, resonance at $g = 2.0024$) can be determined from the line width from EPR [Wyk97]. Since continuous wave EPR spectra are recorded using field modulation (resulting in a spectrum which approximates the first derivative of the EPR line shape), double integration is required to determine the EPR intensity and hence ultimately the defect concentration. To minimize the errors associated with double integration, base line correction, finite limits of integration, etc., especially in cases where overlapping EPR spectra are detected, a spectral fitting method (using a simple algorithm) was employed to determine the integrated intensity of the EPR centers present in the samples. This fitting entailed the experimental spectra with simulated spectra of the defects present in the sample, determining the integrated intensity of each from the simulation.

Experimentally it is observed that neither a Lorentzian nor Gaussian line shape provided a good fit to the experimental EPR spectra. A Tsallis function was used to produce the simulated spectra [How03]. Furthermore, in the case of low nitrogen concentrations, it is often necessary to use modulation amplitudes approaching or exceeding the line width of the EPR signals to achieve a good signal/noise ratio enabling accurate concentration determination within a reasonable time frame used. Hence pseudo-modulation [Hyd90] was employed, with the Tsallis line shape in order to produce a good fit to the recorded EPR spectra. Using this method the integrated intensity of the EPR spectra for each defect present could be determined with a reproducibility of better than ±10%. This is the dominant error in the relative N_S^0 concentration determinations. Since the uncertainty in the reference sample concentration is also of the order of 5%, the uncertainty in absolute N_S^0 concentrations is between 10 – 20 %. It should be remembered that EPR produces an average concentration for the bulk sample. In many cases, the concentrations were below the detection limit of the equipment and hence only an upper limit could be estimated for the concentration. N_S^0 is the dominant paramagnetic defect in the samples of this work.

4.3.2. Experimental

The substitutional nitrogen concentration was determined by Electron Paramagnetic Resonance (EPR) measurements using a 4119HS cylindrical cavity on an X-band Bruker EMX-E spectrometer in collaboration with the University of Warrick. All measurements were made at room temperature and concentrations were determined by comparison to a reference sample: single growth sector HPHT synthetic diamond of 2 mg in mass and doped with 270 ppm of single substitutional nitrogen, as determined by infrared absorption and combustion. The integrated intensity of the EPR signal from the reference sample was compared to the signals obtained for the sample in question and a concentration was determined.

4.3.3. Results and discussion

$(N–V)^-$ concentration. For the determination of the $(N–V)^-$ concentration the EPR technique was working at the limits of detectivity which influences the precision of N-determination (see above). However the PL spectra (see further in this section Fig. 4.14) suggest that mainly the neutral $(N–V)^0$ of the two different charge states of N-V was present in the films. Hence so far the low $(N–V)^0$ concentrations could not be detected quantitavelly. The detailed analysis of the EPR spectra line width confirms that the signal is not originating from the entire sample and the nitrogen-vacancy can not be therefore considered as being equally distributed as the signal does not have sufficient strength for such a line width. Fig. 4.8 shows a fit to the spectrum noise depicting a maximum concentration possible for this sample. The concentration would be much smaller but the sample is too small to generate a large enough signal for the system to detect.

N-concentration. It is known that the N concentration can significantly vary in different growth sectors in the substrate, which has been shown in Chapter 3. This can be also translated to the sector growth of the free standing CVD diamond. N can exist either in negatively charged configuration (P1), neutral configuration (N_S^0) or being positively charged (N_x). In Fig. 4.8, the EPR spectrum of the single crystalline CVD homoepitaxial diamond 100905euos film taken with a magnetic field along the [100] axis at room temperature is shown. The small signal at the central part of the magnetic field in Fig. 4.8 is the central hyperfine line of substitutional nitrogen (N_S^0). For the majority of the samples that did not appear to have any other sectors as substrates remainders there was such a small number of N_S^0 that it is was not possible to detect it by EPR. Likewise, for other defects as their concentrations were below the system detection limits. However the P1 defect was well detectable, an integration of the spectra yielded concentrations of less than 1 ppm. The measured concentrations of P1 defect is shown in Table 4.3. Additional EPR signals are observed at $g=2.0028\pm0.0002$ which agrees with the reported g-value of the hydrogen-related defects labeled H1 in polycrystalline CVD diamond [Zho96, Tal98] discussed below. In the CVD homoepitaxial diamond films the H1 defect has been shown to be a bulk defect [Miz04, Miz06].

Sample	N_S^0, ppm
300605euos	0.58
290705euos	0.45
181005euos	1.66*
250805euos	0.39
100905euos	0.15
90805euos	0.08
100605euos	0.31

*with substrate remainders

Table 4.3: *Samples studied by EPR with the total* N_S^0 *concentration.*

H1 defect. This above discussed defect structure can be observed in the centre of the spectra in Fig. 4.9. It is proposed that the H1 center is $(H\text{-}V)^0$ in which, among four carbon dangling bonds around the vacancy, one bonding to hydrogen and two bondings together leave one dangling bond where the unpaired electron localizes [Zho96].

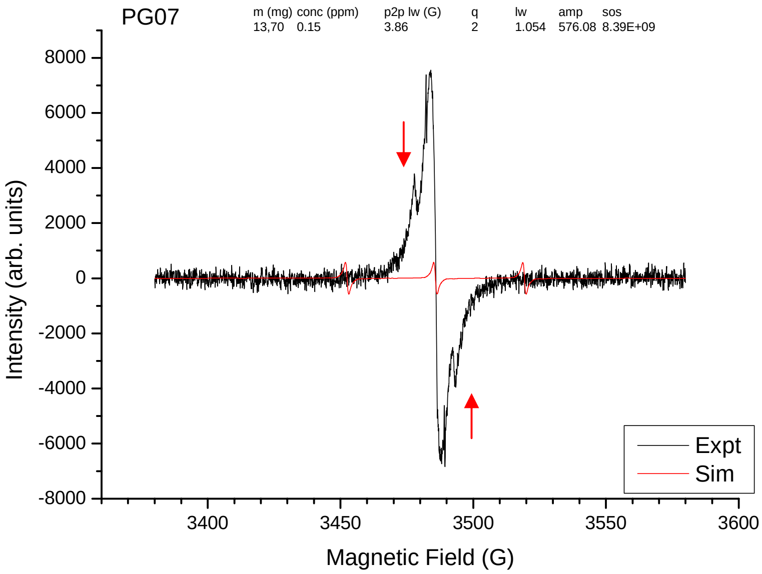

Figure 4.8: *The EPR spectrum of sample 100905euos and its fit with the magnetic field along the [100] axis at room temperature. The microwave frequency is 9.74 GHz.* N_S^0 *is the central hyperfine line of substitutional nitrogen. The arrowed weak satellites are the H1 defect.*

From the spectra in Fig. 4.9 a mathematical modeling was carried out to subtract the measurement noise and to determine as precise as possible the concentration of the H1 for this sample. A power sweep carried out on this sample and shown in Fig. 4.9 shows that the satellites were less easily saturated by the microwave power than the central line. The satellites, which arise from the normally forbidden electron-nuclear spin flip transitions due to dipole–dipole interaction between the unpaired electron and hydrogen, reveal that the unpaired electron is accompanied by a nearby hydrogen. Thus, the observed EPR spectrum is arising from a type of hydrogen-related defect similar to the H1 center.

In some of the samples listed in Table 4.3, particularly, samples 250805euos and 100905euos, there appeared to be a significant concentration of H1 defect, usually found in polycrystalline CVD material and present at dislocation grain boundaries [Zho96, Tal98].

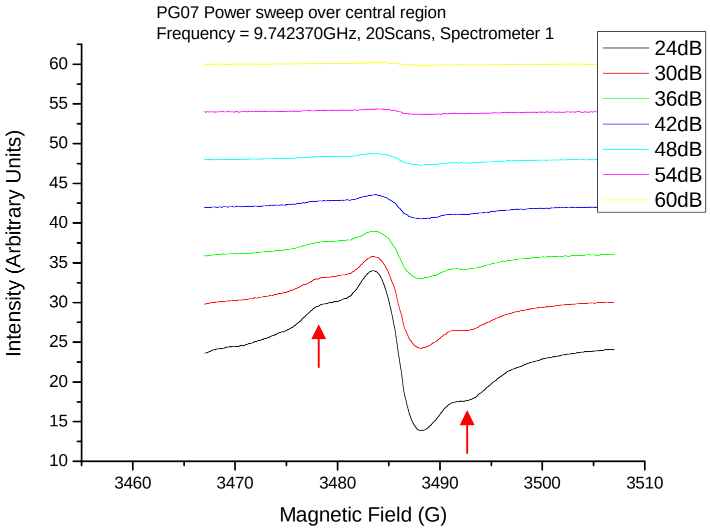

Figure 4.9: *The EPR spectrum of sample 100905euos showing a power sweep over the* N_S^0 *central region. The satellites of the P1 peak are the H1 defect.*

4.4. Cathodo- and photoluminescence characterization

4.4.1. Introduction

The presence and distribution of luminescent active point defects in diamond layers can conveniently be determined from cathodoluminescence (CL) and photoluminescence (PL) analyses [Dav79, Col92] outlined in Chapter 2. In the CL experiments, the penetration depth of the impinging electrons of typically 8 keV for the research described in this thesis is limited to less then a few microns. This makes CL a near-surface technique and well-suited to investigate for example the properties of homoepitaxial diamond layers while excluding any signal from the underlying diamond seed crystal. Because the decay time of many optical centers in diamond is very short (typically 10-50 ns) [Zai01], the same center can be excited many times per second. This results in an intense emission and makes CL a very sensitive technique able to identify very small impurity concentrations (a limit of ~ 1 ppb, i.e about 10^{14} cm^{-3} range compared to the 10^{18} cm^{-3} range for IR spectroscopy).The direct recombination of the electrons with the holes in the valence band results in approximately 5.5 eV intrinsic edge emission in very pure diamonds [Dea64]. Alternatively, the excited electrons can recombine via impurity induced states in the forbidden energy gap, which for most centers is accompanied by a characteristic luminescence [Dav79, Col92]. Related to centers with emission in the visible range, which allows for the direct observation of the spatial distribution of the impurities. In high quality semiconductor and insulating crystals, a free-exciton, i.e. a bound electron-hole (neutral quasi-particle), luminescence often can be measured. Free-exciton (FE) and bound-exciton (BE) recombination radiation is usually studied for characterization of the crystal quality. However, the ratio of the FE and BE can give exact concentration of the impurity to which the exciton is bound [Kaw93]. Examples in diamond are B or P.

Contrary to using an electron beam in CL, in case of PL a photon beam (light) can be used to promote electron excitation which can be quenched by radiative recombination. After a short time the center relaxes to the ground state, emitting light with photon energy below that of the exciting light. In case of a coherent light source for the PL excitation such as a laser, generally also the Raman line (see Chapter 2) can be detected and used for probing the crystal quality at the same time as PL spectrum. Therefore, the Raman signal is very useful to normalize the PL spectra as obtained from different samples with respect to each other, which allows for a semi-quantitative comparison. In the work in this thesis the presence of luminescent point defects in the diamond layers was analyzed by photoluminescence spectroscopy, whereas Cathodoluminescence was utilized to determine mainly the residual boron content in the freestanding SCCVD layers.

4.4.2. Experimental

Cathodoluminescence (CL) was measured in collaboration with the University of Erlangen. The CL spectra was excited at 63 K, using a custom-built electron gun operating at 8 keV with a beam current of approximately 800 nÅ focused to a spot of approximately 200 µm in diameter. CL spectra were acquired from 230 to 600 nm using a 0.25 m Monochromator fitted with a 1200 groove/mm grating blazed at 500 nm. The detector was an EMI 9558Q photomultiplier in counting mode, and the spectra have not been corrected for the response of the system. The resolution was 0.33 nm.

Photoluminescence (PL) was measured in collaboration with HRD Research at a temperature of 77 K by using a cryogenic stage of Oxford Instruments in combination with a Jobin Yvon spectrometer with the 514.5 nm excitation line of an argon-ion laser, the 325.0 nm excitation line of a HeCd, and the 632 nm excitation line of a HeNe laser. The experimental conditions were kept exactly the same for each sample, in order to allow semi-quantitative analyses. Each sample was measured on two arbitrary spots on each side of the sample. The samples are measured on two spots to take into account spatial inhomogeneities. The 514.5 nm and 632 nm excitation photoluminescence spectra were recorded by using a 600 grooves/mm grating element, the 325.0 nm excitation photoluminescence spectra were recorded by using the 2400 grooves/mm grating element.

4.4.3. Results and discussions

4.4.3.1. Cathodoluminescence results

The free-exciton (FE)-related emissions of the diamond samples were measured at 63K with a spectral resolution of 3.3Å as shown in Fig. 4.10. The exciton peaks can be easily identified from the work of Dean *et al.* on natural and synthetic crystals [Dea65], the Data Handbook of Zaitsev [Zai01], the review chapter of Sauer [Sau04]. Because of the indirect gap of diamond, the FE are associated with one or several phonons [Dea65, Zai01, Sau04]. Specifically, the peaks at 235 nm (FE^{TO}), 242 nm (FE^{TO+O}), 233 nm (FE^{TA}), and 238 nm (BE^{TO}) are due to free-exciton recombination radiation with transverse optical (TO) phonon, a phonon replica of FE^{TO}, free exciton with absorption of acoustic phonon, and boron binding exciton with TO phonon, respectively. The observed lines are discussed in detail in Fig. 4.10 for the samples listed in Table 4.2.

Boron concentration determination. Some of the samples such as the samples 290705euos and 181005euos show a bound exciton to boron. This data is thus a direct confirmation of FTPS results where we could see boron in minor quantities to be present in some CVD diamond films. To determine the B concentration in the range of boron incorporation ~ [B] 10^{15} - 10^{18} cm^{-3}, the ratio of the intensity of the BE^{TO} peak to that of the FE^{TO} peak can be used [Kaw93, Kaw93b, Rua92].

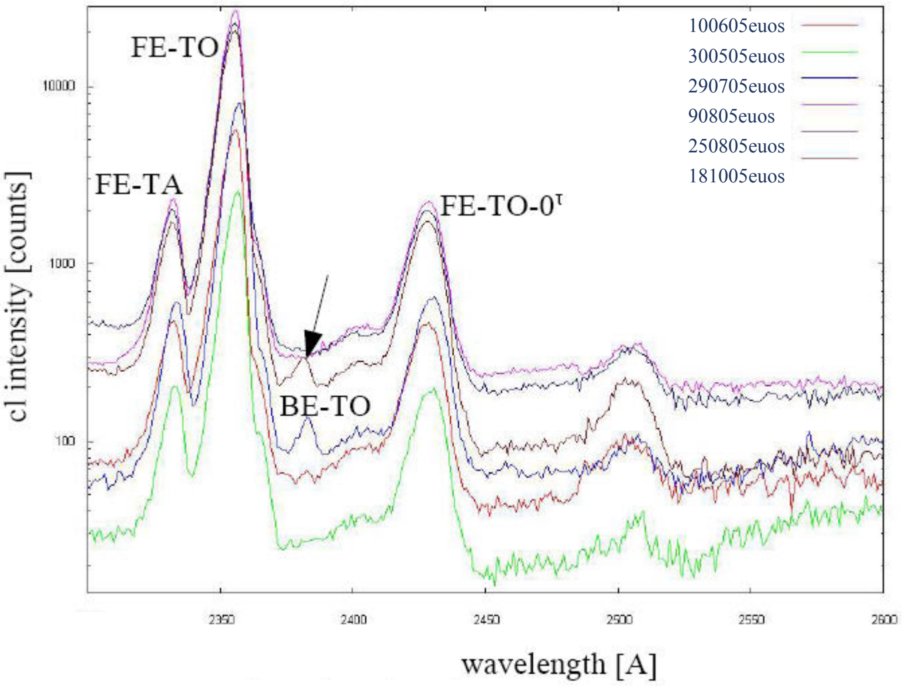

Figure 4.10: *Excitonic emission at 63K of the six diamond samples described in Table 4.2.*

Using the calibration shown in [Kaw93] the ratio of the amplitudes of the BE and FE at 77 K is a function of the boron content as shown in Fig.4.11. The data points can be fitted by Formula 1.

$$\frac{BE}{FE} = (21{,}19 \pm 0{,}39) \cdot (1 - e^{\frac{boron\,conc. \cdot 10^{17}\,cm^{-3}}{(26{,}99 \pm 1{,}58)}}). \tag{1}$$

As it can bee seen from Figure 4.11, the ratio saturates at high boron concentrations. However, the calibration can still be used at lower concentrations where the function is linear. Measurements done at still lower temperatures improve the sensitivity of the method, for example measurement at 63K increases this ratio by a factor of 1.68 ± 0.14.

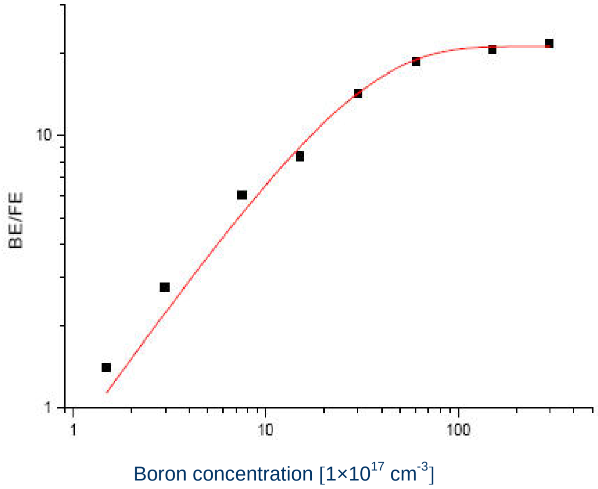

Figure 4.11: *BE/FE amplitude ratio as a function of boron content. Temperature was 77K. The fitted function is shown in red.*

The B-concentrations in our sample listed in the table 4.4 were determined by measuring the same sample at 63K and 77K. The calculated boron concentrations for two samples show boron concentrations in the order of 3 ppb whereas all the other samples from the measured set contain less than 0.6 ppb of boron, which is the system's lower detection limit due to photon statistics in all samples. Thus the FTPS data are in good agreement with the CL data. Contamination by boron in the 10^{16} cm^{-3} range of homoepitaxial diamond films is usual [Kas04]. The origin of boron in the CVD films is somehow controversial as the growth chamber was never exposed to any B-doping as repeated many times in literature [Kas04]. This proves that the B incorporation from any possible sources remains easy under the present deposition conditions. Although it might be unavoidable in most of the deposition conditions [Kas04], it can be controlled at least down to the 10^{14} to 10^{16} cm^{-3} ranges. There have been several speculations about the B origin in the growth chamber.

The HPHT substrate can contain ppm levels of B which can get into the plasma when the unpolished sample edges are exposed to atomic hydrogen. Other possible sources are gas contamination or contamination of B in alloys from which the chamber is made of and which come into the contact with the plasma. Also B is also used in silica or quartz widows used as MW windows in the reactor.

Sample	B, ppb
300605euos	-
290705euos	3
181005euos	3
250805euos	-
100905euos	-
60405euos	-
90805euos	-
100605euos	-

Table 4.4: *Samples studied by CL with the total B concentration (detection limit <0.6ppm).*

Additionally, the free and bound exciton peaks widen for an increasing (from 1 to 3) number of phonons for the free and for the boron-bound exciton regions. The FWHMs of the exciton peaks compare favorably to the value obtained for the best homoepitaxial films: 5 meV for the FE^{TO} [Oku01, Wat00]. When high-resolution detection is not used [Sau04] FWHMs of 30 meV are more usual [Sau04]. From the low FWHM of the free exciton peaks values [Sau04], we conclude that our films are of good quality.

Presence of other defects. CL spectra have been taken in a wide spectral range. Fig. 4.12 shows a typical CL spectrum of freestanding homoepitaxial CVD diamond film 90805euos measured at 63 K in a wider wavelength range. There is a set of visible lines usually present in all the spectra. The narrow peaks are in principle associated with point defects. In the presented CL spectrum, the luminescence bands present from 270 to 320 nm originate from 5RL and 2BD defects. The set of vibronic levels and the phonon replicas of the 5 RL defect (zero phonon line at 272 nm), are at the wavelengths of 278 nm, 283 nm and 287 nm [Zai01]. Also other peaks are detected, specifically the 276 nm and 290 nm lines of the 2BD defect [Kan04].

The origin of 5RL and 2BD bands are interstitial carbon atoms, and boron-related defects containing interstitial atoms including a strain component, respectively [Zai01]. Further on the 303 nm line might originate from the 272 nm ZPL (5RL) associated with two phonons. As the intensities of its components follow those of the FE excitons, the 5 RL defect is unambiguously present in the film. The interstitial carbon defect (5RL) might originate [Zai01] from an overfeeding of the film with C atoms. The result related to the interstitial carbon with additional strain component is in very good agreement with the Raman data, presented in Chapter 3.

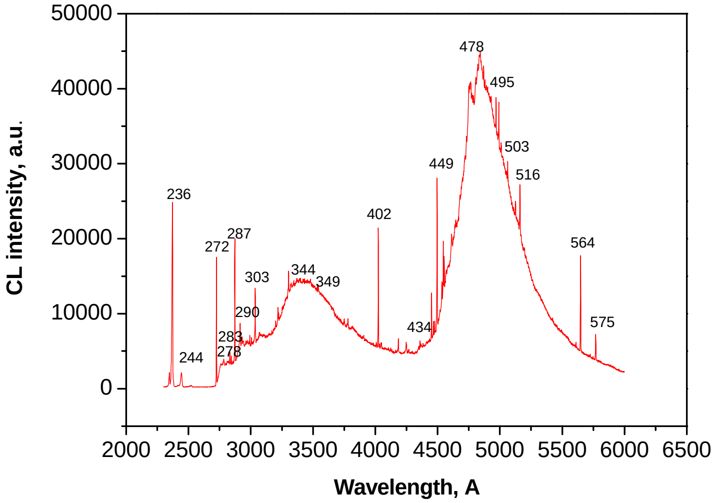

Figure 4.12: *Wide-range typical CL spectrum of the CVD homoepitaxial diamond film 90805euos measured at 63 K.*

At lower energies, the 575 nm and 564 nm are ascribed to the most abundant defects in diamond: a neutral $(N–V)^0$ complex defect and one substitutional nitrogen respectively [Zai01], while the 503 nm peak with its specific phonon replica (narrow bands and the 533 nm peak) is associated with the H3 centre (N–V–N). The 495 nm peak is a specific defect characteristic to CVD diamond films [Sau04]. Therefore, there is some contamination of the films by nitrogen although it is expected to be rather low because of the low intensity of $(N\text{-}V)^0$ peaks relative to that of the FE^{TO}. In addition we observed defect lines at 402 nm, 449 nm, 516 nm whose origin is not identified were observed.

Complementary to sharp lines discussed above rather broad bands are present in the diamond films, originating from extended defects. An example of such defect is a well-known 434 nm (A band), which is associated with dislocations and/or planar defects [Oku01]. Also a 539 nm band was found which is known to appear in homoepitaxial [Kaw93] diamond films. It is ascribed to donor (nitrogen) acceptor (boron) pairs decorating dislocations [Rua92, Sau04].

Additionally 478 nm and 349 nm broad bands are seen which were previously found in the CL spectra of slightly boron doped homoepitaxial diamond films [Kas04]. These two bands are associated with boron. The 344 nm and 270 nm bands were also found in the CL spectra of various boron doped diamond samples. However, their physical origin remains unclear [Law95, Sau04].

4.4.3.2. Photoluminescence results

As discussed above, the electron beam can be replaced by a photoexcitation which can be used to study selectively defects appearing in the band gap. When 514 nm laser excitation was employed, besides a very sharp well-defined diamond Raman peak at 1332 cm^{-1}, the second–order Raman peak at 590 nm is clearly visible and its intensity is at least twice that of the background signal. This is characteristic of high-diamond quality suggesting that no degradation of the layers has occurred despite high methane concentrations used during the CVD growth.

N-V, Si-V, N-doublet centers. The PL emission spectra were obtained at liquid nitrogen temperature for all the samples summarised in Table 4.2. Several laser excitations were used to obtain maximum sensitivity over various energy regions. The 514.5 nm laser excitation is more sensitive to detecting the 637 nm $(N\text{-}V)^-$ defect, and 632.8 nm excitation is ideal for detecting traces of the Si impurity (i.e. Si-V centre at 737 nm). One can see a weak luminescence emission from the $(N\text{-}V)^0$ centre at 575 nm, weak N-doublet related emission at 563 nm, and the (Si-V) centre at 737 nm, which could be detected for the samples grown typically at 700°C (see Table 4.2 and Fig.4.13 (b)). The centre found at 534 nm relates to a nitrogen-containing defect, possibly to a (N-V) complex. The presence of the (Si -V) band is probably a consequence of quarts reactor window etching or due to an aggressive O_2 plasma etching of the Mo holder having trace amounts of Si. The presence of the 575 $(N\text{-}V)^0$ nm line in not intentionally doped samples, as seen in Fig.4.13 (b) can be due to the residual nitrogen present in the vessel after pumping (background vacuum < 10^{-7} Torr) which is further present in the gas phase or related to a reactor leak rate, which for our CVD chamber was about 10^{-8} mbar/s for the CVD chamber used.

$(N–V)^0$ complex. The spectra given in Fig. 4.13 (a, b) show a difference in the luminescence features for the samples grown at 700°C and 800°C. The two spectra were normalized in order to have identical height of the diamond Raman peak. For the sample grown at 800°C and using an open holder besides the 575 nm peak due to neutral the $(N\text{–}V)^0$ complex the 637 nm zero-phonon line, due to single substitutional nitrogen associated with a vacancy in the negative $(N\text{–}V)^-$ charge state can be observed. This is not observed in any of the freestanding films grown at 700°C, whereas the GR1 (741 nm) which is a general radiation defect associated with neutral vacancies is not present anymore at an increased temperature to 800°C. Therefore there is a strong correlation between the defect structures and the deposition temperature.

Another observation is that the spectra of all the freestanding samples described in Table 4.2 normalized to the Raman line in order to have a semi-quantitative estimation, show that the samples grown using a higher purity hydrogen H_2 (7N) have a considerably less intensity of nitrogen associated peaks.

GR1 defect. In freestanding CVD plates also GR1 lines (741-744 nm) are clearly observed, associated with neutral vacancies as mentioned above. The 741 nm (GR1) is always accompanied with 737 nm (Si-V). Because the growth takes place at 700 °C, where vacancies are mobile, it is surprising that they are observed in the plates. In addition, very weak emissions of at 596 nm, 683 nm, and 600 – 610 nm were occasionally observed in the freestanding samples the origin of which remains unclear.

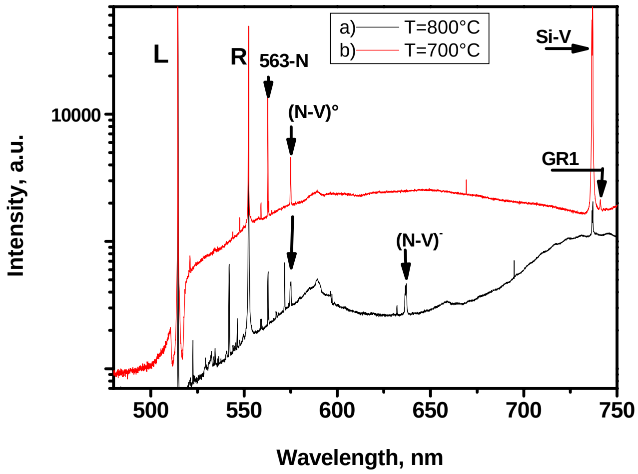

Figure 4.13: *Photoluminescence spectra obtained at liquid nitrogen temperature using a 514 nm green laser for excitation. The corresponding diamond layers were grown at (a) at 800 °C (b) at 700 °C. Both spectra have been normalized to the Raman line.*

The 3H defect. The use of high-energy 488.0 nm laser excitation allows the detection of trace amounts of 3H (503.5 nm) and H3 (503.2 nm) defects. The 3H defect with a zero-phonon line position at 503.5 nm and the defect H3 at 503.2 nm also observed in the freestanding plates. The 3H defect is a typical self-interstitial related centre [Col89], relatively unstable and should be annealed out at typical CVD growth temperatures [Zai01]; nevertheless the 3H defect was detected in all the freestanding films.

4.5. Time-of-flight transport measurements

4.5.1. Introduction

An important characteristic of CVD diamond for electronic applications are the electron and hole drift mobilites. Because the undoped material is highly resistive the Hall measurements cannot be applied to undoped CVD diamond. Therefore the drift mobilities can be measured for example by using a Time-of-Flight (TOF) system, relaying on a generation of carriers by a strong absorption of light and transporting this charge through the sample under an electric field. The TOF system is described below. Early TOF measurements carried out on single crystalline SCCVD diamond samples by using the technique in the space charge limited (SCLC) mode suggested mobilities as high as 3800 and 4500 cm^2/Vs for holes and electrons respectively [Isb02]. However, recent data using particle-induced TOF rather suggested mobilities closer to the value published for IIa diamond, i.e. about 2000 cm^2/Vs [Fin06, Pom05]. To resolve this controversy IIa natural and SCCVD diamond samples were measured in small signal TOF mode and the results were compared with measurements in SCLC mode using laser induced charge generation. Additionally, the influence of defects in the SCCVD diamond films on the charge trapping and charge transport characteristics were studied.

4.5.2. Experimental

Two modes of TOF operation were used. Firstly, the small signal TOF mode, was used if the photo generated charge $Q_{ph} << Q_0$, where $Q_o = CE$ (C is the sample capacity and E the electric field applied). A atypical value of C is ~ 0.5 pF for 2 mm diameter contacts and a thickness of the diamond layer of 500 μm. On the other hand the SCLC mode is obtained when $Q_{ph} >> Q_0$. The RC constant of the detection system must be much lower than the transit time. This is achieved by matching the detection circuit by using 50 Ohm matched high frequency detection electronics, specially designed for TOF experiments. Care was taken to reduce all parasitic inductances in the measurement box. A pulsed (AC) electric field (~ 3 ms) was applied on the sample to assure a homogeneous electric field profile in the time of the charge transit. The laser pulse was delayed with respect to the electric field with typically 50 μs, which is significantly shorter than the dielectric relaxation time (~ ρε where ρ is the specific resistivity and ε the dielectric permittivity of diamond). The signals were recorded with a 2.5 GS/s (500 MHz) digital oscilloscope with 25 shots averaged to improve the S/N ratio.

Samples measured were a (100) oriented natural IIa diamond 90105euos and 60405euos, 60207euos CVD diamonds (see details in Fig.4.14 and Table 4.5). IIa natural diamond sample was used as a comparison measure.

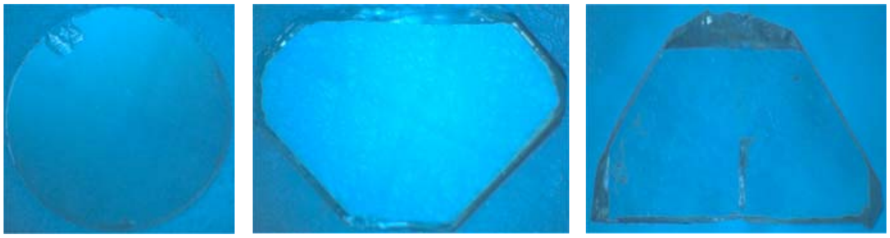

Figure 4.14: *Diamond samples TOF studied: a) natural IIa diamond sample 90105euos; b) SCCVD diamond sample 60405euos; c) SCCVD diamond sample 60207euos.*

Sample	Type	Orientation	Sample size (mm^2)	Contacts	Top/bottom contacts nm/nm (Ømm)
90105euos	IIa	(100)	Ø5×0.5	Al / Al	20/50 (3)
60405euos	SCCVD	(100)	2.3×2.3×0.24	Al / Al	20/50 (2)
60207euos	SCCVD	(100)	3×2.5×0.44	Al / Al	20/50 (2)

Table 4.5: *Diamond samples details.*

The samples are cleaned and their surface oxidized using a solution of H_2SO_4+KNO_3 at 300 °C during 30 minutes and by consequent rinsing with deionised ultra-pure water. The top semitransparent and back non-transparent Al contacts were evaporated from a thermal Al source. The contacts were sufficiently blocking to satisfy the TOF requirements (see Fig. 4.14). The transmittance of the Al semitransparent contact was about 30% at 220 nm and their resistance was < 1 kOhm.

4.5.3. Results and discussion

Fig. 4.15 shows the transit photocurrent decay for electrons and holes for an electrical field of ~0.22 V/µm. After the laser shot, the photo-induced current drops off shortly, independently from the electric field applied due to charge trapping at defects. The main photo induced charge gets trapped after the laser shot and remains trapped and it is not re-emitted into the transport path on the time of the experiment $t \sim 5t_T$, where the t_T is the transit time. However, a small part of the charge manages to transit the sample, leading to a well-defined electrical field dependent transit time. As a part of this charge can be delayed due to the dispersion effects of the drifting charge or by a trapping, a transit time is defined as a change of the slope from pre transit to post transit region which is typically used for transport in a dispersive semiconducting material (see below).

The transit time is related to the drift mobility μ and the electric fields E as follows

$$t_T = d/(\mu \cdot E), \qquad (1)$$

where d is the sample thickness. The transit time t_T, indicated by arrows in Fig. 4.15. As discussed in the literature, several definitions of t_T time can be found, one of them is that t_T is defined as a time during which the photocurrent drops to 50% of its value after the laser shot charge generation [Neb97]. This definition of the transit time t_T is related to a movement of the main weight of the laser generated charge parcel, transported through the sample. However, this definition cannot be used in the case of dispersive transport such as for the CVD sample 60405euos and the IIa diamond sample 90105euos. In this case the majority of the charge is trapped just after the laser pulse. In such a dispersive transport situation the charge arrival to the collection electrode is delayed due to charge reemission from the traps. In this case the change in the slope in the log(I)- log(t) plot indicates the arrival of the fastest carriers to the collecting electrode. The transit time can be defined as a time needed for carriers to traverse the samples from the front to the back electrodes.

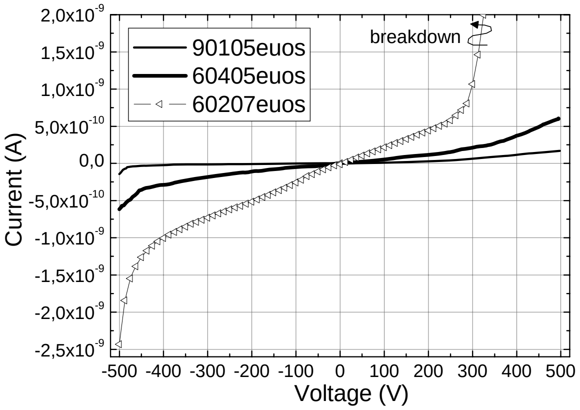

Figure 4.14: *IV-Characteristics of oxidized natural IIa diamond (90105euos) and SCCVD diamond 60405euos, 60207euos) plates with Al contacts, measured at room temperature using a Keithley 6517A electrometer.*

This definition of t_T is used throughout this work. This means that the drift mobility can be slightly overestimated (~ 10 % as determined by the numerical simulation due to the fact that the fastest carriers are taken into account). The drift mobility, determined by equation (1), is calculated for the samples 90105euos and 60405euos in Fig.4.15. Based on the data in Fig. 4.15 the drift mobility for the IIa diamond sample is about ~2150 cm²/Vs for holes and ~2650 cm²/Vs for electrons respectively, for an electric field of about 0.22 V/μm. For the CVD diamond 60405euos the mobility is lower and it is about 650 cm²/Vs for holes and 950cm²/Vs for electrons. The values for IIa diamond agree well with the theoretical data published in the literature, which are governed by the phonon scattering on acoustic phones at room temperature [Nav80]. The lower mobility for sample 60405euos suggests an additional scattering mechanism due to defects, such as ionized impurities or structural defects, i.e. dislocations, an effect that will be further studied. Figure 4.16 shows the mobility recalculated for sample 90105euos and 60405euos and demonstrates the tendency of decreasing carrier mobility for lower electric fields. The initial voltage independent drop of the photocurrent after the photo-excitation for both sample 90105euos and sample 60405euos suggests that the layers contain deep traps in the bulk causing the initial drop of the photocurrent. Such a low TOF signal makes a precise measurement difficult, especially for the IIa natural diamond sample.

Fig. 4.17 shows TOF data for the high purity sample 60207euos as a function of the laser intensity expressed in the power of the IR (1024 μm) YAG beam.

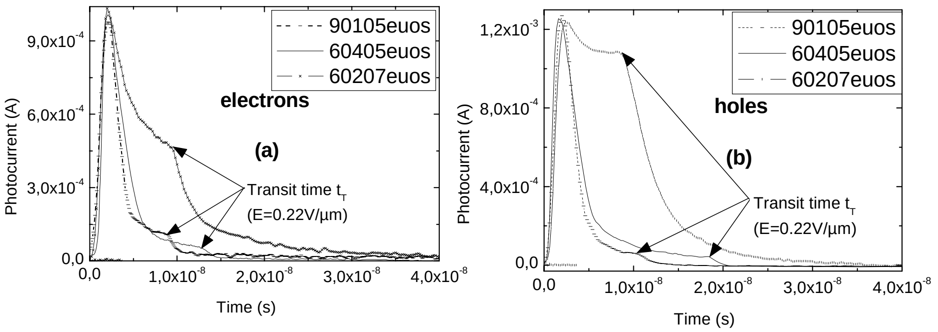

Figure 4.15: *Comparison of the transient photocurrent, induced by a 2.7 ns laser shot at 218 nm for CVD (samples 60405euos, 60207euos) and IIa (sample 90105euos) diamond.*

By increasing the laser intensity the SCLC conditions are reached as indicated by a dotted line in Fig. 4.17. Upon increasing the laser intensity the shape of the transient changes significantly and a “cusp” characteristic for the SCLC mode appears. This feature is related to the so-called extraction time [Piv05, Isb04], which is usually shorter that the transit time by a relation:

$$t_E = \beta \cdot t_T \tag{2}$$

with β coefficient about 0.787 [Isb04]. Using the experimentally measured extraction time t_E yields 0.85 for $\tilde{\beta}$. This suggests that the mechanism of the charge relaxation at the contacts for low electric field deviates slightly from the theory presented in ref. [Isb04]. This is believed to be mainly due to charge trapping at the contacts, which is changing the electric field profile. However, this point needs further investigation.

In order to determine the charge carrier mobility at low fields μ_0 the experimental data are fitted with the formula (2). The parameters μ_0 and saturation velocity (V_S) were adjusted to match the slope.

$$\mu = \frac{\mu_0}{1 + \frac{\mu_0 E}{V_S}}, \tag{3}$$

The mobility determined from the small signal TOF is calculated using a numerical fitting based on Equation (3).

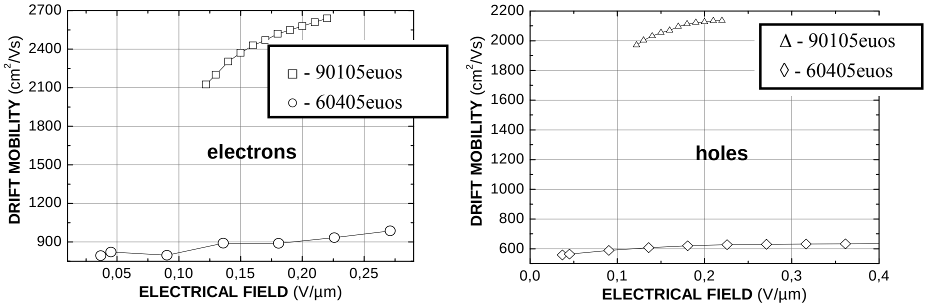

Figure 4.16: *The electron and hole mobilities calculated from the transit time for IIa diamond 90105euos and CVD diamond 60405euos samples and, based on the transient traces shown in Figure 4.15 and fitted by an asymptotic behavior formula for the saturation drift velocity.* V_S *equals* $1.2 \cdot 10^7$ *cm/s for holes and* $1 \cdot 10^7$ *cm/s for electrons.*

This fitting yields a value of 2050 cm^2/Vs for electrons and 2250 cm^2/Vs for holes at room temperature. These values correspond very well to the data obtained for IIa diamond with a difference of ±200 cm²/Vs.

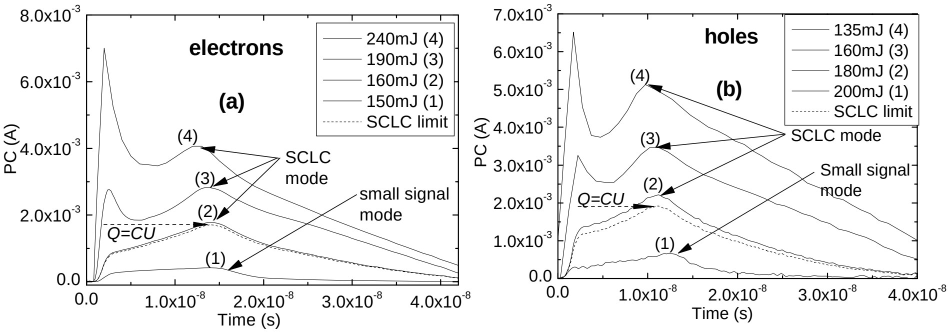

Figure 4.17: *The transient photocurrent for a high quality CVD diamond 60207euos as a function of the laser intensity of the IR YAG pump beam. The transition to the SCLC mode is indicated by a dotted line at* $Q = CE$ *where C is the sample capacity and E the electric field applied. This sample showed a mobility of 2250* cm^2/Vs *for holes and 2050* cm^2/Vs *for electrons calculated from equations (1) and (2).*

A nearly perfect signal with no trapping is visible. It is suggested that the main difference in the data for IIa and CVD diamond samples comes from the precision for the determination of the t_T, which is about 10 - 15 % due to the dispersive character of the transport in IIa diamond. For the sample 60207euos the value for the electron mobility is slightly lower than the hole mobility.

4.6. Conclusions

Chapter 4 was devoted to a detail characterization of structural defects in CVD diamond layers, which understanding is of outmost importance for optical and electrical applications of CVD diamond. The detail spectroscopy characterization tells not only about the presence of the defects, which strongly influence the optical and electrical characteristics of freestanding SCCVD diamond films but additionally it gives important hints about the epitaxial CVD diamond growth and about the detail mechanism of the plasma-chemical interaction at the growing surface leading to the incorporation of impurities and defects. To study these defects in detail Chapter 4 was divided to several sections to allow characterization of defects using gemological, optical, magnetic and transport techniques.

The main results can be summarized as follows:

The gemological characterization used clearly show that the freestanding films are of high gemological quality, matching the quality of IIa natural diamond. Specifically, the color grade was determined with a Gran colorimeter and surface luminescence images of the CVD plates were recorded using the DiamondView^{TM}. These results show that the color of the best crystal is D which means comparable clear IIa crystals. Additionally the DiamondView images show that in optimized films no visible (N-V) or (Si-V) luminescence is present, confirming low incorporation of residual impurities. However, the blue luminescence (band A) was observed, excited by UV sources related to the dislocations. In detail cross-polarized imaging we have seen a typical image of dislocation patterns different to known “tatami” patterns in IIa natural diamond, responsible for the presence of dislocations. As the dislocation originates from substrate, as it has been discussed in Chapter 3 we tried to minimize their presence by a suitable surface treatment discussed also in Chapter 3.

To study the presence of impurities on sub ppm scale, the photocurrent technique in AMFTPS configuration was used. By optimization of this technique in collaboration with the colleagues at the institute of Physics, Czech Academy of Sciences we had succeeded at a very sensitive detection of defects on sub ppm scale. Nevertheless, even in the best films, when measured on this very sensitive level, residua of N in substitutional state (P1 defect) was present, which concentration has been evaluated to be in the range of ppm or lower. Residual N comes into the films from minor leaks in reactors (in our case the leak rate was very low as 1×10^{-8} mbar/sec). This value is higher than that acquired from EPR measurements which should typically be 1 - 2 decade lower P1 (N) defect concentration. We explain this difference of different charge state of N, because only P1 defect (N_S^0) with a free spin is observable in EPR. The best commercial samples studied with low N concentration show also rather high N-response in the PC spectra, similar to the films of this study, confirming that nitrogen concentration is actually higher as measured by EPR. Additionally in some films we could observe B-residua, we consider the B-residua incorporation from the reactor walls and other material present in the reaction vessel.

The EPR measurements confirmed presence of several defects; the most important of this is the P1 defect also seen by AMFTPS and additionally the H1 defect observed clearly even in our homoepitaxial films. We have made a speculation that the low energy tail observed in AMFTPS spectra and called D_x defect is related to this H1 defect (which is a C-dangling coupled bond to H atom in a close proximity). Additionally we could see minor $(N\text{-}V)^-$ presence in our films, but the exact concentration was limited by the resolution of the setup.

The PL and CL study gave us significant information about the range of defects present in our films. From about 300 known defects in IIa and CVD diamond we could see mainly $(N–V)^0$, $(N–V)^-$, centers and minor luminescence from H3 centre (N–V–N). Also we detected a blue “band A” luminescence due to presence of dislocations, GR1 band related to vacancy at 741 nm and accompanied with 737 nm (Si-V) centers originating from the residual Si coming from MW Quartz window. This is surprising as the growth takes place at 700 °C, where vacancies are mobile, however they are observed in the CVD diamond samples. In addition, very weak emissions of at 596nm, 683 nm, and 600 – 610 nm were occasionally observed in the freestanding samples the origin of which is unclear. We could see also other complexes such as 5RL and 2BD and trace amounts of 3H (503.5 nm).

The UV luminescence measurement allowed us to study the quality of the CVD films by observing the exciton recombination. Specifically, the peaks at 235 nm (FE^{TO}), 242 nm (FE^{TO+O}), 233 nm (FE^{TA}), and 238 nm (BE^{TO}) could be measured. Because the bound exciton related to B could be measured in some cases we could estimate the residual B concentration which is in ppb range for some films, by an estimation, based on ration of the BE and the FE. For some films BE was not visible. The CL exciton data thus clearly confirm high crystalline quality of the films. Additionally, it allowed to compare the B-concentrations obtained from FTPS data with the CL data.

Finally in, the last part of Chapter 4 we have discussed the electrical transport properties of CVD diamond films grown. It could be established that for a large number of samples we could see a dispersive transport due to trapping of charge on defects present in CVD diamond films, as studied by spectroscopic methods. For the best quality samples we have obtained good electrical transport properties with high mobilities for electrons and holes. Namely the precise fitting yielded a value of 2050 cm^2/Vs for electrons and 2250 cm^2/Vs for holes at room temperature. These values correspond very well to the data obtained for IIa diamond and nearly prefect signal with no trapping was visible.

4.7. References

[Cla92] C.D. Clark, C.B. Dickerson et al., J. Phys.-Cond. Matter **4** (3) (1992), 869-878.

[Col92] A.T. Collins, Diam. Relat. Mater. **1** (1992), 457.

[Dav97] G. Davies, Chem. Phys. Carbon, **13** (1979), 1.

[Dea64] P.J. Dean, J.C. Male, J. Phys. Chem. Solids **25** (1964), 1369.

[Dea65] P.J. Dean, E.C. Lightowlers, D.R. Wight, Phys. Rev. A **140** (1965), 352.

[How03] D.F. Howarth, J.A. Weil, Z. Zimpel, J. Magn. Res. **161** (2003), 215.

[Hyd90] J.S. Hyde, M. Pasenkiewicz-Gierula, A. Jesmanowicz, W.E. Antholine, Appl. Magn. Reson. **1** (1990), 483.

[Fin06] J. Fink, P. Lodomez, H. Kruger, H. Pernegger, P. Weilhammer, N. Wermes, Nuclear Instruments and Methods in Physics Research A **565** (2006), 227–233.

[Isb02] J. Isberg, J. Hammersberg, E. Johansson, T. Wikstrom, D. J. Twitchen, A. J. Whitehead, S. E. Coe, G. A. Scarsbrook, Science **297**(2002),1670-1672

[Isb04] J. Isberg, J. Hammersberg, D.J. Twitchen, A.J. Whitehead, Diam. Relat. Mater. **13** (2004), 872– 875.

[Isb06] J. Isberg, A. Tajani, D. J. Twitchen, Phys. Rev. B **73** (2006), 245207.

[Kas04] M. Kasu, M. Kubovic, A. Aleksov, N. Teofilov, Y. Taniyasu, R. Sauer, E. Kohn, T. Makimoto, N. Kobayashi, Diam. Relat. Mater. **13** (2004), 226.

[Kan04] H. Kanda, K. Watanabe, Diam. Relat. Mater. **13** (2004), 904.

[Kaw93] H. Kawarada, A. Yamaguchi, Diam. Relat. Mater. **2** (1993), 100.

[Kaw93b] H. Kawarada, H. Matsuyama, Y. Yokota, T. Sogi, H. Hirayama, A.Yamaguchi, A. Hiraki, Phys. Rev., B **47** (1993), 3633.

[Kin98] J.M. King, T.M. Moses, J.E. Shigley, C.M. Welbourn, S.C. Lawson, M. Cooper, Gems & Gemology **34**(4) (1998), 246-268.

[Law95] S.C. Lawson, H. Kanda, H. Kiyota, T. Tsutsumi, H. Kawarada, J. Appl. Phys. **77** (1995), 1729.

[Lee89] S.Lee, S. Kumar, C.R.Wronski, N. Maley, J. Non-Crystalline Sol. **114** (1989), 316

[Mar04] P. M. Martineau, S. C. Lawson, A. J. Taylor, S. J. Quinn, D. J. F. Evans, M. J. Crowder, Gems & Gemology **40**(1) (2004), 2–25.

[Nav80] F. Nava, C. Canali, C. Jacoboni, L. Reggiani, S. F. Kozlov, Solid State Commun. 33, 475 (1980).

[Neb97] C. E. Nebel, J. Munz, M. Stutzmann, R. Zachai, H. Guttler, Phys. Rev. B 55, 9786 (1997).

[Oku01] H. Okushi, Diam. Relat. Mater. **10** (2001), 281.

[Piv05] A. Pivaskas, R. Osterbaka, G. Juska, K. Arlauskas, H. Stubb, Sinthetic Metals. **155** (2005), 242- 245.

[Pom05] M. Pomorski, E. Berdermann, M. Ciobanu, A. Martemyianov, P. Moritz, M. Rebisz, B. Marczewska, Phys. stat. sol. (a) **202**(11) 11 (2005), 2199–2205.

[Ros99] J. Rosa, M. Vanecek, M. Nesladek, L.M. Stals, Diam. Relat. Mater. **8** (1999), 721.

[Rem05] Z. Remes, R. Petersen, K. Haenen, M. Nesladek, and M. D'Olieslaeger, Diam. Relat. Mater. **14** (2005), 556.

[Rem07] Z. Remes , M. Nesladek , P. Bergonzo, J. Barjon, F. Jomard, Phys. Stat. Sol. (a) **204** (9) (2007), 2950-2956.

[Roh96] E. Rohrer, C. F. O. Graeff, R. Janssen, C. E. Nebel, M. Stutzmann, H. Güttler, R. Zachai, Phys. Rev. B **54** (1996), 7874.

[Rua92] J. Ruan, K. Kobashi, W.J. Choyke, Appl. Phys. Lett. **60** (1992), 1884.

[Sau04] R. Sauer, Thin-film diamond I, in: C.E. Nebel, J. Ristein (Eds.),Semiconductors and Semimetals **76** (2004), 379.

[Shi97] J.E. Shigley, T. Moses, I. Reinitz, S. Elen, S.F. McClure, E. Fritsch, Gems & Gemology **33**(1) (1997), 42-53.

[Van02] M. Vanecek, A. Poruba, Appl. Phys. Lett. **80** (2002), 719.

[Van03] M.Vanecek, R.Kravets, A.Poruba, J.Rosa, M.Nesladek, S.Koizumi, Diam. Relat. Mater. **12** (2003), 521.

[Wad04] M. Wade, M. Kadri, E. Bustarret, A. Deneuville, P. Muret, D. Araujo, Phys. Status Solidi, A Appl. Res. **201** (2004), 2457.

[Wan03] W. Wang, T. Moses, R. Linares, J.E. Shigley, M. Hall, J.E. Butler, Gems & Gemology **39**(4) (2003), 268-283.

[Wan05] W. Y. Wang, A. Tallaire, M. Hall, T. M. Moses, J. Achard, R. S. Sussmann, A. Gicquel, Gems & Gemology **41**(3) (2005), 234–244.

[Wel96] C.M. Welbourn, M. Cooper, P.M. Spear, Gems & Gemology **32**(3) (1996), 156–169.

[Wyk97] J.A. van Wyk, E.C. Reynhardt, G.L. High, I. Kiflawi, J. Phys:D Appl. Phys. **30** (1997) 1790-1793.

[Zai01] A.M. Zaitsev, Optical properties of diamond, A Data Handbook, Springer-Verlag Berlin, Heidelberg, 200.

Chapter 5 Concluding remarks and further perspectives

The aim of the concluding remarks is to supplement information concerning main results obtained in this work and given in detail in Chapter 3, Chapter 4 and summarized in Chapter 3 and Chapter 4 Conclusions. When this thesis has been started in January 2004, the single crystal diamond technology appeared suddenly as a significant novelty aiming at future electronics applications of CVD diamond. This was the important scientific motivation with which the thesis work has been initiated, to develop growth techniques which could lead to the preparation of high quality single crystal free standing diamond. Based on the experience of the group at IMO, University of Hasselt, lead that time by Prof. M. Nesládek the developments based on using plasmas of high densities and working at relatively high gas pressures have been adopted which seemed to be promising for the preparation of high quality epitaxial diamond. As an important breakthrough, a few month before the work was started, an article of Isberg *et al.* [Isb01] had appeared in the scientific literature that based on a material developed by the Element Six Ltd company, it had shown measurements of extremely high charge carrier mobilities for electrons and holes, measured on SCCVD diamond, better factor 2 than of natural IIa diamond. The preparation of this material was a subject of unpublished research works of the Element Six Ltd Company that came as a big surprise to the scientific community and has raised motivation of many groups to develop such high quality material.

In the original approach planned at the beginning of the thesis in 2004, the high plasma densities were obtained by confining the plasmas to a small volume typically 1 cm^3 with power of typically 1000 W by a specially designed plasma configuration including the substrate holder, which allowed operating such high plasma densities at relatively high gas pressure. This was the starting idea of the thesis which has been further developed. At the initial stage of the thesis the plasma configurations optimization, design of different types of substrate holders have been undertaken. The substrate configurations significantly influenced the plasma sheet and the plasma-chemical interaction in the close vicinity of the substrate surface. Based on the literature study an original solution for the problem of high quality CVD diamond epitaxial growth came up. After first sets of designs and draft process window parameter mapping it has been soon realized that the samples prepared at novel conditions have rather specific surface structural properties. In the trend observed, even after prolonged CVD diamond growth, nearly atomically flat substrate surfaces could be prepared, which finding has been published in several scientific journals. This was an excellent starting point of the further work, when the search for the mechanism of the growth and improvements has led to the growth of nearly perfect crystals. To find such improvements one had to base the optimization on detail understanding of the diamond crystallography, structure of diamond, its surface, crystallographic defects and role of defects in the crystal growth.

To cope with this challenge collaboration established within a Belgian and EU-based project has been resorted. The work then proceeded in close collaboration with many European scientists on the characterization of the diamond films, including structural, defects spectroscopy and electric transport measurement methods. The task to learn about the physics of defects in CVD diamond was challenging but also exciting for the author, and at the same time very beneficial for understanding of the CVD diamond growth mechanism and led to further optimization of the growth conditions, clearly reflected in changes of physical properties of CVD diamond studied. In the meantime many physical techniques described in Chapter 2 such as optical techniques, Raman spectroscopy, PL/CL luminescence, EPR, Photocurrent, Scanning Electron microscopy, Time-of-flight measurements, gemological methods, AFM, STM, SEM and other methods have been studied in order to get insight into the films properties. Collaboration with scientists specialized in the field and joint published works have been carried out.. Based on the results obtained the main defect structures could be traced up in the films grown. Many of them were related to the impurities such as nitrogen, boron, silicon, hydrogen and other elements which incorporation could be altered by the plasma conditions, which was one of the important tasks of this work.

At the same time the physics of diamond surfaces has been intensively studied in detail and quite soon after the beginning of the thesis it was found that the surface, although atomically flat, is composed of small nano-clusters, which origin has been investigated in details at IMO and in collaboration with KU Leuven using the surface techniques with atomic resolution (AFM, STM). It was surprising that these structures were present onto the surface almost independently of the growth time and were related to the specific growth mode at high CH_4 concentrations which was used in the course of this work. These surface diamond nano-clusters were not similar to the classical growth modes such as Volmer –Weber or Stranski-Kastranov, as the interface volume remained constant during the films growth; on the other hand it was not clearly layer by layer grown as expected of such kind of interface development. Further progress has been made when the surface layer has been etched away by atomic hydrogen plasma. The result after the etching clearly showed, that the subsurface of the diamond film and the bulk of crystal is high quality monocrystalline diamond, as confirmed by the Raman spectroscopy leading to a first Raman line at 1332 cm^{-1} with FWHM of ~1.6 cm^{-1}, i.e. better than IIa diamond, and the observable 2nd order Raman peak, i.e. comparable to the best results in the literature. Based on these results we have concluded that the growth mechanism, different from the published step flow growth mechanism is leading to barely perfect crystal growth.

We have studied additionally the influence of the surface and substrate quality on the crystal growth and developed specific surface O_2/H_2 plasma treatments allowing reduction of crystallographic defects incorporated in the films and originating from the substrate. Using the optimized conditions we have studied reproducibility of preparation of the diamond films grown over prolonged time period of several hundreds hours, and studied in detail the growth mechanism, defect incorporation and propagation in the crystal during the crystal growth. Finally, after optimizing this step the best layers have been subjected to the transport measurements using the Time-of-flight setup, allowing to measure the electrical and hole mobilities and compared the data with the published data of the group of Isberg which, at the same time with the results of this thesis were evolving in the due course. Based on this work results it could be confirmed that the material produced is of excellent quality with theoretical mobilities for diamond with no observable charge trapping and it can be used for several applications in electronics such as for detectors, ranging from UV to particle detectors. The electronic properties of the material produced in this study thus arrived to the expectations raised on the beginning of the thesis, allowing preparing high quality crystals with optimized defect density, controlled growth mechanism and transport properties.

To finish I would like to recall the Greek word used in the introduction of the thesis i.e. *adamao*, meant 'I tame' or 'I subdue' as I was deeply involved and served the “physics of diamond” and in the topic which brought to me exciting physics of the plasma CVD growth and which let my personal satisfaction. Also I would like to recall the related word *adamas*, which means 'hardest steel' or 'hardest substance' which after the completion of my work can confirm it in the research not related to diamond only